Vesicle Adhesion, Fusion, and Neurotransmitter Uptake Studied by Small-Angle X-ray Scattering

Dissertation
for the award of the degree
"Doctor rerum naturalium"
of the Georg-August-Universität Göttingen

within the doctoral program
Göttingen Graduate Center for Neurosciences,
Biophysics, and Molecular Biosciences (GGNB)
of the Georg-August University School of Science (GAUSS)

submitted by
Karlo Komorowski
from Mölln

Göttingen, 2020

Thesis Committee

Prof. Dr. Tim Salditt, Institut für Röntgenphysik, Georg-August Universität Göttingen

Prof. Dr. Claudia Steinem, Institut für Organische und Biomolekulare Chemie, Georg-August-Universität Göttingen

Prof. Dr. Silvio Rizzoli, Institut für Neuro- und Sinnesphysiologie, Universitätsmedizin Göttingen

Members of the Examination Board

First Reviewer: **Prof. Dr. Tim Salditt**, Institut für Röntgenphysik, Georg-August Universität Göttingen

Second Reviewer: **Prof. Dr. Claudia Steinem**, Institut für Organische und Biomolekulare Chemie, Georg-August-Universität Göttingen

Further members of the Examination Board

Prof. Dr. Silvio Rizzoli, Institut für Neuro- und Sinnesphysiologie, Universitätsmedizin Göttingen

Prof. Dr. Sarah Köster, Institut für Röntgenphysik, Georg-August Universität Göttingen

Prof. Dr. Marcus Müller, Institut für Theoretische Physik, Georg-August Universität Göttingen

Prof. Dr. Stefan Klumpp, Institut für Dynamik komplexer Systeme, Georg-August Universität Göttingen

Date of the oral examination: 15.02.2021

Contents

Abstract **1**

1 Introduction **3**
1.1 Synaptic Neurotransmission . . . 3
1.2 Adhesion and fusion of vesicles . . . 7
1.3 X-ray structure analysis of vesicles . . . 19

2 Vesicle adhesion and fusion studied by small-angle X-ray scattering **25**
2.1 Introduction . . . 25
2.2 Materials and Methods . . . 28
2.2.1 Preparation of vesicles . . . 28
2.2.2 Protein expression and purification . . . 29
2.2.3 Preparation of SNARE-liposomes . . . 29
2.2.4 Small-angle X-ray scattering . . . 30
2.2.5 Form and structure factor models . . . 31
2.3 Results and Discussion . . . 36
2.3.1 SAXS characterisation of unilamellar vesicles . . . 36
2.3.2 Adhesion of lipid vesicles . . . 38
2.3.3 Interaction potentials . . . 42
2.3.4 Outlook: SNARE-liposomes . . . 46
2.4 Summary and Conclusions . . . 48

3 Vesicle adhesion in the electrostatic strong-coupling regime studied by time-resolved small-angle X-ray scattering **53**
3.1 Introduction . . . 53
3.2 Interaction potentials and strong coupling regime . . . 56
3.3 Materials and Methods . . . 59
3.3.1 Microfluidics devices . . . 59
3.3.2 Simulation of the microfluidic flow . . . 60
3.3.3 Sample preparation . . . 60

3.3.4 Small-angle X-ray scattering 60
3.3.4.1 Microfluidic SAXS 61
3.3.4.2 Flow-through and stopped-flow SAXS 61
3.3.4.3 SAXS analysis 61
3.4 Results and Discussion 64
3.4.1 Vesicle adhesion in the strong coupling regime 64
3.4.2 SAXS combined with the stopped-flow rapid mixing device . . 67
3.4.3 SAXS combined with microfluidics 71
3.5 Conclusions 77

4 Neurotransmitter uptake and fusion of synaptic vesicles studied by X-ray diffraction 81
4.1 Introduction 81
4.2 Materials and Methods 86
4.2.1 Preparation of the uptake experiment 86
4.2.2 Preperation of proteoliposomes 86
4.2.3 Small-angle X-ray scattering 87
4.2.3.1 SAXS measurements 87
4.2.3.2 SAXS analysis 87
4.3 Results and Discussion 91
4.3.1 Polydispersity und Purity 91
4.3.2 Structure of SVs upon glutamate uptake 95
4.3.3 Fusion of SVs with proteoliposomes 99
4.4 Conclusion and Outlook 101

5 Summary and Outlook 107

Appendix 111
A.1 Supporting Material: Vesicle adhesion and fusion studied by small-angle X-ray scattering 111
A.1.1 Dynamic Light Scattering 111
A.1.2 Non-interacting vesicles: additional figures and tables 113
A.1.3 Adhesion of vesicles: additional figures and tables 122
A.1.4 SNARE-mediated liposome fusion and docking experiments . 126
A.2 Supplementary information: Vesicle adhesion in the strong coupling regime studied by time-resolved small-angle X-ray scattering 128

A.3 Neurotransmitter uptake and fusion of synaptic vesicles studied by X-ray diffraction: Supplemental Material 132
A.3.1 Supplementary data: dynamic light scattering (DLS) 132
A.3.2 Supplementary SAXS data analysis: alternative fitting strategy 135
A.3.3 Supplementary SAXS data analysis: isotropic model composed of spherical shells 141
A.3.4 Supplementary data: SVs in different buffer 144

Bibliography **145**

Authors Contribution **161**

Publications **163**

Acknowledgements **165**

Abstract

Synaptic neurotransmission is a highly complex and crucial process in the communication between neuronal cells, and is thus directly related to the complex functions of the neural system, including information processing in the brain, sensory reactions, and learning. The last decades have considerably shaped our current understanding of the underlying processes in synaptic neurotransmission on the molecular level, and up to the level of the entire synapse. X-ray crystallography and more recently also cryo-electron microscopy have provided the structural basis to elucidate the function of many synaptic proteins. At the same time, synaptic neurotransmission also relies crucially on processes governed by biological membranes. Synaptic vesicles as small membranous organelles store neurotransmitters in the cytoplasm of the synapse and release them into the synaptic cleft in a highly controlled manner. While synaptic vesicles can be described in a very detailed picture in terms of their molecular composition, less is known about structural rearrangements involved in the dynamic processes of neurotransmitter uptake and fusion with the presynaptic plasma membrane.

This work employs X-ray diffraction, in particular small-angle X-ray scattering (SAXS), for structural investigations of vesicles in view of adhesion, fusion and neurotransmitter uptake. To this end, we study model lipid vesicles, as well as vesicles with reconstituted proteins and synaptic vesicles. SAXS is a powerful non-invasive technique which enables to probe the structure of the membrane as well as vesicle size and size distribution (polydispersity) under quasi-physiological conditions in solution.

Membrane adhesion and fusion in the physiological system are the result of a complex interplay between lipids, fusiogenic proteins, ions and water molecules. From a physical point of view, attractive and repulsive forces are balanced in membrane adhesion, and repulsion has to be overcome to enable fusion. Experimentally, we show that adhesion of lipid vesicles induced by divalent salts can be clearly identified by SAXS. The deduced structural parameters, most importantly the interbilayer spacing, can be modeled based on theoretical inter-membrane interaction potentials. For moderately and highly charged systems the experimental results are well in line with the predicted strong-coupling attraction, which is associated with correlated counterions confined

between two bilayers in close proximity.

With the availability of highly brilliant synchrotron radiation, structural dynamics, reaction kinetics, and morphological transitions can be monitored by SAXS with millisecond time-resolution. This work employs rapid turbulent mixing in a stopped-flow device coupled to SAXS to study the structural dynamics of vesicle adhesion and fusion. This allows us to observe intermediate and transient adhesion states in charged vesicles. As a complementary technique to stopped-flow, we also evaluate continuous flow mixing in microfluidics devices for vesicle SAXS.

Finally, we use SAXS to study the structural changes of synaptic vesicles after neurotransmitter (glutamate) uptake, and present first results on fusion of synaptic vesicles with vesicles with reconstituted fusiogenic proteins.

Chapter 1 describes the biological framework, the physics of vesicle adhesion and the corresponding interfacial interaction potentials, and gives a brief summary of X-ray structure analysis of lipid vesicles.

In Chapter 2, SAXS is used to study vesicle adhesion and fusion. SAXS models are discussed in view of potentially discriminating intermediate steps in the vesicle fusion pathway, with a particular focus on vesicle adhesion (docking). We introduce the docking model, which enables the quantitative analysis of SAXS data obtained from adhering vesicles. We show, that the interbilayer spacing in the calcium-induced adhesion of charged unilamellar vesicles is well explained by the electrostatic strong-coupling theory. Further, we study the fusion of vesicles with reconstituted SNARE proteins.

In Chapter 3, time-resolved SAXS is used to investigate the structural dynamics of vesicle adhesion in real time. Intermediate states are observed by using a stopped-flow rapid-mixing device coupled to SAXS. Further, microfluidics SAXS is used in two different beam configurations and the microfluidic flow is studied by scanning-SAXS, i.e. by scanning the microfluidics device by a focused X-ray beam. The main emphasis in this chapter is on strong-coupling.

In Chapter 4, X-ray diffraction is used to study glutamate uptake and fusion of synaptic vesicles. We show, that upon glutamate uptake, structural rearrangements both on the length scale of the membrane and of the entire vesicle can be quantified by SAXS analysis. At the same time, a discussion is provided regarding the limitation of SAXS analysis with respect to polydisperse ensembles and how these limitations could be overcome by single-particle coherent diffraction with X-ray free electron laser pulses.

Chapter 5 provides a brief summary of this thesis and ideas for future directions.

Introduction 1

1.1 Synaptic Neurotransmission

Synaptic neurotransmission is a highly complex process on the sub-cellular and molecular level that constitutes the underlying mechanism in the communication between neuronal cells [1, 2, 3], illustrated in Fig. 1.1. This process takes place in the nerve terminals, so called synapses, which are the connections between neurons. Synaptic Vesicles (SVs) are the key organelles in neurotransmission that store neurotransmitters in the cytoplasm of the synapses under resting conditions [4]. An electrical stimulus, i.e. an incoming action potential in the nerve terminal, leads to the opening of voltage-gated calcium channels. The resulting calcium influx stimulates fusion of neurotransmitter-filled SVs with the synaptic plasma membrane, followed by the release of neurotransmitters into the synaptic cleft (exocytosis). The neurotransmitters, in turn, bind to receptor molecules of the post-synaptic membrane. In this way, the

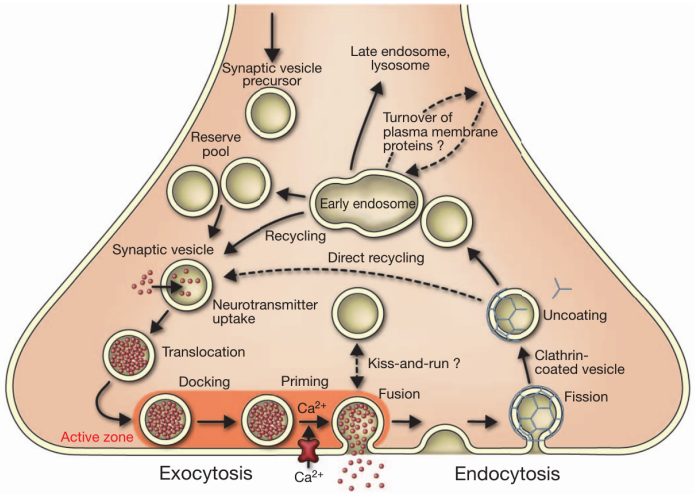

Fig. 1.1: Illustration of the exo- and endocytotic cycle of synaptic vesicles. Figure taken from JAHN *et al.* [3] and used with kind permission from Nature.

signal is transferred from one neuron to another. After exocytosis, SVs are regenerated within the synapse by clathrin-mediated endocytosis, where the SV proteins are retrieved. The rebuilding of SVs takes place either directly or through an endosomal intermediate after the uncoating of clathrin. In a next step, SVs are refilled with neurotransmitters and are then ready for the next round of exocytosis.

Glutamate uptake

The uptake of neurotransmitters is driven by the energy provided by an electrochemical gradient which is established by a vacuolar-type ATPase (V-ATPase) [5, 6, 7]. For this purpose, the V-ATPase translocates protons into the cytosol of the SVs using the energy derived from ATP hydrolysis. With $\sim$ 800 kDa the V-ATPase is the largest protein on the SV, facing towards the cytoplasm of the synapse, with copynumbers of 1 - 2 per vesicle [4]. It is considered that the proton electrochemical gradient is regulated by cytoplasmic ATP concentration [8]. Glutamate uptake reaches a plateau at 2 mM ATP for isolated SVs, which lies well within the physiological range of ATP concentration. Under resting conditions, the cytosolic ATP concentration is approximately 2 mM, and is reduced to 1 mM after endocytosis.

The uptake of neurotransmitters is eventually mediated by vesicular neurotransmitter transporters. The vesicular transporters are defining the neurotransmitter phenotype of a SV, and neurons are traditionally classified accordingly. For glutamate, three different vesicular glutamate transporters (VGLUTs) have been identified, VGLUT1, VGLUT2, and VGLUT3 [9, 5, 10, 11]. Synapses which express VGLUT1 and VGLUT2 are defining the glutamatergic phenotype of neurons (VGLUT3 surprisingly not), and are mainly found in the cerebral cortex and hippocampus or in the thalamus and brain stem, respectively. Glutamate uptake established by an electrochemical gradient further depends on chloride ions and competes with glutamate at high concentrations [12]. It was found, that glutamate transporters possibly also act as proton antiports or as K^+/H^+ exchanger, allowing to adjust to different ionic conditions [12]. Recently it was reported, that a single SV is filled with approximately 8000 glutamate molecules [13].

Great effort has been made to investigate the process of neurotransmitter uptake on the molecular level. Contrarily, the understanding of structural changes on the organelle level and how they relate to physiological function is yet at the beginning. Large structural changes upon glutamate uptake were observed in isolated SVs, with an $\sim$25 % increase in diameter [14]. The lipid bilayer alone can not account for the

corresponding surface area expansion with an increase of $\sim$ 50 %, supporting the idea, that other molecules act as a flexible network within the SV membrane. It was shown, that SVs lacking SV protein 2A (SV2A) did not undergo structural changes upon glutamate uptake, however, the detailed mechanism remain unclear [14]. At this point, one can only speculate about possible implications of the large size increase to physiologically relevant processes. In model membrane systems equipped with the minimal fusion machinery the fusion efficiency was found to be considerably increased with increasing lateral tension [15], which supports the idea, that the large size increase of SVs might play an important role in the efficiency of neurotransmitter release. In fact, there is still a large gap in time scales between fusion taking place during exocytosis in the biological system and fusion between membrane/vesicle model systems, as the observed fusion rates are much higher in the synapse [15].

Fusion of SVs with the presynaptic plasma membrane

Exocytosis of SVs takes place at specific compartments of the presynaptic plasma membrane referred to as active zones. Three temporally and spatially distinct steps can be distinguished such as docking, priming and fusion. Docking and priming means recruiting SVs into the active zone in close proximity to the plasma membrane and activating the release apparatus, respectively. Docked and primed SVs define the ready releasable pool [16], and fuse with the plasma membrane upon calcium influx in a highly cooperative manner.

Fusion of SVs with the presynaptic plasma membrane is crucially mediated by the SNAREs (soluble N-ethylmaleimide-sensitive-factor attachment receptors) synaptobrevin 2, syntaxin 1a and SNAP-25B [17]. Synaptobrevin 2 is situated in the SV membrane, and is the most abundant protein on the SV with a copynumber of approximately 70 per vesicle [4]. Syntaxin 1a and SNAP-25B are associated to the synaptic plasma membrane. The assembly of the SNAREs is considered to be the driving force for fusion of SVs with the synaptic plasma membrane. To this end, they contain characteristic and evolutionary conserved domains of 60 to 70 amino acids, referred to as SNARE motifs, which mediate complex formation of cognate SNARE monomers [18]. While the SNARE motifs of monomeric SNAREs are flexible and rather unstructured in the isolated state, they become helical after assembly to a core complex. Both synaptobrevin 2 and syntaxin 1a contain a transmembrane domain, while it lacks for SNAP-25. However, SNAP-25 is also associated to the synaptic plasma membrane by a hydrophobic post-translational modification that functions as a membrane anchor.

SNAREs were first characterized in the late 1980ies [19, 20], and the first crystal structure of a SNARE complex was published by R. B. SUTTON *et al.* a decade later in 1998 using neuronal SNAREs involved in synaptic exocytosis [21]. The core complex represents a parallel four-helix bundle provided by the SNAREs synaptobrevin 2, syntaxin 1a and SNAP-25B in a 1:1:1 stoichometry. To this complex, SNAP-25 contributes with two α-helices, synaptobrevin 2 and syntaxin 1a contribute each with one α-helix. The

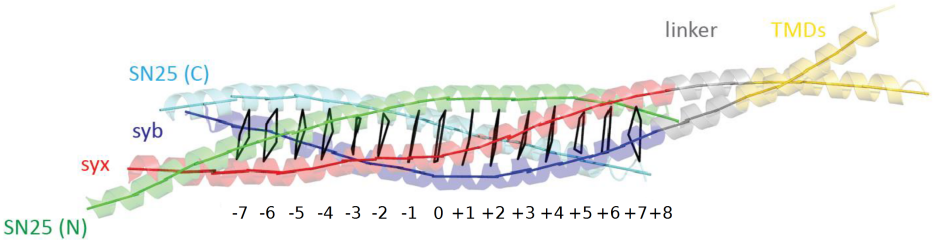

Fig. 1.2: Ribbon structure of the SNARE complex [22], adapted from [23]. The interacting layers (from -7 to $+8$) are indicated. The $+8^{\text{th}}$ layer is not resolved since the electron density of SNAP-25 is lacking at this position.

SNARE complex contains 16 stacked layers in the inner core which are stabilized by mostly hydrophobic side chains interactions with the exception of the '0' layer. The latter is composed of one negatively charged arginine (Arg, R) side chain and three highly polar glutamine (Gln, Q) side chains. SNAREs are classified accordingly into Q- and R-SNAREs with respect to the '0' layer [18]. A functional relevant complex formation for driving membrane fusion has the composition QabcR such as in the case of the neuronal SNARE complex. In this scenario, synaptobrevin 2 represents the R-SNARE, while syntaxin 1a and both the N-terminal and C-terminal helices of SNAP-25 are termed as Qa-, Qb- and Qc-SNAREs, respectively. The amphiphilic character of the SNARE motif also enables other configurations. For example, a Qaabc complex composed of two syntaxin 1a and one SNAP-25 is able to form but provides less energy [24], and therefore it is unable to drive membrane fusion [17]. Further information on the fully assembled SNARE complex including the linker and the transmembrane region was provided later by another X-ray crystallographic study [22], as illustrated in Fig. 1.2. It was found that assembly of synaptobrevin 2 and syntaxin 1a proceeds beyond the SNARE motifs, forming continuous helices along the linker and transmembrane regions. Together with a subsequent study in [23], where fusion of membranes was prevented by using a mutant of synaptobrevin 2 lacking the residue corresponding to the $+8^{\text{th}}$ layer in the SNARE complex, it is suggested that the helical

extension plays a crucial role in the membrane merger.

In vitro, the assembly to a SNARE complex as a minimal fusion machinery is sufficient to drive membrane fusion using artificial membrane systems [25]. However, such a minimal machinery for membrane fusion on its own does not explain physiological observations as for example the fusion efficiency in terms of the reaction rates [26, 17]. Toward the complete picture, it is proposed that the fusion machinery is composed of a set of molecular components, which regulates the assembly and disassembly cycle of SNARE complexes to achieve such a controlled and fast exocytosis. The detailed mechanisms and pathways are reviewed in [3].

1.2 Adhesion and fusion of vesicles

Thus far, we have briefly described the biological framework relevant for this thesis. We can easily see that biological membranes as highly complex interfaces play an important role in synaptic neurotransmission. Both compartmentalization and the ability of membrane fusion are important properties. Compartmentalization enables the parallelization of spatially limited reactions such as the uptake of neurotransmitter, while membrane fusion makes the exchange of substances possible.

The lipid bilayer is often described as the structural matrix of a biological membrane. At the same time, lipids are not only "structural molecules", but they are also directly performing important cellular functions including signaling [27, 28]. The diversity of lipids contributes to the complexity of a biological membrane as to its functions and structural organization [29]. To this end, the lipid composition varies for different cells or organelles as they fulfill different tasks. For example, differences in lipid composition of SVs and the synaptosome were reported recently, where isolated SVs showed a higher fraction of triacyl glycerols and sphingomyelins as opposed to the synaptosome membrane fraction [30].

Along with sterol lipids and sphingolipids, glycerophospholipids are one of the three major groups representing the most abundant group of membrane lipids that are found in eukaryotic membranes [27]. The amphiphilic nature of lipids enables the spontaneous self-assembly of most membrane lipids to higher-level structures in aqueous solutions due to the hydrophobic effect once a critical concentration is reached, referred to as critical micelle concentration (CMC) [31, 32].

Lipids can be generally characterized by their net charge and their effective molecular shape, where both attributes have impact on the type of the formed aggregate. The

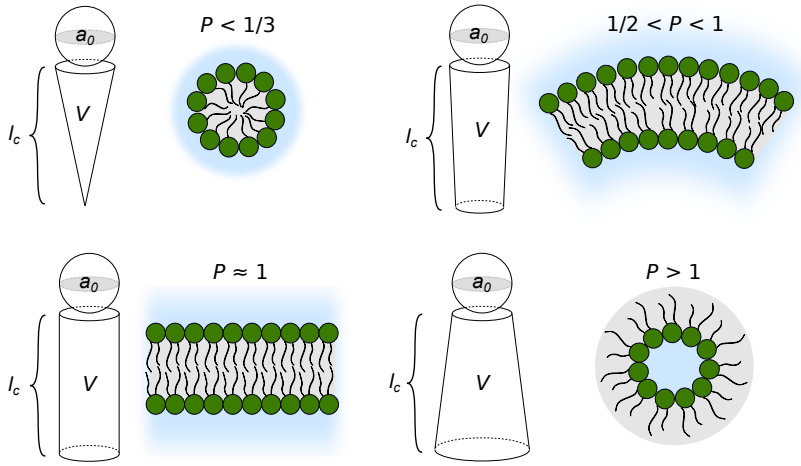

Fig. 1.3: Geometries of mean molecular shapes of different types of lipids and the corresponding lipid aggregates, which depend on the critical packing parameter P, based on [31]. Small values for the packing parameter, $P < 1/3$, as in the case of single-chained lipids (surfactants) result in spherical micelles. In the opposite case, lipids with $P > 1$ corresponding to an inverted truncated cone (e.g. DOPE) have the propensity to form inverted micelles. Lipids with cylindrical shapes ($P \approx 1$) as DOPC have the propensity to form planar bilayers. Unilamellar vesicles are formed by lipids with a truncated cone ($1/2 < P < 1$), where the bilayer shows a spontaneous curvature.

propensity of individual lipids to form a certain aggregate is determined by the packing parameter $P = V/(a_0 l_c)$ with the volume V occupied by the acyl chains, the mean cross-sectional area a_0 of the headgroup in the interfacial region and the length l_c of the chains [31]. Fig. 1.3 shows several geometrical shapes of different lipid species and the corresponding aggregate. However, this rather simplistic picture is in general limited to single-component aggregates, while lipids indeed can form a variety of different aggregates further dependent on, for example, lipid composition, concentration, temperature, and ions. At the same time, the geometrical shape of individual lipid species plays an important role in membrane fusion intermediates. For example, adding DOPE to DOPC can significantly lower the energy for stalk formation due to a reduction of the spontaneous curvature [33, 34].

Once two lipid bilayers are in close proximity, fusion takes place either spontaneously or in a controlled manner for example triggered by fusiogenic proteins or by other external parameters such as the addition of divalent salts or osmotic pressure. Fusion of lipid bilayers proceeds through the formation of non-bilayer intermediates at the contact site [35, 36]. Figure 1.4 illustrates membrane fusion intermediates in the classical fusion-through-hemifusion pathway. In the first step an 'hourglass'-shaped

stalk intermediate is formed, followed by a radial expansion of the stalk to a hemifusion diaphragm. The latter is formed by a lipid bilayer composed of the two distal leaflets, while the proximal leaflets are fused. Subsequently, rupture of this bilayer results in the formation of a fusion pore and eventually in complete fusion.

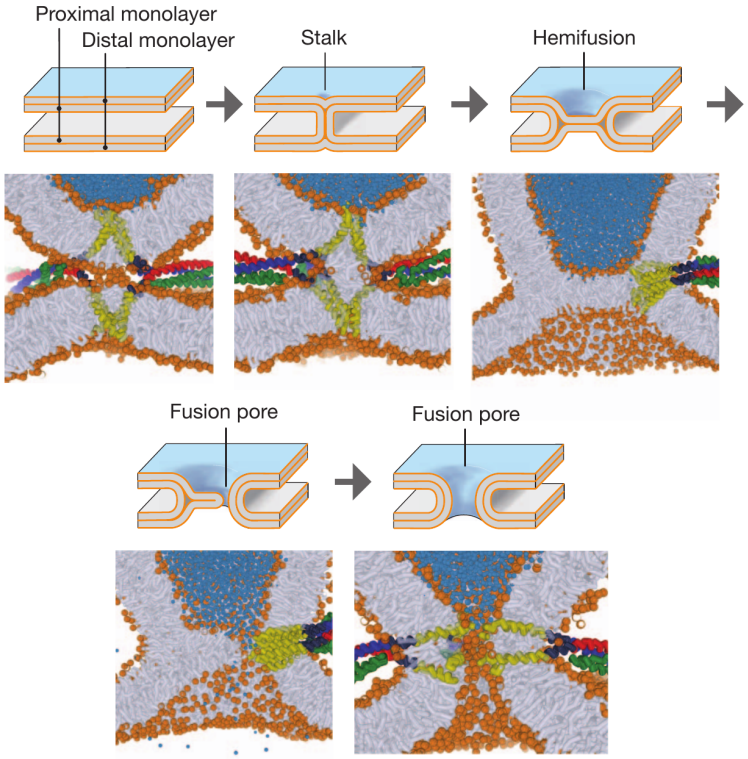

Fig. 1.4: *Top illustrations:* Lipid bilayer fusion intermediates in the classical fusion-through-hemifusion pathway. *Bottom illustrations:* Snapshots of a simulated SNARE-mediate membrane fusion pathway corresponding roughly to the fusion-through-hemifusion pathway. Figure taken from JAHN *et al.* [3] and used with kind permission from Nature.

The interplay between lipids and proteins is indicated in Fig. 1.4 (bottom illustrations) for the case of SNARE-mediated membrane fusion. The intermediate states are represented by snapshots of molecular dynamics simulations [37], which roughly correspond to those of the pure lipid bilayer fusion-through-hemifusion pathway. Zippering of SNAREs brings two bilayers into close proximity. Importantly, subsequent lipidic intermediate states are also facilitated by the SNAREs [37]. Beyond the predicted classical model other pathways have been reported in the framework of the stalk hypothesis [38, 36, 39]. In general, the detailed mechanisms with respect to intermediate

molecular structures as well as the energy landscapes of membrane fusion pathways are still not fully understood. Structural rearrangements take place at short time and small length scales, and are therefore experimentally difficult to access. In this regard, great progress has been achieved experimentally and based on simulations over the last decade, for example in [34, 40, 41, 42, 43, 44, 45, 46, 47].

Adhesion interaction energy between a pair of vesicles

For vesicle adhesion, the interaction energy forces the opposing vesicles to flatten at the contact site and to form an extended interface between the membranes in close proximity [48, 49, 50, 51]. For simplicity, equally sized vesicles are assumed as illustrated in Fig. 1.5(a). It is further assumed, that the adhering vesicles conserve their volumes. Finally, the adhesion is assumed to be in the limit of strong adhesion. According to [50], the bending energy can then be neglected and the total energy can be considered as only consisting of the elastic stretching energy and the adhesion energy

$$U = K_{\mathrm{a}} \frac{(A - A_0)^2}{A_0} - A_f |W_{\mathrm{a}}|, \tag{1.1}$$

where A_0 is the surface area of undeformed vesicles, A is the surface area of deformed vesicles, A_f is the contact area, K_a is the elastic area compressibility modulus and W_a is the adhesion energy per unit area. Minimizing Eq. 1.1 with respect to A_{f}

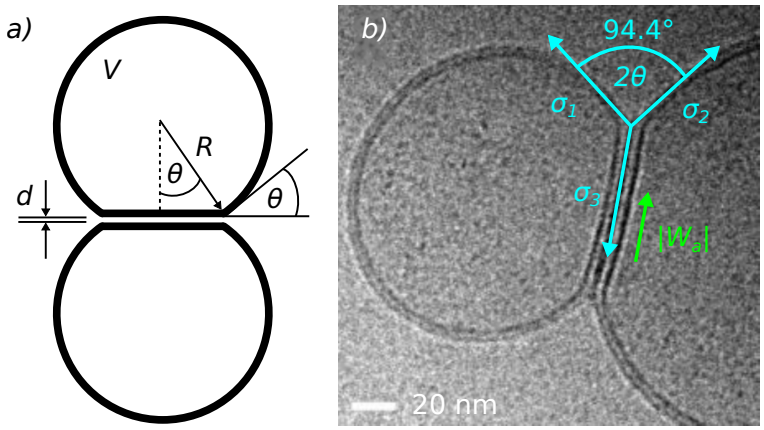

Fig. 1.5: a) Illustration of the geometry of two equally sized adhering vesicles, adapted from [50]. (b) Cryo-electron microscopy image of two vesicles arrested in a SNARE-mediated docking state, figure taken and modified from [23]. The balance of forces with the elastic stretching tensions $\sigma_1, \sigma_2, \sigma_3$ and the inter-membrane interaction $|W_{\mathrm{a}}|$ is indicated.

yields the equilibrium condition, from which the equilibrium contact angle θ and the equilibrium adhesion energy $|W_a|$ can be found. Assuming a perfect sphere for undeformed vesicles the volume V_0 and the surface area A_0 are given by

$$V_0 = \frac{4}{3}\pi R_0^3 \tag{1.2}$$

and

$$A_0 = 4\pi R_0^2 \,, \tag{1.3}$$

whereas for adhered vesicles assuming a spherical cap geometry the volume V and the surface area A are given by

$$V = \frac{\pi}{3}R^3(1+\cos(\theta))^2(2-\cos(\theta)) \tag{1.4}$$

and

$$\begin{aligned} A_c &= 2\pi R^2(1+\cos(\theta)) \\ A_f &= \pi R^2 \sin^2(\theta) \\ A &= A_c + A_f = \pi R^2(1+\cos(\theta))(3-\cos(\theta)) \,. \end{aligned} \tag{1.5}$$

Here the surface areas A_c and A_f correspond to the curved and the flat part of the deformed vesicles, respectively, and θ is the half of the contact angle as indicated in Fig. 1.5. Using the volume constraint $V = V_0$, R can be expressed in terms of R_0 as

$$R = R_0 \left[\frac{4}{(1+\cos(\theta))^2(2-\cos(\theta))} \right]^{1/3} . \tag{1.6}$$

The total energy is then [50]

$$\begin{aligned} U = {} & 4\pi R_0^2 K_a \left(\frac{(3-\cos(\theta))}{4^{1/3}(1+\cos(\theta))^{1/3}(2-\cos(\theta))^{2/3}} - 1 \right)^2 \\ & - 4\pi R_0^2 |W_a| \left(\frac{(1-\cos(\theta))}{4^{1/3}(1+\cos(\theta))^{1/3}(2-\cos(\theta))^{2/3}} \right) . \end{aligned} \tag{1.7}$$

By minimizing Eq. 1.7 with respect to θ the adhesion energy per unit area is obtained as [50]

$$|W_a| = 2K_a(1-\cos(\theta)) \left[\frac{3-\cos(\theta)}{\left(2(1+\cos(\theta))^{1/2}(2-\cos(\theta))\right)^{2/3}} - 1 \right] . \tag{1.8}$$

This expression for the adhesion energy can be also derived directly from the Young-Dupré equation $2\sigma\cos(\theta) = 2\sigma - |W_a|$, where $\sigma = (1/2)K_a(A - A_0)/(A_0)$ is the elastic stretching tension [52]. Figure 1.5(b) shows a cryo-electron microscopy image of a SNARE-mediated vesicle docking state as well as the balance of forces with the elastic stretching tensions σ_1, σ_2, σ_3 and the inter-membrane adhesion interaction $|W_a|$. With the assumptions made in the discussion and further with the simplification $\sigma = \sigma_1 = \sigma_2$ and $\sigma_3 = 2\sigma$ the adhesion energy is $|W_a| \approx 0.0034\ \mathrm{J/m^2}$ corresponding to $0.82\ k_BT/\mathrm{nm^2}$ for a contact angle of $2\theta = 94.4°$, and with the literature value of $K_a = 243\ \mathrm{mN/m}$ for phosphatidylcholines bilayers [53]. For comparison, the total zippering energy of $\sim 70k_BT$ has been recently reported for a single SNARE complex [54, 55].

Van der Waals attraction and hydration repulsion

Adhesion of lipid bilayers is governed by the interplay of various interfacial forces. These forces can be either short- or long-range, attractive or repulsive, and further, they can be of electrostatic and/or of entropic nature. In equilibrium, these interaction forces predict well-defined interbilayer spacings.

For charge neutral lipid bilayers in close proximity the interaction potential can be well described by the sum of van der Waals attraction and hydration repulsion [56]. Van der Waals interactions between molecules are universal and always attractive. The attraction results from different polarizabilities of lipid and water molecules. The interaction pressure P can be calculated in the framework of Lifshitz theory [57, 58]. For lipid bilayers, a widely used approximation of the van der Waals interaction pressure is given by

$$P_{\mathrm{vdW}}(d_h) = \frac{H}{6\pi}\left[\frac{1}{d_h^3} - \frac{2}{(d_h + d_{\mathrm{CH_2}})^3} + \frac{1}{(d_h + 2d_{\mathrm{CH_2}})^3}\right], \tag{1.9}$$

where H is the Hamaker coefficient in the units of energy [59]. Here, the proximal hydrophilic headgroup regions and the water layer in between are modeled as one homogeneous layer with the thickness $d_h = d_w + 2d_{hg}$, so that the bilayer is treated as a hydrocarbon layer with the thickness $d_{\mathrm{CH_2}}$ [59, 56].

The van der Waals attraction is balanced by strong repulsive forces acting between lipid bilayers on the nanometer scale, referred to as hydration repulsion, resulting from the orientation of water molecules close to the surface. For bilayer separations $d_w \gg \lambda_h$,

the hydration repulsion can be approximated by [60, 61]

$$P_{\mathrm{hyd}}(d_{\mathrm{w}}) = P_{\mathrm{h}} \exp\left(-\frac{d_{\mathrm{w}}}{\lambda_{\mathrm{h}}}\right) , \tag{1.10}$$

where the decay length λ_{h} typically is in the range of 1 to 3 Å. The exponential hydration repulsion is suggested to be universal and of entropic nature within the approximated distance regime. At smaller separations and consequently for smaller degrees of hydration, however, the interaction pressure is generally not following an exponential law and depends mainly on the chemical characteristics of the headgroups [62].

Interaction potentials between charged lipid bilayers

Electrostatic interactions are ubiquitous in soft matter and biological systems, and many biological processes and structures can be found, where charge-mediated interaction is the primary driving force [63, 64].

One famous example is given by DNA packaging in the cell nucleus, where all highly negatively charged DNA is densely packed as a nucleoprotein complex called chromatin. On the lowest level of the multi-hierarchical structure, a short DNA section is wrapped around a positively charged histone protein and partially and electrostatically neutralized [63, 65]. In the physical point of view, it is of interest to understand the ion distributions near charged surfaces and the resulting and divers interaction phenomena between two charged surfaces.

Two like-charged objects in vacuum always repel each other, but once they are surrounded by an electrolyte the system becomes more complicated. It was shown, that mean-field approaches such as the Poisson-Boltzmann theory yield always repulsion between like-charged objects [66]. In the mean-field approximation, the counterions are rather loosely bound at the charged surface and form a diffuse ionic cloud, where correlations between the counterions are neglected as illustrated for two plates in Fig. 1.6(a). At the same time, like-charge attraction is possible in the presence of counterions, which experimentally has been known since the 1980ies [67, 68, 69, 70]. Quite a bit counterintuitively, such an attraction only occurs when the surface charge density is high enough. In this scenario, mean-field approximations, even though successful in describing many weak-coupling phenomena, fail to describe the like-charge attraction, and electrostatic correlations between counterions have to be considered, illustrated in Fig. 1.6(b). It is now the strong coupling theory, which predicts the

like-charge attraction of highly charged bodies when surrounded by counterions [71, 72, 63, 73]. For the simplest case of two like-charged planar plates at small separations, an analytical expression for the interaction pressure was found two decades ago by R. NETZ and coworkers [74].

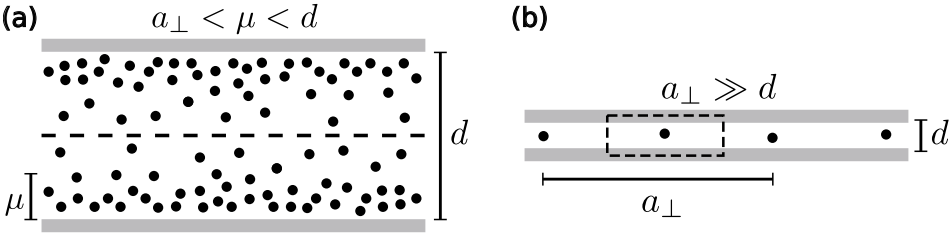

Fig. 1.6: Illustration of (a) the electrostatic mean field scenario accurately described by Poisson-Boltzmann theory, and (b) of the strong coupling scenario in the case of two like-charged plates. The scenarios are obtained by comparing the Gouy-Chapman length μ, the interplate separation d and the lateral distance between counterions $a_\perp$. Figure adapted from [72].

In the following, we first introduce the characteristic length scales relevant for the interaction between two membranes following the literature in [75, 76, 72].

The Bjerrum length is defined as the distance between two unit charges at which the electrostatic energy equals the thermal energy $k_\mathrm{B}T$ and is denoted by

$$l_\mathrm{B} = e^2(4\pi\epsilon\epsilon_0 k_\mathrm{B}T)^{-1} \,. \tag{1.11}$$

Here, $e \simeq 1.602 \cdot 10^{-19}$ C is the elementary charge, $\epsilon_0 = 8.85 \cdot 10^{-12}$ F/m is the vacuum permittivity, ϵ is the relative permittivity of a medium (≈ 80 for water at room temperature), $k_\mathrm{B} \simeq 1.381 \cdot 10^{-23}$ J/K is the Boltzmann constant, and T is the temperature in the units of K.

The Gouy-Chapman length, defined as the distance between a planar surface and a unit charge at which the electrostatic energy equals the thermal energy, is expressed as

$$\mu = (2\pi q l_\mathrm{B}\sigma_\mathrm{s})^{-1} \,, \tag{1.12}$$

where q is the valency of the counterions and σ_s is the surface charge density.

The Debye screening length is

$$\lambda_\mathrm{D} = \left(\frac{\epsilon_0 \epsilon_r k_B T}{\sum_i n_{0,i} e^2 q_i^2} \right)^{1/2} \,, \tag{1.13}$$

where $n_{0,i}$ is the number density of ions species i. At this characteristic length scale the electrostatic interactions between two charges in the presence of all other ions of the solution are screened.

The ratio of the rescaled Bjerrum length $\tilde{l}_\mathrm{B} = q^2 l_\mathrm{B}$ and the Gouy-Chapman length μ gives the important electrostatic coupling parameter

$$\Xi = \tilde{l}_\mathrm{B}/\mu = 2\pi q^3 l_\mathrm{B}^2 \sigma_\mathrm{s} \,. \tag{1.14}$$

The coupling parameter uniquely describes the physical regimes of the system and discriminates weakly coupled cases from those which are strongly coupled [71]. Experimentally relevant, the coupling parameter can be tuned by varying the surface charge density σ_s or the valency of the ions q.

For $\Xi \ll 1$, corresponding to the weak coupling regime, the Gouy-Chapman length μ is relatively large and the distribution of the counterions can be well described by the Poisson-Boltzmann theory in the mean-field approximation. Contrary, large coupling parameters, where $\Xi \gg 1$, describe the limit of the strong coupling regime, and the Gouy-Chapman length μ is relatively low. In this regime, the counterions are strongly correlated and form a quasi two-dimensional layer at the charged surface.

The structure of the counterionic layer is characterized by the typical distance between the counterions at the surface. Using the local electroneutrality condition, the typical lateral separation for counterions in the vicinity of the charged surface is

$$a_\perp \sim \sqrt{\frac{q}{\sigma_\mathrm{s}}} \,. \tag{1.15}$$

In the strong coupling regime, the lateral separation of the counterions is much larger than the interplate separation, $a_\perp \gg d$.

Weak-coupling regime

As discussed above, for weakly coupled cases, where $\Xi \ll 1$, mean-field approaches such as the Poisson-Boltzmann theory hold. The Poisson-Boltzmann theory gives a precise description of the ion density distribution near a charged wall at physiological conditions, e.g. for monovalent ions and low or moderate surface charge density [75, 76, 72].

For counterions only, the Poisson-Boltzmann equation reads [52]

$$\nabla^2\Psi(\vec{x}) = -\frac{qe\rho_0}{\epsilon\epsilon_0}\exp\left(-\frac{qe\Psi}{k_\mathrm{B}T}\right), \tag{1.16}$$

which is to be solved for the electrostatic potential $\Psi(\vec{x})$. For the case of a single planar plate and counterions only, the Poisson-Boltzmann equation predicts a counterion density profile of the form [52]

$$\rho_\mathrm{PB}(z) = \frac{2\pi l_\mathrm{B}\sigma_\mathrm{s}^2}{(z/(1+\mu)^2)}, \tag{1.17}$$

which describes an extended, i.e. algebraically decaying, ionic cloud with the distance z from the surface. Although the counterion profile is diffusive at the surface, the typical thickness of the ionic layer can be described by μ as it equals the height of the layer which contains half of the counterions.

For the case of two like-charged plates with low or moderate surface charge density in the presence of an 1:1 electrolyte ($q_\pm = 1$, e.g. NaCl), analytical solutions of the Poisson-Boltzmann equation are a good approximation predicting the interplate separation. However, analytical solutions can only be calculated when separating the general solution into several limits. By length scale analysis, four different regimes can be distinguished, namely the Debye-Hückel regime, the Gouy-Chapman regime, the Ideal-Gas regime, and the intermediate regime [75, 76]. The different regimes are indicated in Fig. 1.7 as a function of the dimensionless variables μ/λ_D and d/λ_D.

Following [75, 76], the Debye-Hückel regime is valid for small surface potentials, i.e. for small surface charge densities, and is separated into two Debey-Hückel regions, Debye-Hückel 1 and Debye-Hückel 2, for large and for small separation d, respectively. For large separations, valid for $d \gg \lambda_\mathrm{D}$ and $\mu \gg \lambda_\mathrm{D}$, the interaction pressure reads

$$P(d) = \frac{2k_\mathrm{B}T}{\pi l_\mathrm{B}\mu^2}\exp\left(-\frac{d}{\lambda_\mathrm{D}}\right). \tag{1.18}$$

In the other limit of small separation, valid for $d \ll \lambda_\mathrm{D}$ and $\mu \gg \lambda_\mathrm{D}^2/d$, the interaction pressure is approximated by

$$P(d) = \frac{2k_\mathrm{B}T}{\pi l_\mathrm{B}\left(\lambda_\mathrm{D}^{-1}\mu\right)^2}\frac{1}{d^2}. \tag{1.19}$$

In the intermediate regime the distance d is the largest length-scale and the surface is

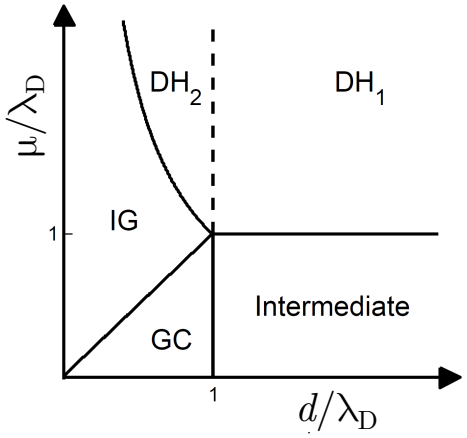

Fig. 1.7: Schematic representation of the different regimes (Ideal gas, Gouy-Chapman, Intermediate and Debye-Hückel) of the Poisson-Boltzmann equation for two flat and like-charged plates at separation d, figure adapted from [76]. The regimes are separated with respect to the independent and dimensionless variables d/λ_D and μ/λ_D with the Gouy-Chapman length μ and the Debye length λ_D.

strongly charged ($\lambda_D \gg \mu$). This regime is valid for $d \gg \lambda_D \gg \mu$, and the interaction pressure is given by

$$P(d) = \frac{8k_BT}{\pi l_B \lambda_D^2} \exp\left(-\frac{d}{\lambda_D}\right) . \tag{1.20}$$

The Ideal-Gas regime and the Gouy-Chapman regime both represent the regimes that are obtained for the counterion only case. In the Ideal-Gas regime both the surface charge density and the concentration of the counterions is small, resulting in a nearly constant distribution of the counterions between the two surfaces. Consequently, the main contribution to the electrostatic interaction is given by the entropy of the counterions. The interaction pressure, valid for $\lambda_D^2/d \gg \mu \gg d$, is written as

$$P(d) = \frac{k_BT}{\pi l_B \mu} \frac{1}{d} . \tag{1.21}$$

Finally, the interaction pressure in the Gouy-Chapman regime, valid for $\lambda_D \gg d \gg \mu$, is expressed as

$$P(d) = \frac{\pi k_BT}{2l_B} \frac{1}{d^2} . \tag{1.22}$$

In this regime, the surface charge density is large at low concentrations of the counterions. Note that the Gouy-Chapman regime is already close to the limit of the validity

of the weak-coupling limit due to strong electrostatic interaction.

Strong-coupling regime

The strong coupling regime is described in the limit of $\Xi \gg 1$. We consider two identically charged parallel planar surfaces at distance d that are neutralized by counterions yielding global electro-neutrality. Further the dielectric permittivity of the solvent and of the plates are assumed to be equal, and counterions are assumed point-like, and all of the same charge. As discussed above, the lateral correlation length between the counterions is larger than the interplate separation, $a_\perp \gg d$. Since the counterions are highly separated from each other, a single counterion confined by the two plates can be considered as a correlation cell as sketched in Fig. 1.6(b). In this scenario, the inter-ionic energy per particle is small compared to $k_\mathrm{B}T$, so that ion-ion interactions can be neglected [77]. The effective interaction pressure between the plates is than mainly dominated by the contribution from each single correlation cell. This enables us to get a quite intuitive insight into the electrostatic strong-coupling phenomenon. Following [71, 74], we consider two symmetrically charged plates confining a neutralizing single counterion. The distance between the plates with the area A is denoted as d, and the distance between the plates and the counterion as z and $d - z$, respectively. For $d \ll \sqrt{A}$, the electrostatic interaction energy between the counterion and the plates is $W_1 = 2\pi k_\mathrm{B}T l_\mathrm{B} q \sigma_\mathrm{s} z$ and $W_2 = 2\pi k_\mathrm{B}T l_\mathrm{B} q \sigma_\mathrm{s}(d - z)$, respectively, which follows from the evaluation of the potential at an infinite charged wall. The interaction energy between the two plates is proportional to $A\sigma_\mathrm{s}$ (total charge on one plate), and given by $W_{12} = -2\pi k_\mathrm{B}T A l_\mathrm{B} \sigma_\mathrm{s}^2 d$, again for $d \ll \sqrt{A}$. The total energy is then $W = W_1 + W_2 + W_{12} = 2\pi k_\mathrm{B}T A l_\mathrm{B} \sigma_\mathrm{s}^2 d$. The total electrostatic pressure per unit area reads

$$P_\mathrm{el} = -\frac{\partial(W/A)}{\partial d} = -2\pi k_\mathrm{B}T l_\mathrm{B} \sigma_\mathrm{s}^2 \,, \tag{1.23}$$

indicating that the two plates attract each other. In addition, the entropic contribution of the order $S \sim k_\mathrm{B} \ln d$ accounts for the counterion confinement resulting in a repulsive term. The entropic pressure, calculated by the relation $P = T(\mathrm{d}S/\mathrm{d}V)$ with the volume $V = Ad$, reads

$$P_\mathrm{ent} = \frac{k_\mathrm{B}T}{Ad} = \frac{2\sigma_\mathrm{s} k_\mathrm{B}T}{qd} \,, \tag{1.24}$$

since the system is electro-neutral with the condition $q = 2A\sigma_s$. Eventually, the total pressure is given by

$$P = P_{el} + P_{ent} = -2\pi k_B T l_B \sigma_s^2 + \frac{2\sigma_s}{qd} = 2\pi k_B T l_B \sigma_s^2 \left(-1 + \frac{2\mu}{d}\right) . \tag{1.25}$$

This expression predicts a bound state between the plates with an equilibrium separation of $d^* = 2\mu$. As a consequence, the like-charged plates attract or repel each other for $d > d^*$ and $d < d^*$, respectively. The result obtained for the total pressure in Eq. 1.25 agrees with the precise description of the strong coupling theory in the limit of $\Xi \gg 1$ [71, 74].

An alternative approach to understand like-charge attraction in the strong coupling regime has been given by E. TRIZAC [77]. Accordingly, the unbinding of counterions from the vicinity of the plates is crucial for like-charge attraction, when d is small enough. In this scenario, the counterions can freely explore the space perpendicular to the plates, described by a constant distribution

$$\rho_{sc}(z) = 2\pi l_B \sigma_s^2 \frac{2\mu}{d} , \tag{1.26}$$

while they are correlated laterally, i.e. parallel to the surface of the plates. It was shown from the contact theorem, that only then attraction between like-charge plates can set it [77]. Contrarily, the counterions are bound to the charged surface in the case of a single plate with an exponentially decaying counterion distribution of the form [71]

$$\rho_{sc}(z) = \rho_0 \exp\left(-\frac{z}{\mu}\right) , \tag{1.27}$$

in the strong coupling limit.

1.3 X-ray structure analysis of vesicles

Since the discovery of X-rays by Wilhelm Conrad Röntgen in 1895 [78], they have played a tremendous role in the structural elucidation of matter. The first X-ray scattering experiments on membranes, by F. O. Schmitt, G. Boehm and coworkers in the 1930 - 1940ies, were strongly motivated towards the structural elucidation of the brain and the nervous system [79, 80]. When analyzing the fine structure of nerve myelin, lipids were found to be the origin of observed diffraction peaks [80, 81]. In the following, more systematic studies were carried out by using purified "nerve lipides" such as

lecithin, cephalin, sphingomyelin, kerasin and prenosin isolated from beef spinal cord, concluding from the diffraction data, that the molecules occur as bimolecular leaflets [82]. It was only one decade earlier, that for the first time a lipid bilayer ("a layer of lipoids just two molecules thick") was proposed by E. Groter and F. Grendel in 1925, evidenced only by measuring the surface area of extracted chromocyte lipids arranged in a monolayer and by comparison to the total surface area of one chromocyte [83].

Since then, different lipid model membrane systems are widely used for X-ray structural studies addressing a broad range of biophysical and physiological questions [84, 85, 86, 87]. One main objective of this thesis is the structural investigation of membrane/vesicle adhesion and fusion. X-ray crystallography has provided the structural basis to elucidate the function of proteins, which play an important role in membrane merger (e.g. SNARE proteins as discussed earlier). From a structural point of view, membrane fusion intermediates and the role of specific types of lipids have been rather elusive due to both short time and small length scales at which structural rearrangement of the lipids takes place.

Stalk structures arrested in an equilibrium state have been extensively studied in solid-supported aligned multi-bilayers under partial dehydration by X-ray diffraction and reflectivity [88, 34, 89]. The critical water layer thickness between opposing bilayers at which a stalk begins to form was found to be approximately constant, $d_{\mathrm{w}}^{*} = 9 \pm 0.5$ Å, for different lipid compositions [34]. Recent effort has been made to extend the X-ray studies of membrane fusion in supported multi-bilayers towards physiological conditions by incorporation of SNAREs into the bilayer stack [90]. However, X-ray stalk structures in the presence SNAREs could not be observed so far. The ability to observe stalks in supported multi-bilayers depends on the ability of the multi-bilayer system to form a particular equilibrium lipid mesophase, namely the rhombohedral phase. In the preparation of multi-bilayers with reconstituted SNAREs, however, the SNAREs come with detergents. The latter was shown to impair the formation of the rhombohedral phase [90]. A further limitation of these experiment is, that important parameters such as pH or ionic strength can not be easily applied in such a setup.

It is therefore of interest, to study model membrane systems in fully hydrated states. In this work, we use small unilamellar vesicles with radii from approximately 30 - 50 nm, with a focus on both pure lipid vesicles and on vesicles with reconstituted SNARE, referred to as SNARE proteoliposomes. There has been great progress in the last decade in order to distinguish intermediates in the SNARE proteoliposome fusion pathway, e.g. docking, hemifusion and fusion, in view of kinetics and structures by

employing a wide range of biophysical techniques, for example, fluorescence-cross-correlation-spectroscopy combined with Förster resonance energy transfer (FCCS-FRET) [91, 92], dynamic light scattering (DLS) [93], cryo-electron microscopy (cryo-EM) [94, 23, 95]. In vitro, formation of the SNAREs synaptobrevin, syntaxin and SNAP-25 to a coiled-coil complex is sufficient to drive membrane fusion [91, 23]. In practice, a system of two populations of vesicles, either containing synaptobrevin or the acceptor complex (also referred to as the ΔN-complex), are widely used to study SNARE-mediated vesicle fusion. Interestingly, it was shown that mutants of synaptobrevin 2, e.g. synaptobrevin Δ84 lacking the 84^{th} residue which corresponds to the $+8^{\text{th}}$ layer in the SNARE complex, lead only to partial zippering of the SNARE complex resulting in stable docking of the vesicles with an extended interface between two opposing membranes [23]. This docking intermediate is found to be irreversible after NSF/α-SNAP-mediated disassembly of the SNARE complex [96]. Recently, a docking state has also been reported in the context of influenca virus fusion with a target membrane mediated by hemagglutinin fusion proteins [97]. Thus there is evidence that a tightly docked interface could be a part of a protein-mediated membrane fusion pathway.

However, important detailed structural information on the length scale of the membrane are not accessible by these techniques. What are the bilayer structure and the inter-bilayer water spacing on a sub-nanometer scale? Small-angle X-ray scattering (SAXS) is an established technique to study the structure of lipid vesicles, and in particular of the lipid bilayer, in solution, both in the multilamellar as well as in the unilamellar state [98, 99, 100]. With the availability of highly brilliant synchrotron radiation, SAXS experiments on biological samples in solution can be performed at low concentrations and short exposure times. In the last decades, much progress has been made in the analysis of vesicle SAXS data [100, 87]. A common approach is the direct modeling of SAXS data, i.e. fitting a model function to the SAXS intensity profile using non-linear least-squares methods. In general, this model-based approach requires some basic knowledge about the structure of the measured objects in order to find an effective expression for the one-dimensional electron density profile $\rho(\vec{r})$, projected onto the bilayer normal. In the literature, different models have been reported, such as strips of constant values or Gaussian functions accounting for different regions within the lipid bilayer representing distinct chemical moieties [101, 99]. Note, that the lipid bilayer generally represents an intrinsically disordered ensemble described by collective phenomena of lipids, which is why atomic resolution can not be achieved by X-ray diffraction. However, the headgroup of a phospholipid contains an electron-rich phosphate group, which results in a large electron density contrast between the

headgroups and the surrounding hydrocarbon and aqueous region. In particular the effective bilayer thickness can be well measured in SAXS experiments, which is often defined as the distance between the phosphate groups [99]. Note, that the boundary between the lipid bilayer and the aqueous surrounding is rather diffuse. More refined descriptions of the lipid bilayer have been reported by using the scattering density profile (SDP), where volume distribution functions are calculated for several quasi-molecular fragments of the bilayer, supported by comparison to molecular dynamics (MD) simulations [102, 103]. Such models were used to jointly analyze SAXS and SANS (small-angle neutron scattering) data to increase the level of structural information.

Beyond pure lipid vesicles, SAXS analysis has been extended towards more complex systems such as purified organelles [104, 105], or Escherichia coli cells [106]. In this thesis, we follow [104, 107] for analysis of SAXS data obtained from SVs. The SV membrane is densely packed with proteins. It was shown, that only a SAXS model, where the structure of the protein shell was considered laterally anisotropic, was sufficient to describe SAXS data obtained from SVs. While the lipid bilayer is still conventionally modeled by a sum of three Gaussian functions, Gaussian chain models are used to describe the inner and outer protein layers, and effectively model distinct protein patches characterized by their radius of gyration and the number of protein patches on the surface, thus breaking spherical symmetry. This model enables to obtain detailed structural information about the protein layers and the lipid bilayer. Contributions of (transmembrane) proteins to the lipid bilayer are not directly modeled but included in the bilayer model. The polydisperse ensemble is further modeled by a bimodal size-distribution accounting for the size polydispersity of the SVs, and for contamination resulting from SV purification.

Recently, extracellular vesicles (EVs) have been extensively studied structurally, and are potentially interesting organelles for medical therapy [105, 108]. Surprisingly, and maybe not surprising at all, the SAXS signal of EVs shows a large similarity to those obtained from SVs [105]. In contrast to SVs, SAXS analysis was performed by using an isotropic SAXS model consisting of a spherical core-shell model. In the case of SVs, isotropic model fits did not yield satisfactory fits. One possible reason for this might be the difference in size; EVs have a size distribution ranging from 100 - 200 nm in radius, an order of magnitude larger than the sizes measured for SVs [104].

Beyond static structure, structural dynamics of vesicles is highly relevant for the understanding of functional processes. Numerous processes can only be fully understood, when we unravel the structural rearrangements, e.g. of molecular assemblies or of

morphological membrane transitions, as a function of time. With modern synchrotron sources it has now become possible to study structural dynamics with millisecond time resolution [109, 110]. Besides the ability to probe kinetics, we demonstrate in Chapter 3 that intermediate steps in the transition from unilamellar to multilamellar vesicles can only be made visible by employing time-resolved SAXS, in this case using the stopped-flow rapid-mixing technique [109]. For time-resolved SAXS, controlled mixing is crucial, which can be achieved either by stopped-flow rapid mixing, or alternatively and on different time scales by microfluidics [111, 112, 113].

Microfluidics devices enable the manipulation of small amounts of fluids within micron-scale channels in a very controllable manner, and are thus suitable for precise mixing [114]. Given small Reynolds-numbers [115], the flow is characteristically laminar and mixing is diffusion-limited. In continuous flow, mixing occurs while the sample flows, so that temporal resolution can be potentially achieved by measuring the signal at different positions along the stream, corresponding to probing different reaction times. The accessible time resolution, i.e. smallest observable reaction time by minimizing the dead time, can be in principle on the order of 100 μs [116], well below the accessible time resolution in the millisecond range achieved by stopped-flow rapid-mixing devices. A further advantage is the fact that by constant replenishment of sample radiation damage can be outrun. In microfluidics SAXS, the time resolution depends not only on the flow characteristics such as flow velocity, but also on the focal spot size of the X-ray beam. At the same time, real-space resolution determined by the focal spot size of the beam enables to probe the detailed spatial heterogeneity of a system within the microfluidic flow [117]. With recent improvements in X-ray optics, the focal spot size of the X-ray beam can be in principle reduced down to the nanometer range [118], however, a smaller beam size comes at the cost of a lower signal-to-noise ratio of the SAXS signal. Exploratory microfluidics SAXS experiments are presented in Chapter 3 to evaluate the suitability to study vesicle adhesion and fusion upon mixing with divalent salts, also in view of future extensions towards probing the structure of physiologically relevant states of SVs in microfluidic flows. Note that the potential down-scaling of the total volume which can be achieved by microfluidics is in particular important for samples, which can not be easily obtained in large amounts, such as in the case of isolated SVs.

Vesicle adhesion and fusion studied by small-angle X-ray scattering

2

Karlo Komorowski, Annalena Salditt, Yihui Xu, Halenur Yavuz, Martha Brennich, Reinhard Jahn, and Tim Salditt
Reproduced from Biophysical Journal **114**, 1908-1920 (2018)

We have studied the adhesion state (also denoted by docking state) of lipid vesicles as induced by the divalent ions Ca^{2+} or Mg^{2+} at well controlled ion concentration, lipid composition, and charge density. The bilayer structure and the interbilayer distance in the docking state were analyzed by small-angle X-ray scattering (SAXS). A strong adhesion state was observed for DOPC:DOPS vesicles indicating like-charge attraction due to ion-correlations. The observed interbilayer separations of ~ 1.6 nm agree quantitatively with the predictions of electrostatics in the strong coupling regime. While this phenomenon was observed when mixing anionic and zwitterionic (or neutral) lipids, pure anionic membranes (DOPS) with highest charge density σ resulted in a direct phase transition to a multilamellar state, which must be accompanied by rupture and fusion of vesicles. To extend the structural assay towards protein-controlled docking and fusion, we have also characterized reconstituted *N*-ethylmaleimide-sensitive factor attachment protein receptors (SNAREs) in controlled proteo-liposome suspensions by SAXS.

2.1 Introduction

Membrane fusion is an ubiquitous physiological process, both on the cellular and subcellular level. A well known example is the fusion of neurotransmitter-filled synaptic vesicles with the presynaptic plasma membrane [4]. The fusion and the subsequent release of neurotransmitters are essential for nerve conduction, which is mediated by proteins known as soluble *N*-ethylmaleimide-sensitive factor attachment protein

receptors (SNAREs) [17]. Neuronal SNAREs comprise both synaptobrevin 2 (Syb), situated in the membrane of the synaptic vesicle, as well as syntaxin 1a (Syx) and SNAP-25 (SN25), which in turn are anchored in the presynaptic plasma membrane. According to the zippering hypothesis, the N- to C-terminal assembly to a four-helix bundle, named the SNARE complex, provides the driving force to bring opposing membranes into close contact and therefore initiates the merger [17].

Despite significant experimental efforts, e.g. [23, 94], many important details of the membrane fusion pathway, in particular concerning intermediate structures of the membrane and the corresponding energy barriers, are still under debate. At the same time, numerical studies have provided interesting insight into possible structures and mechanisms [119, 37], which in turn require experimental verification. From studies of multilamellar model membranes, we know that the planar bilayer topology becomes unstable upon dehydration, and stalks begin to form for certain lipids once that a critical (minimal) water layer thickness d_w is reached between opposing bilayers [88, 34, 89, 120, 90]. A limitation of these experiments is the fact that the critical osmotic pressure is extremely high and cannot be reached in solution, but requires partial hydration in vapor pressure chambers. Important biochemical and biophysical parameters such as ionic strength cannot be used in such a setup. It is therefore of interest to investigate the equilibrium spacing between adhering lipid vesicles in solution, in particular in the presence of controlled concentrations of monovalent or divalent ions such as Ca^{2+}. In particular, it is important to see whether adhesion and eventually fusion can be induced by controlled variation of divalent ion concentration, and to quantify the corresponding electrostatic forces [75, 71]. Experimentally, adhesion and fusion can be studied both in protein-free vesicles induced by Ca^{2+}, as well as in vesicles with reconstituted SNAREs (also denoted as proteo-liposomes), since reconstitution protocols are well established [23].

In this work, we use small-angle X-ray scattering (SAXS) as a well established technique for structure analysis of lipid vesicles in solution [99, 101, 121] to characterize the adhesion (or docking) state of vesicles. To this end, we primarily address 'physical' adhesion induced by Ca^{2+} in pure lipid vesicles. We hence provide an experimental investigation of the contact zone, which has also received much attention in recent MD simulations [122, 123, 124]. Importantly, we find that the interbilayer distance in the strong adhesion state is governed by condensation of divalent counterion according to the regime of strong coupling [71]. In the outlook, we present first SAXS experiments using vesicles with reconstituted SNAREs. For the latter, we use the mutant SybΔ84 which was shown to induce adhesion, but not to promote full fusion [23]. In this

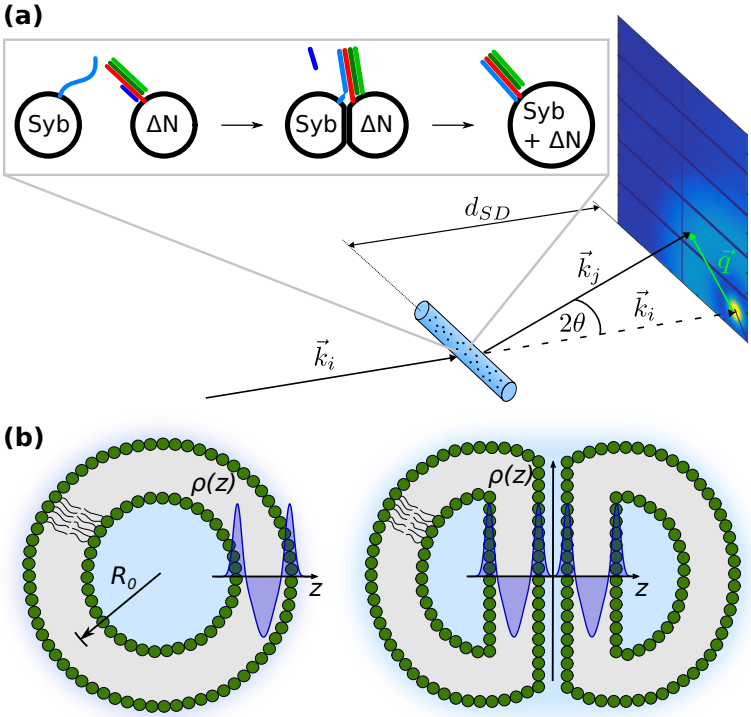

Fig. 2.1: (a) Small-angle X-ray scattering geometry and isotropic two-dimensional diffraction pattern as measured by an area detector (here, scattering from DOPC:DOPE (1:1) vesicles). The distance between the sample plane and the detector is denoted by d_{SD}. The momentum transfer vector is given by $\vec{q} = \vec{k}_j - \vec{k}_i$, where $\vec{k}_i$ and $\vec{k}_j$ are the wave vectors of the incident and the scattered X-ray beam, respectively. (b) Sketch of a 'free' vesicle with the radius R_0 (left) and of two docked vesicles with an extended interface between two opposing bilayers (right). For both illustrations three Gaussians describing the EDP $\rho(z)$ of a bilayer are indicated (one Gaussian for each headgroup region and one Gaussian for the hydrophobic chain region).

way, intermediate states of a SNARE-mediated liposome fusion pathway could be made accessible for SAXS. Note that the adhesion state of both protein-free vesicles and proteo-liposomes, with two bilayers brought into close apposition, is likely to be governed by strong electrostatic and osmotic forces.

The main aim of the present work is hence to probe the bilayer structure and the interbilayer water spacing d_w with molecular resolution, as quantified by the electron density profile (EDP) normal to the membranes. Following suitable preparation protocols of vesicles, the first challenge is the preparation and identification of the adhesion or docking state. As a long term goal we want to control and distinguish a non-reacted, a docked and a fused state, as illustrated in Fig. 2.1.

We thus first address vesicle preparation, protein reconstitution, and SAXS analysis in the Materials and Methods section following this introduction. Subsequently, results will be presented and discussed, first for non-interacting unilamellar lipid vesicles, and then for the adhesion state of vesicles induced by $CaCl_2$ and $MgCl_2$. The interbilayer distances obtained from adhered vesicles will be discussed in terms of interaction potentials. The paper will close with an outlook towards X-ray structural investigations of SNARE-mediated liposome docking and fusion and with a summary of the main findings. Auxiliary data sets and further evaluations as well as additional technical details are included as Supporting Material A.1.

2.2 Materials and Methods

2.2.1 Preparation of vesicles

The lipids dioleoylphosphatidylcholine (DOPC), dioleoylphosphatidylethanolamine (DOPE), dioleoylphosphatidylserine (DOPS), and cholesterol (Chol) were purchased as lyophilized powders from Avanti Polar Lipids (Alabaster, AL, USA). As a first step, the lipids were dissolved in chloroform and mixed at the desired molar ratio. Chloroform was then evaporated under a stream of nitrogen. The resulting dried lipid film was subsequently hydrated with ultra-pure water (Milli-Q) to a final lipid concentration of either 5 mg/ml for DOPC:DOPE:DOPS:Chol, or 10 mg/ml for all other lipid mixtures. To achieve a homogeneous phase, the mixture was sonicated to clarity using a tip sonicator (Bandelin, SONOPULS HD 3100) with the following settings: amplitude 40 %, pulse duration 0.5 s/0.5 s, at least five times 60 s with cooling periods on ice. After sonication, the vesicle suspension was stepwise extruded through polycarbonate

membranes with pore sizes of 100 nm, 50 nm and 30 nm in diameter (in that order, for each round 25 times) using a Mini-Extruder from Avanti Polar Lipids.

For the investigation of $CaCl_2$- and $MgCl_2$-induced vesicle adhesion, the DOPC-DOPS mixtures were hydrated with either ultra-pure water or a 100 mM glucose solution to a final concentration of 10 mg/ml and subsequently vortexed. Afterwards, the vesicles were extruded through membranes of a pore size of 100 nm in diameter. $CaCl_2$- and $MgCl_2$ suspended either in ultra-pure water or in a 100 mM glucose solution, were added to the vesicle suspension prior to the experiment.

Size distributions of the vesicles were quantified by dynamic light scattering (DLS), both for non-interacting vesicles (included as Supporting Material A.1, Fig. A.1) and for the calcium-induced adhesion state. DLS measurements were performed by using an ALV/CGS-3 DLS/SLS Laser Light Scattering Goniometer System (ALV GmbH Langen, Germany). The setup is equipped with a 22 mW polarized HeNe-Laser operating at a wavelength of $\lambda = 632.8$ nm (UNIPHASE, model 1145P), and an ALV-7004 Multiple Tau Digital Correlator. Data analysis was performed with the ALV-Correlator Software (ALV-7004 for Windows, V.3.0.5.4), as previously described in [125].

2.2.2 Protein expression and purification

Expression and purification of SNAREs were performed by following the protocol in [23]. The SNAREs used in this work, synaptobrevin-2 (residues 1-116 [26] and 49-96 [126]), syntaxin-1A (residues 183-288) [26] and a cysteine-free variant of SNAP-25A (residues 1-206) [127], were derived from *Rattus norvegicus* and their constructs were cloned into expression vectors. Full-length syb(1-116) C28S was cloned into a pET28a vector containing His_6-tags. For the ΔN-complex (containing syb2(49-96), syx1A(183-288) and SN25(1-206)), the SNAREs were co-expressed using the pETDuet-1 vector for syb2(49-96) and syx1A(183-288) and the pET28a vector for SN25(1-206). All SNAREs were expressed in *Escherichia coli* strain BL21(DE3) and purified by Ni^{2+}-NTA (nickel-nitrilotiacetic acid) affinity chromatography followed by ion-exchange chromatography on the Äkta system (GE Healthcare). His_6-tags were removed by thrombin cleavage.

2.2.3 Preparation of SNARE-liposomes

The SNARE-liposomes were prepared by following the protocol in [23].

Briefly, DOPC:DOPE:DOPS:Chol (molar ratio of 5:2:2:1) liposomes were prepared in a 150 mM KCl, 20 mM HEPES, pH 7.4 buffer by reverse-phase evaporation and subse-

quently by extrusion through polycarbonate membranes. The lipids were dissolved in chloroform:methanol (2:1) and mixed at the desired molar ratio. Using a rotary evaporator the solvent was evaporated resulting in a dried lipid film. The lipid film was re-dissolved in 1.5 ml diethyl ether and 0.5 ml of the buffer was added. The resulting mixture was sonicated using a thin tip sonicator (Branson Sonifier, 50 % duty cycle at low intensity, 3 x 45 s and cooling on ice after each sonification step for 45 s). Diethyl ether was removed from the emulsion by using again the rotary evaporator. Further buffer was added to the resulting liposome suspension to get a final lipid concentration of 8 mM. To get unilamellar liposomes with a mean radius of approximately 50 nm, the liposomes were extruded through polycarbonate membranes with a pore size of 0.4 μm, and with a pore size of 0.1 μm (each 25 times), in that order.

For SNARE reconstitution, the liposomes were mixed with n-OG (n-octyl-β-D-glucoside) and either with syb or the ΔN-complex purified in 1 % n-OG or CHAPS (3-[(3-cholamidopropyl)dimethylammonio]-1-propanesulfonate), respectively. The molar ratios of these mixtures were determined by the *R*-value, which describes the ratio of the concentration of n-OG above its critical micelle concentration to the concentration of the lipids (for details see [23]), and further by the lipid-to-protein ratio. For reconstitution of the ΔN-complex and of syb, the *R*-values were set to $R = 2$ and to $R = 1.5$, respectively, and the lipid-to-protein ratio was set to 500:1 at a final lipid concentration of 4 mM for both reconstitutions. In order to remove excess n-OG, two runs of dialysis against liposome buffer using Slide-A-Lyzer cassettes (Thermo Scientific) of a molecular weight cut-off of 2 kDa were performed at room temperature. In a first 'overnight' dialysis 2 g/l of adsorbent beads (SM-2-Bio-Beads, Bio Rad) were included, followed by a second run for approximately 4 hours.

2.2.4 Small-angle X-ray scattering

SAXS experiments were performed at the bending magnet beamline BM29 (BioSAXS) at the European Synchrotron Radiation Facility (ESRF) in Grenoble, France [128]. The photon energy was set to $E = 12.5$keV by a multilayer monochromator with $\Delta E/E \simeq 0.01$. The beam size at the sample plane was $(700 \times 700)\ \mu\text{m}^2$. The scattered X-rays were recorded using a pixel detector (Pilatus 1M, Dectris) with 981×1043 pixels of size $(172 \times 172)\ \mu\text{m}^2$, at a sample-to-detector distance of 2.867 m to cover a q-range of approximately 0.036 nm^{-1} to 4.95 nm^{-1}. By using the sample-changer robot, the samples were automatically loaded into a vacuum-mounted quartz-capillary of 1.8 mm in diameter for exposure. For this purpose, the samples were loaded into PCR tubes (in

general 50 μl per sample) and the matched buffers were loaded into microcentrifuge tubes (1-2 ml). For data acquisition, ten frames of one second were recorded for each sample, where a flow of the sample through the beam was generated to minimize radiation damage. For background subtraction the matched buffer was measured before and after each sample. Automatic raw data processing, including azimuthal integration to obtain the one-dimensional scattering curve $I(q)$, background subtraction and curve averaging (with a veto in case of radiation damage), was performed online by a processing pipeline within the *EDNA* framework [129].

2.2.5 Form and structure factor models

SAXS analysis of lipid vesicles is well covered in literature. In this work we largely follow [98, 99]. However, we briefly repeat the scattering equations for notational clarity, and as a basis of the specific choice of model and parameterizations used for the adhesion (docking) state. We use the standard decomposition of the powder-averaged kinematic structure factor $S(q)$ and vesicle (or bilayer) form factor $F(q) = |f(q)|^2$ with the form factor amplitude $f(q)$ to write the scattering intensity $I(q) \propto \langle F(\vec{q})S(\vec{q})\rangle$, where $\langle ...\rangle$ denotes the powder average. q is given by the modulus of the momentum transfer vector $q = |\vec{q}| = (4\pi/\lambda)\sin\theta$, where λ is the wavelength of the the X-rays and θ the half of the scattering angle relative to the incident beam (cf. Fig. 2.1). The EDP normal to the bilayer, which enters into the form factor F, is parameterized by three Gaussian functions according to

$$\rho(\vec{r}) = \sum_{i=1}^{3} \rho_i \exp\left[-\frac{(z-z_i)^2}{2\sigma_i^2}\right], \tag{2.1}$$

representing both headgroup regions and the hydrophobic chain region with the amplitude ρ_i, the peak position z_i and the width σ_i of the respective Gaussian function as sketched in Fig. 2.1(b). This model has the advantage that it provides analytic solutions for F.

The flat bilayer and the spherical vesicle model. For non-interacting vesicles, we assume $S = 1$. We consider two basic models to compute F on the basis of [99], namely the flat bilayer model, which assumes that the SAXS signal is dominated by the powder-averaged bilayer structure, and spherical vesicle model, which takes interference of the bilayer with the overall spherical shape properly into account. Note that the latter has the advantage of providing the mean vesicle radius R_0 and polydispersity σ_R, in

addition to the bilayer structure parameters.

With the assumption that interference between different bilayer patches averages out in polydisperse ensembles, the vesicle suspension can be considered as a 'perfect powder' of flat lipid bilayer patches with random orientations. The form factor amplitude is hence given by the one-dimensional Fourier transform of the electron density $\rho(z)$ (Eq. 2.1)

$$f_{\mathrm{fb}}(q) = \int \rho(z)\exp(\mathrm{i}qz)\mathrm{d}z \,, \tag{2.2}$$

followed by powder averaging. The scattering intensity is then simply given by $\langle |f_{\mathrm{fb}}(q)|^2 \rangle$ since interactions between vesicles are neglected [99]

$$I_{\mathrm{fb}}(q) \propto \frac{1}{q^2} \sum_{i=1}^{N} \sum_{j=1}^{N} \rho_i \rho_j \sigma_i \sigma_j \exp\left[-\frac{q^2(\sigma_i^2 + \sigma_j^2)}{2} \right] \cos[q(z_i - z_j)] \,, \tag{2.3}$$

where the factor q^{-2} takes into account the powder average of the one-dimensional Fourier transform in Eq. 2.2.

Taking the spherical symmetry of the vesicles into account, the form factor amplitude is given by the radially symmetric Fourier transform of the electron density $\rho(z)$

$$f_{\mathrm{sv}}(q) = \int \rho(r) r^2 \frac{\sin(qr)}{qr} \mathrm{d}r \,. \tag{2.4}$$

The scattering intensity is then calculated by taking the polydispersity of the vesicle suspension into account using a Gaussian distribution. As shown by [99], it can be written as

$$I_{\mathrm{sv}}(q) \propto \frac{1}{q^2} \sum_{i=1}^{N} \sum_{j=1}^{N} \rho_i \rho_j \sigma_i \sigma_j \exp\left[-\frac{q^2(\sigma_i^2 + \sigma_j^2)}{2} \right] [A_{ij}(q) - B_{ij}(q) + C_{ij}(q)] \,, \tag{2.5}$$

where $A_{ij}(q)$, $B_{ij}(q)$ and $C_{ij}(q)$ contain the structural parameters R_0 (mean radius) and σ_R (standard deviation of the size distribution) as follows:

$$A_{ij}(q) = [(R_0 + z_i)(R_0 + z_j) + \sigma_R^2] \cos[q(z_i - z_j)] \,, \tag{2.6}$$

$$B_{ij}(q) = \exp(-2q^2\sigma_R^2)[(R_0 + z_i)(R_0 + z_j) + \sigma_R^2 - 4q^2\sigma_R^4] \cos[q(2R_0 + z_i + z_j)] \tag{2.7}$$

and

$$C_{ij}(q) = 2q\sigma_R^2 \exp(-2q^2\sigma_R^2)(2R_0 + z_i + z_j) \sin[q(2R_0 + z_i + z_j)] \,. \tag{2.8}$$

The docking model. According to the flat bilayer model, the form factor amplitude of the electron density of a single bilayer is calculated by the Fourier transform in Eq. 2.2, yielding [98]

$$f_{\mathrm{fb}}(q) = \sqrt{2\pi}\left[\underbrace{2\sigma_{\mathrm{h}}\rho_{\mathrm{h}}\exp\left(-\frac{\sigma_{\mathrm{h}}^2 q^2}{2}\right)\cos(qz_{\mathrm{h}})}_{\text{Bilayer headgroups}} + \underbrace{\sigma_{\mathrm{c}}\rho_{\mathrm{c}}\exp\left(-\frac{\sigma_{\mathrm{c}}^2 q^2}{2}\right)}_{\text{Bilayer chain region}}\right]. \tag{2.9}$$

Here, the left term in the square brackets corresponds to the form factor of the bilayer headgroups and the right term to the form factor of the chain region.

In real space two bilayers in close apposition can be described by a convolution of the electron density $\rho(z)$ with the sum of two Dirac delta functions with distance d given by

$$s(z) = \delta(z) + \delta(z-d)\,. \tag{2.10}$$

The Fourier transform of the delta function is simply a shift in Fourier space, thus

$$s(q) = 1 + \exp(-iqd)\,. \tag{2.11}$$

The modulus square of Eq. 2.11 gives the structure factor

$$S(q) = 2 + 2\cos(qd)\,. \tag{2.12}$$

Note that the structure factor in Eq. 2.12 can also be obtained from a multi-lamellar vesicle model with N bilayers with periodicity d [98, 130], setting $N = 2$. Using Eq. 2.9 and Eq. 2.12 the scattering intensity $I(q)$ is given by

$$I_{\mathrm{d}}(q) \propto \frac{1}{q^2}\left[\nu_{\mathrm{d}}|f_{\mathrm{fb}}(q)|^2 S(q) + (1-\nu_{\mathrm{d}})|f_{\mathrm{fb}}(q)|^2\right]\,, \tag{2.13}$$

taking into account the superposition of the scattering contribution of single (undocked) bilayers $(1-\nu_{\mathrm{d}})|f_{\mathrm{fb}}(q)|^2$, and of docked bilayers, respectively. Note that even if all vesicles dock, $\nu_{\mathrm{d}} < 1$, corresponding to the fraction of vesicle surface involved in adhesion. Again, the factor q^{-2} takes the powder average into account.

Form and structure factor simulations. Fig. 2.2 shows simulated SAXS curves $I(q)$ vs. q of the form and structure factor models discussed above in order to illustrate the characteristic features related to the structural parameters.

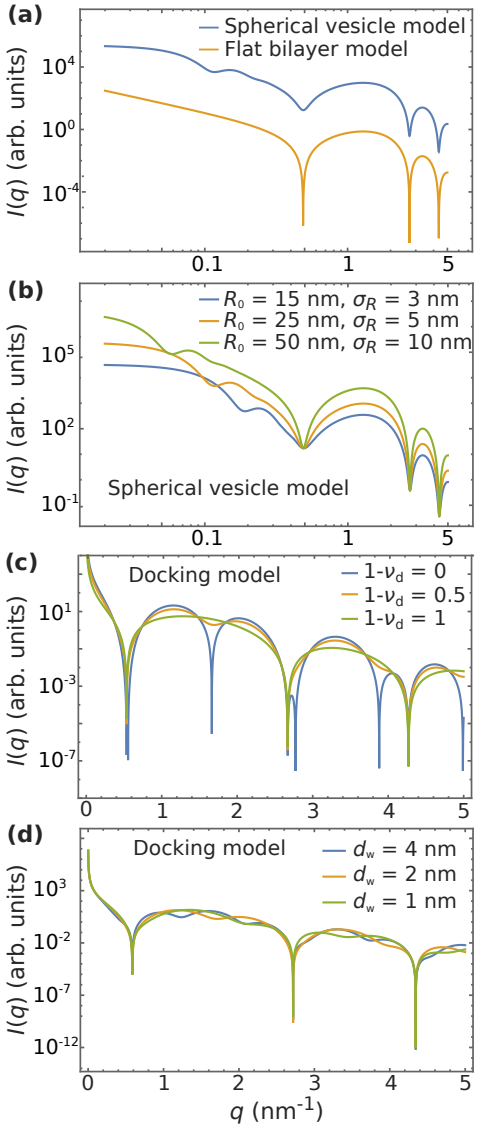

Fig. 2.2: Form and structure factor models. (a) Comparison of the spherical vesicle model (blue line) and the flat bilayer model (orange line). (b) Spherical vesicle model for varied radius and polydispersity (R_0/σ_R = constant). (c) Docking model for d_w = 2 nm and different values of $(1-\nu_d)$. (d) Docking model for different water spacings d_w, 4 nm (blue line), 2 nm (orange line) and 1 nm (green line), for $\nu_d = 0.5$. The bilayer parameters are $\sigma_h = 0.35$ nm, $\sigma_c = 0.7$ nm, $\rho_h = 1.5$ (arb. units), $\rho_c = -1$ (arb. units) and $d_{hh} = 3.6$ nm for (a) and (b) and $\sigma_h = 0.4$ nm, $\sigma_c = 0.7$ nm, $\rho_h = 1.5$ (arb. units), $\rho_c = -1$ (arb. units) and $d_{hh} = 3.66$ nm for (c) and (d).

In (a) we compare the flat bilayer model and the spherical vesicle model. Differences are observed in particular in the low q-region, where modulations are evident in the case of the spherical model. Accordingly, this q-region is sensitive to the mean radius R_0 and to the width of the size distribution σ_R of the vesicles. Contrarily, at higher q-values, the flat bilayer model represents a good approximation and can be used to obtain structural parameters only of the bilayer in a robust manner. In (b) we compare spherical model curves for different radii, while the ratio of the radius to the polydispersity is kept constant. As expected, the minima (modulations) are shifted towards lower q-values when R_0/σ_R increases. Furthermore, we observe an increase of the scattering intensity over the entire q-range. In (c) we compare scattering curves for different values of $(1-\nu_d)$. $(1-\nu_d) = 0$ gives the limiting case for the scattering arising only from adhering bilayers (blue line), thus $I_d(q) \propto (1/q^2)F(q)S(q)$. In addition to the form factor minima of a single bilayer, further modulations are observed due to the structure factor. In the limiting case $(1-\nu_d) = 1$ (green line), the docking model equals the flat bilayer model $I_d(q) \propto (1/q^2)F(q)$. The third example shown is $(1-\nu_d) = 0.5$ (orange line), corresponding to a superposition of the scattering from two bilayers in close apposition and from single uncorrelated bilayers. In this scenario, which corresponds to the experimental observations, the structure factor modulations can be observed but are less pronounced than the form factor minima. In (d) scattering curves for different water spacings d_w are compared. While the form factor minima remain, the intermediate modulations of the structure factor vary in a characteristic manner with d_w. As expected, the minima of the structure factor modulations are shifted towards lower q-values when d_w increases.

Least-squares fit. To obtain structural parameters from SAXS data, the experimental scattering intensities $I_{exp}(q_i)$ with data points $i = 1, ..., N$ recorded at q_i, were fitted by the model curve $I_{mod}(q_i)$, accounting for scaling factor and background as

$$I_{tot}(q) = c_1 \cdot I_{mod}(q) + I_{bg}(q)\,. \tag{2.14}$$

The quality of the fit was monitored by the reduced χ^2-function

$$\chi^2_{red} = \frac{\sum_{i=1}^{N} \frac{[I_{exp}(q_i) - I_{tot}(q_i)]^2}{\sigma_i^2}}{N - p - 1}\,, \tag{2.15}$$

where p is the number of free model parameters and σ_i^2 is the variance of the intensity

$I_{\mathrm{exp}}(q_i)$ for a measured data point i. Nonlinear least-squares fitting was implemented using the MATLAB function *lsqnonlin* of the MATLAB R2016a Optimization Toolbox. For the flat bilayer model and the docking model, a constant background $I_{\mathrm{bg}}(q) = c_2$ was used to account for possible errors in the instrumental background subtraction. For the spherical vesicle model both constant and power-law background correction terms $I_{\mathrm{bg}}(q) = c_2 q^{-c_3} + c_4$ were used, as indicated. For the bilayer structure, a symmetric profile was enforced, reducing the number of free parameters, unless specified otherwise. The Gaussian parameters representing the headgroups are $\sigma_{\mathrm{h}} = \sigma_{\mathrm{h1}} = \sigma_{\mathrm{h2}}$ and $\rho_{\mathrm{h}} = \rho_{\mathrm{h1}} = \rho_{\mathrm{h2}}$. While the width σ_{c} of the Gaussian representing the chain region is a free parameter, the amplitude and the position were fixed to $\rho_{\mathrm{c}} = -1$ (arb. units) and $z_{\mathrm{c}} = 0$ (nm), respectively. The positions of the two outer Gaussians are denoted $z_{\mathrm{h1,2}} = \pm z_{\mathrm{h}}$. Only for the comparison in Fig. 2.3 an asymmetric bilayer model was included. Hence, the width and the amplitude of the Gaussians representing the headgroups were free parameters for both sides ($\sigma_{\mathrm{h1}} \neq \sigma_{\mathrm{h2}}$ and $\rho_{\mathrm{h1}} \neq \rho_{\mathrm{h2}}$), while the positions were fixed analogously to the symmetric profile.

2.3 Results and Discussion

2.3.1 SAXS characterisation of unilamellar vesicles

First, we have verified that a unilamellar state has been reached by the vesicle preparation for each of the different lipid compositions, in order to have a structural reference for any further docking or fusion reactions. In view of a fusion reaction, we further addressed the question if we can control the size distribution of the vesicles. To this end, SAXS measurements were performed after the respective preparation step (subsequent extrusion through membranes of 100 nm, 50 nm and 30 nm pore size) in ultra-pure (Milli-Q) water, and are shown as Supporting Material (Fig. A.2). The SAXS curves indicate that vesicles containing the negatively charged lipid DOPS achieve unilamellarity already after the first preparation step of direct sonication, while DOPC:DOPE mixtures (pure DOPC and the molar ratios of 4:1 and 1:1) differ from the characteristic SAXS profile of unilamellar vesicles in particular between the first two form factor minima, where remnants of Bragg peaks or at least modulations are observed. For both DOPC and DOPC:DOPE (4:1) unilamellarity is not even achieved after three runs of extrusion (using pore diameters of 100, 50 and 30 nm), while DOPC:DOPE (1:1) does become unilamellar after the final extrusion step (30 nm diameter). Hence, if no

charged lipid component is used, at least a high molar ratio of DOPE should be used to achieve unilamellar vesicles. A strong decrease in scattering intensity is observed for DOPC and DOPC:DOPE after extrusion, reflecting the significant reduction in lipid concentration after filtering out big aggregates.

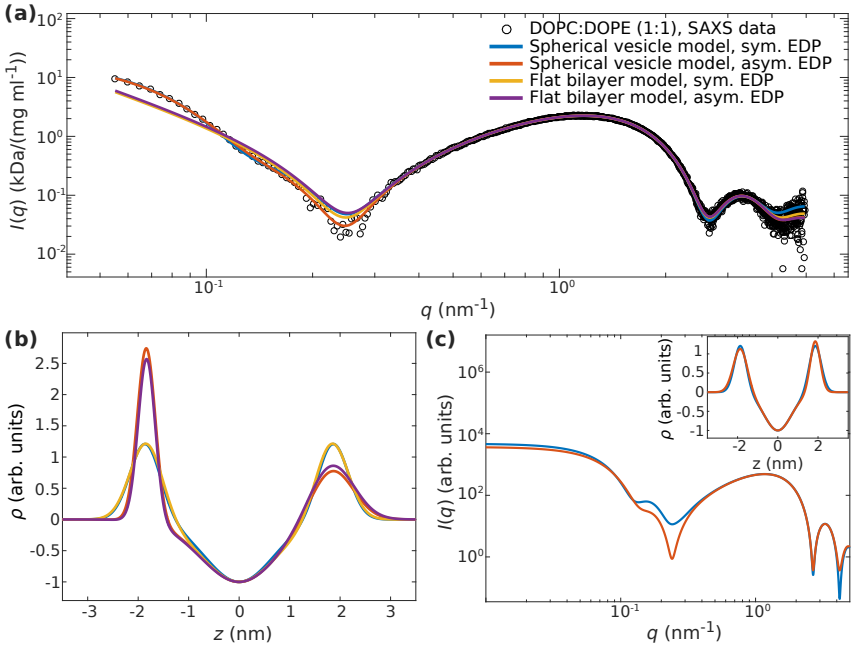

Fig. 2.3: (a) SAXS data of 30nm extruded DOPC:DOPE (1:1) vesicles in Milli-Q water (black circles), spherical vesicle model fits with either a symmetric or an asymmetric EDP (blue and red lines, respectively), flat bilayer model fits with either a symmetric or an asymmetric EDP (yellow and purple lines, respectively). (b) EDPs obtained from the fits in (a) with the corresponding colours. (c) SAXS simulation results using the spherical vesicle model with either a symmetric or an asymmetric EDP (blue and red, respectively).

Next, we have to select a suitable scattering model for unilamellar vesicles, to extract structural parameters of the bilayer EDP. To this end we compare the models of the flat bilayer dispersion and of perfectly spherical vesicles. We further investigate the effects of constraining the model to asymmetric EDP versus a freely parameterized EDP.

Fig. 2.3 shows a quantitative analysis of the SAXS data of 30 nm extruded DOPC:DOPE (1:1) vesicles, where different models are compared. In (a), the spherical vesicle model and the flat bilayer model fits are shown, both for symmetric and asymmetric EDP. For the spherical vesicle model fit, the full q-range was fitted, while only a restricted q-range of $\sim 0.36 - 4.95$ nm^{-1} was fitted to the flat bilayer model, corresponding to

the validity of this model (cf. SAXS simulations, Fig. 2.2). Note that all fit functions are plotted over the entire q-range for a better comparability. Further, an additional power law $c_2 q^{-c_3} + c_4$ modeling the background is included in the spherical vesicle model, and a constant background in the flat bilayer model. The dependence of the structural parameters on the choice of the background model is further elucidated in the Supporting Material (Fig. A.3).

The corresponding EDPs are plotted in (b). The structural parameters and the related χ^2_{red} are listed in Tab. 2.1. In general, all models match the data quite well, with only minor differences in the medium and high q-range. The parameters of the bilayer profile are found to be robust with respect to the two models and background choices. Larger differences between the models are observed in the lower q-range. As expected, only the spherical vesicle model can capture the dip corresponding to the vesicle size (radius R_0). The values for R_0 derived from the fit match the expectation according to the pore size of the extrusion, see Tab. 2.1.

Slight improvements of χ^2_{red} appear for an asymmetric bilayer profile. However, this is hard to justify in view of the unreasonably strong asymmetry (b) as well as the high number of free model parameters. In (c) SAXS simulations of the spherical vesicle model with either a symmetric or an asymmetric bilayer profile are indicated. The EDP is displayed in the inset. By comparison of the two cases, we observe that already a slightly asymmetric profile yields large deviations in the SAXS profile (red lines), in particular for the form factor minima. This observation indicates that a precise background subtraction is essential when considering an asymmetric bilayer structure since especially the form factor minima are sensitive to this. Therefore, we restrict ourselves mainly to the analysis of a symmetric bilayer profile to obtain robust effective EDPs.

Note that the analysis of further curves is presented as the Supporting Material (Fig. A.4), along with tabulated values of structural parameters (Tab. A.1, A.2, A.3), obtained from the fits for the respective models.

2.3.2 Adhesion of lipid vesicles

Next, we have investigated the structural changes induced by the addition of divalent salts. Fig. 2.4(a-c) shows a series of SAXS data $I(q)$ vs. q of vesicles, either suspended in ultra-pure water (a,b) or in a 100 mM glucose solution (c), where structural changes were induced as a function of lipid composition and $CaCl_2$/$MgCl_2$. In the case of pure DOPS (a), we observe a phase transition towards a multi-lamellar phase already at low

Tab. 2.1: Structural parameters obtained from spherical vesicle model and flat bilayer model least-squares fits to SAXS data of 30 nm extruded DOPC:DOPE (1:1)-vesicles, using either a symmetric or an asymmetric bilayer profile. The structural bilayer parameters are $\rho_h = \rho_{h1} = \rho_{h2}$ and $\sigma_h = \sigma_{h1} = \sigma_{h2}$, or $\rho_{h1} \neq \rho_{h2}$ and $\sigma_{h1} \neq \sigma_{h2}$ for a symmetric or an asymmetric bilayer profile, respectively. The amplitude of the Gaussian representing the chain region is selected to $\rho_c = -1$ (arb. units) for all fits.

Model	Bilayer structure	ρ_{h1}, ρ_{h2} (a. u.)	σ_{h1}, σ_{h2} (nm)	σ_c (nm)	d_{hh} (nm)	R_0 (nm)	σ_R (nm)	χ^2_{red}
Flat bilayer	Symmetric	1.26, 1.26	0.32, 0.32	0.73	3.68	-	-	1.15
	Asymmetric	2.63, 0.92	0.17, 0.44	0.77	3.66	-	-	1.1
Spherical vesicle	Symmetric	1.23, 1.23	0.30, 0.30	0.67	3.72	14.35	7.4	1.42
	Asymmetric	2.79, 0.82	0.18, 0.42	0.75	3.68	15.32	8.68	1.09

$CaCl_2$ concentrations, e.g. 0.1 mM, as is evidenced by the emerging Bragg peaks. The latter become more pronounced with an increase of the $CaCl_2$ concentration. From the position of the first Bragg peak we infer a lamellar periodicity $d = 2\pi/q_0 \approx 4.97$ nm, for the 1 mM $CaCl_2$ curve, yielding a water layer thickness $d_w = d - d_{hh} = 1.18$ nm, given the measured headgroup-to-headgroup distance $d_{hh} = 3.79$ nm (Supporting Material, Tab. A.1).

Contrary to DOPS, the SAXS profiles of the two-component mixture DOPC:DOPS (1:1) (b,c) exhibit a different lineshape with structure factor modulations instead of Bragg peaks upon addition of $CaCl_2$ or $MgCl_2$ (highlighted by black arrows). According to the simulations of the docking model in Fig. 2.2, we identify these profiles as stable adhesion states of the vesicles. Control experiments indicate that the observed structure factor modulations are characteristic for the divalent cations Ca^{2+} and Mg^{2+}. The addition of (b) 4 mM glucose or (c) 4 mM KCl does not lead to this particular lineshape. At the same time, changes in the low q-range of the SAXS profile are observed for vesicles suspended in ultra-pure water, both for the control experiment as well as upon the addition of $CaCl_2$, indicating structural changes of the vesicle shape, e.g. due to osmotic shrinkage or locally flattened bilayers. Contrarily, no pronounced changes in the low q-range are observed for vesicles suspended in a 100 mM glucose solution, indicating that the overall vesicle shape (apart from the contact zone) remains

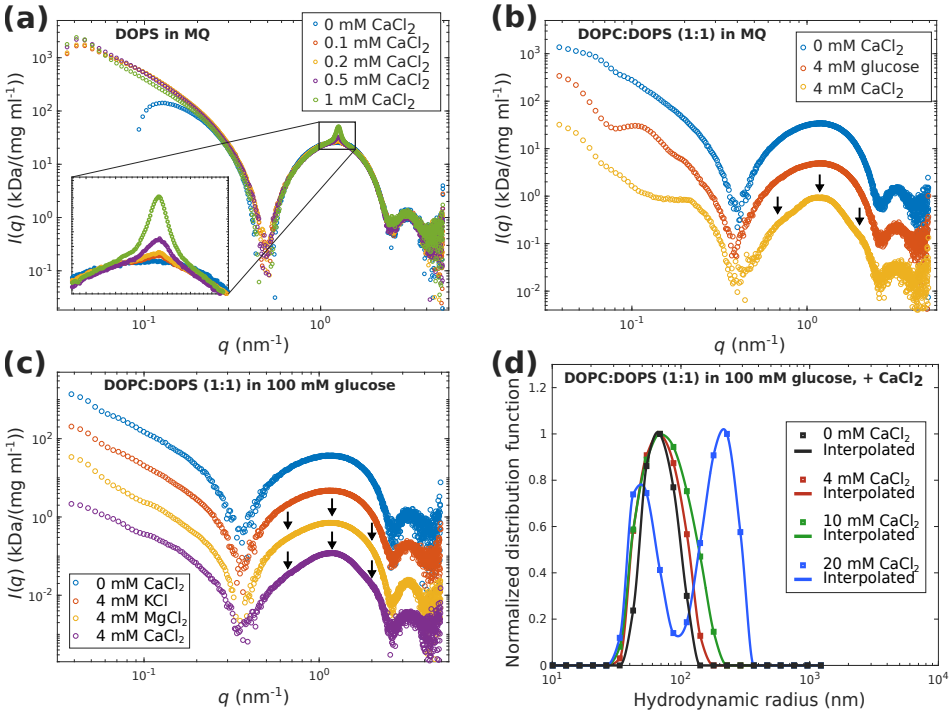

Fig. 2.4: (a) SAXS data $I(q)$ vs. q of DOPS vesicles in ultra-pure water, measured after the addition of $CaCl_2$ at different concentrations. (b) SAXS data $I(q)$ vs. q of DOPC:DOPS (1:1) vesicles in ultra-pure water (blue), after addition of 4 mM glucose (red) and after addition of 4 mM $CaCl_2$ (yellow). The SAXS profiles are shifted for clarity. (c) SAXS data $I(q)$ vs. q of DOPC:DOPS (1:1) vesicles in a 100 mM glucose solution (blue), after addition of 4 mM KCl (red), after addition of 4 mM $MgCl_2$ (yellow), and after addition of 4 mM $CaCl_2$ (purple). The SAXS profiles are shifted for clarity. (d) Size distributions of DOPC:DOPS (1:1) vesicles in 100 mM glucose, measured by DLS after the addition of $CaCl_2$ at different concentrations.

spherical in this case. To shed further light on the overall size of the adhering vesicles, DLS measurements were performed, before and after addition of $CaCl_2$. Fig. 2.4(d) shows the resulting size distributions for DOPC:DOPS (1:1) vesicles in 100 mM glucose. Upon addition of 4 mM and 10 mM $CaCl_2$, the size distributions are systematically broadened, particularly, towards higher hydrodynamic radii. In this range, the size distributions are still monodisperse, indicating that strong aggregation of many vesicles does not play a role. For 20 mM $CaCl_2$, however, the size distribution becomes bimodal and shifts to significantly higher hydrodynamic radii.

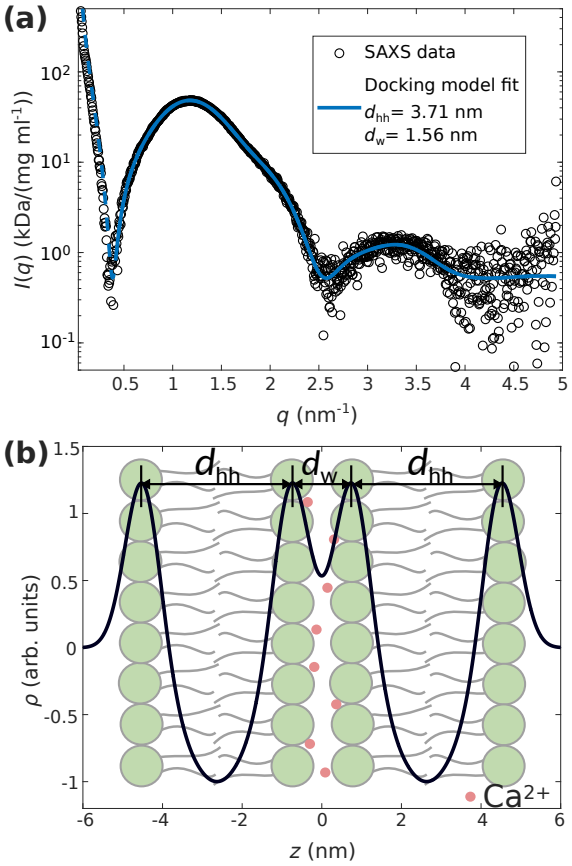

Fig. 2.5: (a) SAXS data $I(q)$ vs. q of DOPC:DOPS (1:1) vesicles suspended in a 100 mM glucose solution upon addition of 4 mM $CaCl_2$ (black circles) and least-squares fit using the docking model (blue line). (b) Reconstructed EDP using the structural parameters obtained from the docking model fit indicated in (a). The structural parameters are summarized in Tab. 2.2.

The quantification of structural parameters by least-squares fitting is exemplified in

Fig. 2.5 for $CaCl_2$-induced adhesion of DOPC:DOPS (1:1) vesicles in 100 mM glucose. To this end, the docking model has been applied with a constant background model. As is apparent from (a), the docking model is well suited to describe the SAXS data in the fitted q-range, here ~ 0.424 to 4.95 nm^{-1}, where the scattering is dominated by the bilayer form factor. In (b), the corresponding EDP of the two bilayers in close proximity is displayed, with an interbilayer spacing of $d_w = 1.56$ nm. In Tab. 2.2 the structural parameters of all fits are listed. Lipid composition, aqueous environment (ultra-pure water versus 100 mM glucose solution) and the $CaCl_2$/$MgCl_2$-concentration have been varied. From the results, we draw the following conclusions: (1) the bilayer structure and the interbilayer distance d_w are nearly identical for the glucose solution and ultra-pure water, (2) d_w does not change between 4 mM and 10 mM $CaCl_2$ and $MgCl_2$, (3) d_w for $MgCl_2$ is slightly higher, by ~ 1.5 Å, than for $CaCl_2$, (4) In ultra-pure water the vesicles deform more easily than in glucose, favoring a higher fraction of adhered membranes ν_d, (5) d_w depends on the lipid composition (i.e. charge density) as it is significantly smaller (~ 1 nm) for DOPC:DOPS (4:1) than for (1:1), and (6) the bilayer thickness increases upon addition of $CaCl_2$ and $MgCl_2$. Note that further EDPs are included as Supporting Material (Fig. A.5), illustrating the differences between $CaCl_2$- and $MgCl_2$-induced structural changes, as well as the effect of background (monovalent) salt (KCl), see Supporting Material, Fig. A.6, Tab. A.4. In this case higher interbilayer distances (~ 3 to 6 nm) are observed.

2.3.3 Interaction potentials

Next, we have investigated which additive interaction potentials and parameters could possibly explain the observed values of $d_w \sim 1.6$ nm of the adhesion state. To this end, Fig. 2.6 shows different approaches for modeling the interaction free energy per unit area, corresponding to different experimental scenarios.

We start by the 'reference state' of uncharged (zwitterionic) phospholipids such as pure DOPC, governed by a repulsive hydration interaction f_{hyd} and an attractive van der Waals term f_{vdW} [52, 131, 56]. The resulting equilibrium water layer thickness is known from experiments on fully hydrated multilamellar membranes as $d_w \simeq 2.7$ nm [132]. Note that the value corresponds to the definition as the distance between the two headgroup maxima. This value is reproduced by modeling the interactions, i.e. by an exponential hydration repulsion term [52]

$$f_{hyd}(d_w) = P_h \lambda_h \exp\left(-\frac{d_w}{\lambda_h}\right), \tag{2.16}$$

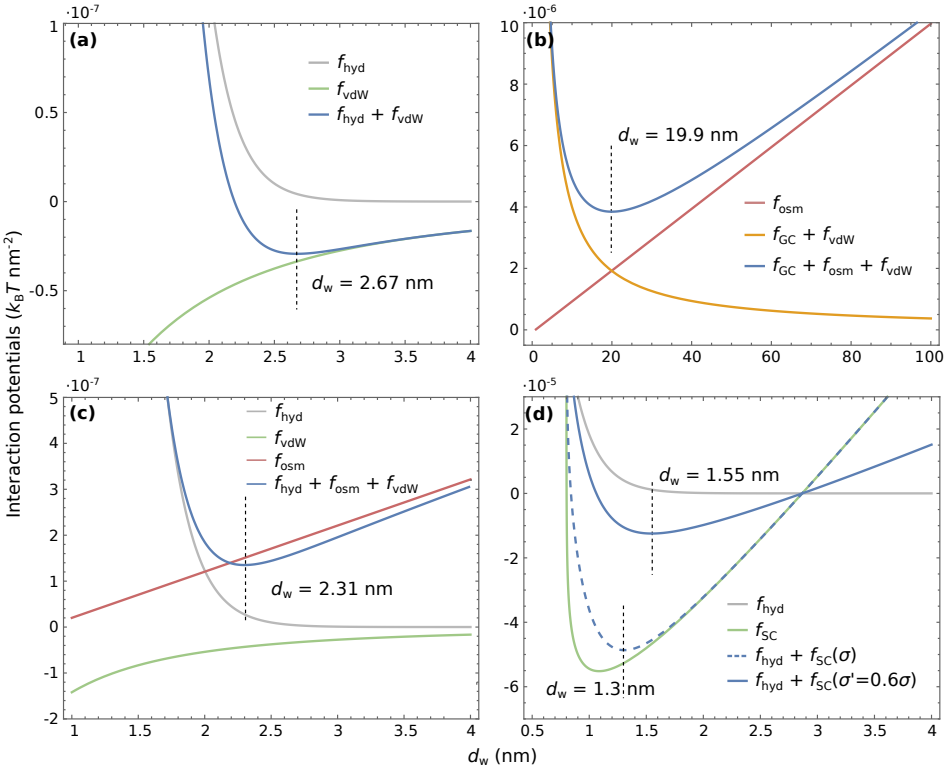

Fig. 2.6: Calculated interaction potentials per unit area as a function of the interbilayer distance, modeled to discern possible scenarios to reproduce the experimental equilibrium water layer $d_w \simeq 1.6$ nm in the adhesion state. (a) The total interaction potential for uncharged membranes exhibits a local minimum at $d_w \approx 2.7$ nm, for the experimental parameters given below. (b) The adhesion vanishes if Poisson-Boltzmann repulsion in the Gouy-Chapman regime is taken into account, and can be rescued only by an additional (attractive) osmotic pressure, plotted here for an assumed maximum of 10 mM expelled ions causing the attractive osmotic pressure (or depletion force). (c) The same depletion force acting on the neutral membrane would only slightly change the adhesion state to $d_w \approx 2.3$ nm. (d) The strong-coupling potential (green line) yields an attractive interaction of like-charge membranes at small separations. By adding the hydration repulsion, an equilibrium water spacing of $d_w \approx 1.3$ nm is found, already close to the experimental finding. The latter is well reproduced for $\sigma' = 0.6\sigma$ (solid blue line). The following simulation parameters have been used: $\sigma = 0.5/64 \cdot 10^{20}\ e/\mathrm{m}^2$ assuming an area per lipid headgroup of 64 Å^2, $\lambda_D \simeq 2.36 \cdot 10^{-9}$ m, $l_B \simeq 7.11 \cdot 10^{-10}$ m, $l_{GC} \simeq 2.87 \cdot 10^{-10}$ m in (b), $l_{GC} \simeq 1.43 \cdot 10^{-10}$ m in (d), $d_a = 20 \cdot 10^{-10}$ m, $d_h = 16 \cdot 10^{-10}$ m, $H_{stat} = 0.7$, $H_{disp} = 0.7$, $\lambda_h = 2 \cdot 10^{-10}$ m, $P_h = 3.3 \cdot 10^9$ Jm^{-3}, $T = 294$ K.

Tab. 2.2: Structural parameters as obtained from the flat bilayer and docking model analyses of the SAXS data of DOPC:DOPS (1:1) vesicles in MQ and in 100 mM glucose with respect to the added $CaCl_2$ and $MgCl_2$ concentration. The model fits are based on a symmetric EDP, thus the amplitude and width of the inner and outer leaflet are $\rho_h = \rho_{h1} = \rho_{h2}$ and $\sigma_h = \sigma_{h1} = \sigma_{h2}$. The amplitude of the Gaussian representing the chain region is selected to $\rho_c = -1$ (arb. units) for all fits.

Sample	Fit model	$[CaCl_2]$ (mM)	$[MgCl_2]$ (mM)	ρ_h (a. u.)	σ_h, σ_c (nm)	d_{hh} (nm)	d_w (nm)	$(1-\nu_d)$	χ^2_{red}
DOPC:DOPS (4:1) in MQ	Flat bilayer	-	-	1.47	0.42, 0.89	3.75	-	-	1.20
	Docking	4	-	1.66	0.43, 0.86	3.95	1.00	0.73	7.13
DOPC:DOPS (1:1) in MQ	Flat bilayer	-	-	1.35	0.42, 0.89	3.64	-	-	1.19
	Docking	4	-	1.42	0.44, 0.95	3.72	1.54	0.85	1.37
DOPC:DOPS (1:1) in 100 mM glucose	Flat bilayer	-	-	1.27	0.42, 0.90	3.63	-	-	1.03
	Docking	4	-	1.39	0.44, 0.95	3.71	1.56	0.89	1.14
	Docking	10	-	1.26	0.51, 0.98	3.70	1.60	0.82	0.95
	Docking	-	4	1.34	0.39, 0.84	3.72	1.72	0.98	0.89
	Docking	-	10	1.32	0.46, 0.98	3.69	1.74	0.86	1.11

where the prefactor $(P_h\lambda_h)$ is typically on the order of a few k_BT Å^{-2} with the Boltzmann constant $k_B \simeq 1.38065 \cdot 10^{-23}$ J/K and the temperature T, and the decay length λ_h is in the range of 1 to 3 Å. Following [59, 56], we write the van der Waals interaction as the sum of the static and the dispersive part $f_{vdW}(d_w) = f_{stat}(d_w) + f_{disp}(d_w)$ with

$$f_{vdW}(d_w) = -\frac{H_{stat}k_BT}{12\pi(d+d_h/2)^2} - \frac{H_{disp}k_BT}{16\pi(d+d_h)^2}\left[1 - \frac{2}{(1+d_a/(d+d_h))^2} + \frac{1}{(1+2d_a/(d+d_h/2))^2}\right], \tag{2.17}$$

where d_h and d_a denote the hydrophilic and hydrophobic slab thickness, i.e. the headgroup and hydrocarbon chains, respectively. The Hamaker constants H_stat and H_disp are of order one. The resulting potential is plotted in Fig. 2.6(a) for the exact parameter values given in the caption. When anionic lipids such as DOPS are present as in the experimental two-component lipid mixture, the corresponding average surface charge density σ results in an unbinding of charged membranes, i.e. the van-der-Waals attraction cannot compensate the repulsion in the Poisson-Boltzmann regime [133]. How does this change if salt is added and electrostatic repulsion is screened?

For monovalent ions and concentrations in the experimentally relevant mM range, the repulsion is in the Gouy-Chapman regime. This follows from evaluation of the three characteristic length scales, the Bjerrum length $l_\mathrm{B} = e^2(4\pi\epsilon\epsilon_0 k_\mathrm{B}T)^{-1}$, the Debye screening length $\lambda_\mathrm{D} = ((\epsilon_0\epsilon_r k_B T)(\sum_i n_{0,i} e^2 q_i^2)^{-1})^{1/2}$, and the Gouy-Chapman length $l_\mathrm{GC} = (2\pi q l_\mathrm{B}\sigma)^{-1}$ according to [75, 76], for the parameters given in the caption. Here, e is the the elementary charge, q is the valency of the ions, n_0 is the number density of the ions, $\epsilon_0 = 8.85 \cdot 10^{-12}$ F/m is the vacuum permittivity, $\epsilon_r \simeq 80$ is the dielectric constant for water, and σ is the surface charge density in the units of e/m^3. In this regime, the free energy per unit area is given by [75, 76]

$$f_\mathrm{GC}(d_\mathrm{w}) = \frac{\pi k_\mathrm{B}T}{2 l_\mathrm{B} d_\mathrm{w}}, \tag{2.18}$$

which is plotted in Fig. 2.6(b) including an additional van der Waals term (orange line). Again, no minimum and thus no adhesion state is formed. Only if we introduce an additional osmotic pressure (red line), a minimum can again form (blue line), albeit at much larger distances for the relevant osmotic pressure corresponding to an excess concentration of ions in the mM range. Such an osmotic pressure or depletion force could arise if ions are expelled from the inter-membrane space, similar to the phenomenon reported in [134]. Accordingly, we would have an additional attractive interaction

$$f_\mathrm{osm}(d_\mathrm{w}) = cRTd_\mathrm{w}, \tag{2.19}$$

where c is the excess concentration of the expelled ions or molecules in the units of $\mathrm{mol\,m^{-3}}$ and $R \approx 8.314\,\mathrm{kg\,m^2\,s^{-2}\,mol^{-1}\,K^{-1}}$ is the gas constant. Here we can assume a maximum value of 10 mM for the expelled ions. Such an osmotic pressure would hence result in a rather large d_w in the range of several nm, rescuing a weak adhesion state in charged membranes. Contrarily, it would have only a minor effect on d_w in the uncharged reference system (pure DOPC), as visualized in Fig. 2.6(c), in comparison

to (a). Accordingly, neither osmotic effects nor mean-field electrostatics [75, 76], which neglects ion-ion correlation effects and is also denoted as the weak coupling regime, can explain the experimental results. Contrarily, the so-called strong coupling theory [71, 74, 135, 72], which is characterized by ion bridging and/or ion correlation effects is well known to result in attractive interaction of like-charge membranes. The two regimes are delineated by the unitless coupling parameter $\Xi = \tilde{l}_\mathrm{B}/l_\mathrm{GC}$, where $\tilde{l}_\mathrm{B} = q^2 l_\mathrm{B}$. The Poisson-Boltzmann approximation is valid for $\Xi \ll 1$, while $\Xi \gg 1$ is denoted as the strong coupling regime. For the present experimental parameters, we indeed find $\Xi \simeq 19.8$. Correspondingly, we must turn to the the strong coupling regime, for which an analytical expression was derived in [71, 72] in terms of the interaction pressure

$$P_\mathrm{SC}(d_\mathrm{w}) = 2\pi l_\mathrm{B}\sigma^2 k_\mathrm{B}T\left(-1 + \frac{2l_\mathrm{GC}}{d_\mathrm{w}}\right). \tag{2.20}$$

By integration, we find the potential plotted in (d) (green line) for the given experimental parameters. The addition of the hydration repulsion to the strong coupling potential (dashed blue line) predicts an adhesion state with $d_\mathrm{w} \simeq 1.3$ nm, which is already quite close to the experimental finding. Further, a reduction of the charge density to $\sigma' = 0.6\sigma$ (solid blue line) or equivalently an increase of the decay length λ_h of the hydration repulsion from 0.2 nm to 0.25 nm (not shown), would result in perfect agreement. We find that the van der Waals force can be safely neglected here, since the attractive force is in this case largely dominated by like-charge attraction, as given by the expression above.

We conclude that the observed adhesion state with $d_\mathrm{w} \simeq 1.6$ nm is well explained by a superposition of hydration repulsion and electrostatics in the strong coupling regime predicted by the theory of R. R. Netz, A. G. Moreira and coworkers.

2.3.4 Outlook: SNARE-liposomes

After probing the adhesion state in pure lipid vesicles, the next challenge is to perform similar experiments using proteo-liposomes, where complex formation of SNAREs and Ca^{2+} condensation both control adhesion and subsequently fusion. While we could not yet reach this goal in this work, we pave the way by a careful structural characterization of the preparation pathway of SNARE-liposomes as displayed in Fig. 2.7(a,b) to get a better understanding of the structure of SNARE-liposomes. (a) shows SAXS data of DOPC:DOPE:DOPS:Chol (5:2:2:1) liposomes in a 150 mM KCl, 20 mM HEPES, pH 7.4 buffer (blue circles) and of DOPC:DOPE:DOPS:Chol (5:2:2:1) liposomes

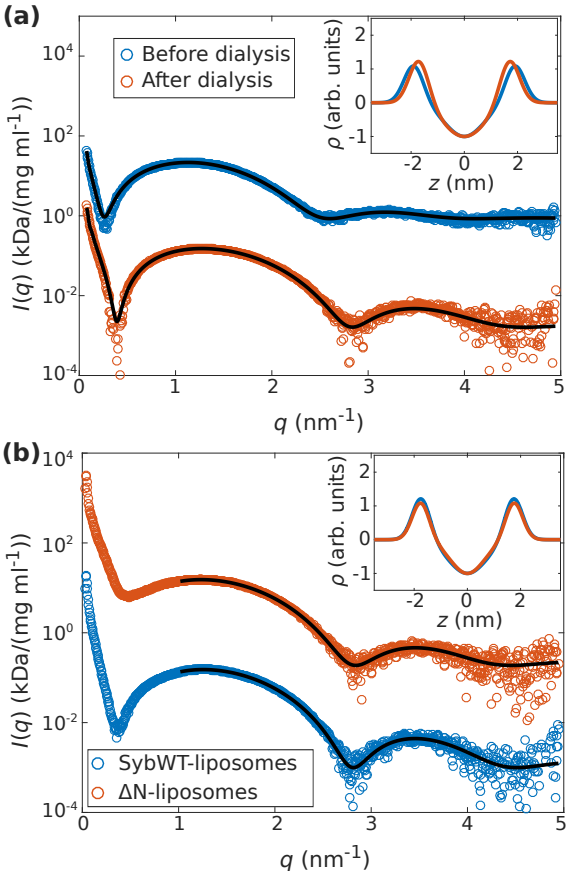

Fig. 2.7: Structural characterization of SNARE-liposomes. (a) SAXS data of DOPC:DOPE:DOPS:Chol (5:2:2:1) liposomes (shifted for clarity) directly after extrusion (blue circles) and after an overnight dialysis, mixed with n-OG ($R = 2$, red circles). Least-squares fits (black lines) are based on the spherical vesicle model, the resulting EDPs are indicated in the inset (colors correspond to the SAXS data). (b) SAXS data of SNARE-liposomes, SybWT-liposomes (blue circles) and ΔN-complex liposomes (red circles), shifted for clarity. Least-squares fits (black lines) are based on the flat bilayer model and the resulting EDPs are indicated in the inset (colors correspond to the SAXS data).

after an overnight-dialysis, where the liposomes were mixed with n-OG (red circles). For the latter case, the R-value was set to $R = 2$ (analogous to the preparation of ΔN-liposomes). The least-squares analysis is based on the spherical vesicle model with an additional power-law background model. Structural parameters of the fits are listed in Tab. 2.3. The obtained EDPs are indicated in the inset. We address the question whether an overnight-dialysis involving n-OG affects the bilayer structure. In fact, the analysis of both scattering curves reveals significant changes in the bilayer structure as the headgroup-to-headgroup distance d_{hh} decreases by ~ 4 Å after the dialysis step. Moreover, the mean radius of the liposome suspension is decreased after dialysis. Fig. 2.7(b) shows SAXS data from ΔN- (red circles) and SybWT-liposomes (blue circles). Compared to the SAXS curves of pure lipid vesicles, the curves differ in particular in the lower q-range. The first minima are less pronounced for SNARE-liposomes, in particular for ΔN-liposomes, most likely due to the interference between the SNAREs and the lipid-bilayer as well as due to the form factor of the SNAREs themselves. Least-squares analysis is carried out based on the flat bilayer model with an additional constant background assuming a symmetric bilayer structure. The corresponding EDPs are shown in the inset, and the structural parameters are listed in Tab. 2.3. By comparison of the structural parameters, we observe only slight differences between Syb- and ΔN-liposomes, and between the SNARE-liposomes and the control liposomes (after dialysis). This indicates that the SNAREs have only a minor effect on the mean lipid bilayer structure. For example, for all SNARE-liposomes a slight increase of d_{hh}, up to ~ 1 Å, was obtained. Hence, rather than a result of SNARE reconstitution, the thinning must be attributed to the preparation protocol. It could be either explained by a loss of Chol [136] washed out by n-OG, or by a remaining fraction of n-OG even after dialysis. Note that n-OG is known to form bilayers together with phospholipids [137]. Further evidence for the second explanation is found in [90].

2.4 Summary and Conclusions

First, we have screened the preparation pathway and parameters as well as different fitting models in view of structural docking and fusion assays. Suitable suspensions of small unilamellar vesicles were obtained for all but pure DOPC vesicles, which showed interbilayer interactions even after several extrusion steps. In all cases, it was challenging to achieve vesicle preparations with sufficiently small polydispersity σ_R to clearly observe R_0 and σ_R. From the spherical vesicle model fits, we have obtained plausible

Tab. 2.3: Structural parameters of syb- and ΔN-liposomes and of protein-free liposomes with the same lipid-composition DOPC:DOPE:DOPS:Chol (5:2:2:1) with respect to the fit model. For all fits a symmetric bilayer profile was applied, so that $\rho_h = \rho_{h1} = \rho_{h2}$ and $\sigma_h = \sigma_{h1} = \sigma_{h2}$. The amplitude of the Gaussian representing the chain region $\rho_c = -1$ (arb. units) for all fits.

	Fit model	ρ_h (a.u.)	σ_h, σ_c (nm)	d_{hh} (nm)	R (nm)	σ_R (nm)	χ^2_{red}
DOPC:DOPE:DOPS:Chol (5:2:2:1) in buffer	spherical vesicle	1.12	0.36, 0.72	3.81	47.8	17	1.39
	flat bilayer	1.11	0.36, 0.70	3.83	-	-	0.82
DOPC:DOPE:DOPS:Chol (5:2:2:1) in buffer (after dialysis)	spherical vesicle	1.36	0.32, 0.72	3.45	34.7	18.1	1.20
	flat bilayer	1.35	0.34, 0.78	3.41	-	-	0.67
SybWT-liposomes in buffer	flat bilayer	1.26	0.33, 0.71	3.47	-	-	0.68
SybΔ84-liposomes in buffer	flat bilayer	1.24	0.34, 0.71	3.51	-	-	0.68
ΔN-liposomes in buffer	flat bilayer	1.10	0.32, 0.64	3.51	-	-	0.72
DOPC:DOPE:DOPS:Chol (5:2:2:1) in ultra-pure water	spherical vesicle	1.09	0.46, 0.84	3.55	29.4	13.7	2.47

values, for example $R_0 \simeq 14$ nm and $\sigma_R = 7.4$ nm for 30 nm-extruded DOPC:DOPE (1:1) vesicles, but it must be realized that a high polydispersity in combination with an insufficient fusion efficiency probably do not allow us to clearly observe the increase in R_0 following vesicle fusion. The spherical vesicle model is found to be too restrictive since it does not account for any deviations from the perfect sphere, for example by thermal fluctuations. Contrarily, the quasi-planar bilayer model was used in a very robust and convincing manner, if the low q-range is excluded. However, access to R_0 is of course lost in this case. In future, there are several possible remedies: 1.) The vesicle population could be purified, or the scattering volume could be reduced, e.g. by using microfluidics in combination with focused undulator radiation. 2.) the spherical model can be generalized to account for deviations from the perfect spherical shape with appropriate parameters for shape and size polydispersity. 3.) the absolute scattering intensity in combination with calibrated vesicle concentration can be exploited to

obtain constraints on R_0. Further, molecular dynamics simulation (MD) studies could be used to obtain constraints in the analysis of the SAXS data. It would for example be an interesting task to focus on asymmetric bilayer profiles resulting from curvature [138, 139].

As the main result of this work, we found very clear evidence for a calcium-induced adhesion state in lipid vesicles, initially suspended in ultra-pure water or in a 100 mM glucose solution, and could quantify the corresponding density profiles of the contact zone. The control experiments in glucose solution prove that the double bilayer contact detected by the SAXS pattern does not arise from deflated vesicles but indeed from the adhesion between two different vesicles. Further, the characteristic water layer thickness in this strong adhesion regime was nearly identical for ultra-pure water $d_w \approx 1.5 - 1.7$ nm and for the glucose solution, and also was nearly identical at 4 and 10 mM concentration of bulk $CaCl_2$. This suggests a recruitment of Ca^{+2} to the contact zone in a quantity required to compensate the charge density of anionic membranes. The monovalent counterions must hence be expelled from the contact zone. The resulting osmotic pressure is not the cause of the adhesion but rather its outcome, but may further act to stabilize the adhesion. Given the fact that d_w is defined here as the distance between density maxima of the headgroups, and the headgroup width is $d_h \simeq 0.8$ nm, an ion bridging phenomenon is structurally plausible, eventually accompanied by a local bilayer corrugation. The observed interbilayer distance can also be compared to the critical distance where the stalk phase appears (0.9 ± 0.05 nm), an intermediate prior to fusion [34].

Using realistic parameters, simple mean field models of electrostatics do not result in interbilayer potentials which yield the observed interbilayer distances. Only when we evaluate the interaction forces of the so-called strong coupling theory according to R. R. NETZ, A. G. MOREIRA and coworkers, we can reproduce the experimental result for realistic parameters. Accordingly, ion condensation on the bilayer surface and ion correlations are responsible for the observed adhesion. This phenomenon which is interesting in itself from a soft-matter and electrostatics point of view, certainly deserves further attention, and should be complemented by investigations of solid-supported lipid bilayers in solution in the presence of $CaCl_2$ (e.g. [140, 141, 142]), as well as by MD simulations in the future. Here, we observed nearly the same effect for Mg^{+2} as for Ca^{+2}, with a small but systematic shift of $\Delta d_w \simeq 0.15$ nm. This would be in line with recent reports that Ca^{2+} and Mg^{2+} dehydrate and partially neutralizes the bilayer surface with a stronger effect for Ca^{2+} due to a higher binding affinity [123], which could possibly also play a role in the physiological scenario of calcium-

dependent membrane fusion. Finally, we observed a stable $CaCl_2$-induced adhesion state at reduced concentration of monovalent salt, but in a soft regime characterized by much higher interbilayer distances, not compatible with ion bridging. Depending on lipid composition and ion concentrations, this equilibrium distance could be varied over a wide range ($\sim$ 3 to 6 nm), see Supporting Material (Fig. A.6, Tab. A.4).

In future, protein-induced docking should become tractable by the scattering model put forward here, once that a higher efficiency and purity of the SNARE induced adhesion state can be reached. As a first step towards this goal, we have structurally characterized vesicles with reconstituted SNAREs in this work. Specifically, our future aim will be to identify and to characterize a SNARE-induced docking state, based on a suitable mutant (SybΔ84), which promotes full fusion but prevents docking. However, we did not find clear evidence for this state, yet, possibly due to limited efficiency and loss of the signal by averaging over different populations, see Supporting Material (Fig. A.7). Nevertheless, even without docking and fusion, the structural characterization of vesicles with reconstituted SNAREs was successful and is an important first step. Generally, the SAXS data of the SNARE-liposomes showed more features in the scattering curves $I(q)$ vs. q (hence, also potentially more information) than we could analyze in this work with limited models. With appropriate extensions of the form factor models it should become possible to obtain information on the SNAREs in the lipid bilayers. Given a lipid-to-protein ratio of 500:1 we estimate a copy number of $\sim$70 SNAREs per vesicle with a radius of 30 nm. With a 'full q-range' model, including a coarse-grained description of the SNAREs, the distribution of SNAREs and possible clustering could be addressed, along with the mean radius and the polydispersity of the SNARE-liposomes. Such a model could be then useful to study the structure before and after fusion, as well as the arrested docking intermediate. Towards this goal, a first point of reference is the work of S. CASTORPH et al. [107], where anisotropic form factor models were derived for the analysis of SAXS data of synaptic vesicles, including the structure of both the lipid bilayer and the protein layers inside and outside of the vesicles.

Acknowledgments

The SAXS experiments were performed on beamline BM29 at the European Synchrotron Radiation Facility (ESRF), Grenoble, France. We acknowledge Dr. Diego Pontoni, Dr. Yuri Gerelli and Pierre Lloria for sharing their resources and expertise at

ESRF and at the Partnership for Soft Condensed Matter (PSCM) facilities during our beamtimes. We also thank Susanne Hengst for her support in sample preparation and Dr. Sebastian Aeffner for fruitful discussions.

This work was supported financially by Sonderforschungsbereich 803 "Functionality Controlled by Organization in and between Membranes" funded by Deutsche Forschungsgemeinschaft.

Vesicle adhesion in the electrostatic strong-coupling regime studied by time-resolved small-angle X-ray scattering

3

Karlo Komorowski, Jannis Schaeper, Michael Sztucki, Lewis Sharpnack, Gerrit Brehm, Sarah Köster, and Tim Salditt
Reproduced from Soft Matter **16**, 4142-4154 (2020)

We have used time-resolved small-angle X-ray scattering (SAXS) to study the adhesion of lipid vesicles in the electrostatic strong-coupling regime induced by divalent ions. The bilayer structure and the interbilayer distance d_w between adhered vesicles was studied for different DOPC:DOPS mixtures varying the surface charge density of the membrane, as well as for different divalent ions, such as Ca^{2+}, Sr^{2+}, and Zn^{2+}. The results are in good agreement with the strong coupling theory predicting the adhesion state and the corresponding like-charge attraction based on ion-correlations. Using SAXS combined with the stopped-flow rapid mixing technique, we find that in highly charged bilayers the adhesion state is only of transient nature, and that the adhering vesicles subsequently transform to a phase of multilamellar vesicles, again with an interbilayer distance according to the theory of strong binding. Aside from the stopped-flow SAXS instrumentations used primarily for these results, we also evaluate microfluidic sample environments for vesicle SAXS in view of future extension of this work.

3.1 Introduction

The intrinsically non-equilibrium state of small unilamellar lipid vesicles (SUVs) is stabilized against the transition to larger membrane aggregates such as multilamellar

lipid vesicles (MLVs) by repulsive interactions, in particular by hydration repulsion as well as by electrostatic repulsion for the case of charged lipids [31, 75, 76]. Furthermore, while fusion of two SUVs would release curvature energy on the order of the bending rigidity κ, the highly curved intermediate states in membrane fusion also act as a highly effective energetic barrier. For these reasons, lipid vesicles can be encountered as metastable phases, or - in a biological context - as organelles, which can maintain their structure and shape also without significant energy turnover. In fact, the conditions of stability against aggregation, shape transformation and fusion are of utmost importance, equally for cellular vesicles and lipid vesicles used in drug delivery, food processing or cosmetics.

At some point in its life, triggered by changes in environmental parameters or by strong interactions, a vesicle it is bound to transform. Structural observation and characterization of these shape transformations is of fundamental interest, but challenging in view of their transient nature and the small length scales involved, on the order of the bilayer thickness. In the biological context, membrane fusion is known as a well-controlled and important physiological process. Fusion of neurotransmitter-filled synaptic vesicles (SVs) with the presynaptic plasma membrane [4], for example, is an essential step in nerve conduction. This process is catalyzed and controlled by proteins, in particular by the soluble *N*-ethylmaleimide-sensitive factor attachment protein receptors (SNAREs) [17]. In general, the merger of two membranes involves a highly complex interplay on the molecular level among lipids, proteins, ions of the aqueous environment and water molecules. Important aspects of the membrane fusion pathway, concerning for example intermediate structures, such as the docking state [23, 94], and the quantitative evaluation of underlying forces and energetics, are currently under investigation. To this end, numerical studies have provided interesting insight into possible structures and mechanisms [119, 37], and now call for experimental verification.

Lipid vesicles without proteins have also been intensively studied. The equilibrium phase diagram of vesicle shapes was calculated long ago [143], and a quantitative understanding of inter-bilayer forces based on linear superposition of molecular interactions has entered textbooks [31, 58]. Self-consistent field-theoretical approaches including Helfrich-type steric interaction predict a phase transition from bound to unbound lipid membranes [144]. More recently, effects from non-linear electrostatics, such as like-charge attraction, have been considered, and a regime of strong coupling induced by multi-valent ions has been identified [71, 74, 135, 72]. Binding of divalent ions, in particular Ca^{2+} and Mg^{2+} to lipid membranes has been studied by Molecular

Dynamics (MD) simulations [122, 123, 124].

We have recently studied the adhesion state of vesicles, as induced by the divalent ions Ca^{2+} and Mg^{2+} for different ion concentration, lipid composition, and surface charge density σ_s [145]. Using small-angle X-ray scattering (SAXS), we could distinguish a strong adhesion state - probably caused by ion bridging - and a soft adhesion state in the presence of background monovalent salt concentration. While vesicle adhesion was observed when mixing anionic and zwitterionic or neutral lipids (binary and quaternary lipid mixtures), pure anionic membranes (DOPS) with correspondingly high σ_s were found to undergo a phase transition to a multilamellar state. The structure and interactions between charged MLVs in the presence of multivalent ions was also studied by SAXS in [146]. Recently, strong coupling has been studied between two highly charged solid-supported lipid bilayers in the presence of monovalent counter-ions by neutron and X-ray reflectivity [147]. While interesting aspects of bilayer interactions beyond linear electrostatics were elucidated, studies of ion-induced transition, non-equilibrium effects or the kinetics of vesicle phase transitions still remain scarce, with the exception of experiments based on temperature changes (T-jump) [148].

In this work, we now extend our SAXS studies of the adhesion state, presenting a wider range of ions and first time-resolved studies monitoring the transition from SUVs to MLVs Fig. 3.1(a,b). We show that the divalent salts induced attractive interactions between bilayers, which are in quantitative agreement with the strong coupling theory put forward by R. Netz and coworkers [71, 74, 135, 72]. Furthermore, we have studied the adhesion transition by time-resolved SAXS using the rapid mixing technique as illustrated in Fig. 3.1(a) as well as with microfluidic devices. Importantly, we can identify a transient docking intermediate state in the SUV to MLV transition in DOPC:DOPS mixtures, induced by Ca^{2+}.

For this study, we have used both a stopped-flow rapid mixer as well as microfluidic devices, and different beam conditions, instrumentation and optics have been evaluated for studies of time-resolved SAXS, in particular with respect to docking and fusion of vesicles. Therefore, it is adequate to briefly consider the state-of-the art in this field: SAXS combined with the stopped-flow rapid-mixing technique has been used previously to study osmotic shrinkage of sterically stabilized liposomes [149], as well as the role of calcium in membrane condensation and spontaneous curvature variations in model lipidic systems [150]. A calcium triggered lamellar to hexagonal phase transition ($L_\alpha - H_2$) was studied by combined rapid mixing and time-resolved synchrotron SAXS [151]. For SAXS in combinations with microfluidics, we refer to the

review [111]. Direct monitoring of calcium-triggered phase transitions in cubosomes using small-angle X-ray scattering combined with microfluidics has been reported in [152]. A microfluidic platform for the continuous production and characterization of multilamellar vesicles was presented in [153]. Finally, a microfluidic SAXS Study of unilamellar and multilamellar surfactant vesicle phases was reported in [154].

3.2 Interaction potentials and strong coupling regime

Before giving the details of the experiment, we briefly address the essential interactions needed to describe the docking of vesicles and the transition from SUVs to multilamellar phases. Like-charge attraction between two bilayers induced by divalent ions is illustrated in Fig. 3.1(c). The distance between the two bilayers is denoted as d_w, which is obtained from the SAXS analysis described in detail in the Materials and Methods section. In the following, we recapitulate the formula used in the literature for the sake of notational clarity. In line with textbook literature and in particular following the review by Andelman [75], we first define the characteristic length scales which govern the different regimes of electrostatic interaction between membranes in solution. The Bjerrum length is defined as

$$l_B = e^2(4\pi\epsilon\epsilon_0 k_B T)^{-1} , \tag{3.1}$$

where $e \simeq 1.602 \cdot 10^{-19}$ C is the elementary charge, $\epsilon_0 = 8.85 \cdot 10^{-12}$ F/m is the vacuum permittivity, ϵ is the relative permittivity of a medium (≈ 80 for water at room temperature), $k_B \simeq 1.381 \cdot 10^{-23}$ J/K is the Boltzmann constant, and T is the temperature in the units of K. The Bjerrum length gives the length scale at which the electrostic energy between two unit charges equals the thermal energy. The Gouy-Chapman length is expressed as

$$\mu = (2\pi q l_B \sigma_s)^{-1} , \tag{3.2}$$

where σ_s is the surface charge density of the membrane, and q the valency of the ions. At the Gouy-Chapman length scale, the electrostic energy between a unit charge and a planar surface with a constant charge density σ_s equals the thermal energy. Finally,

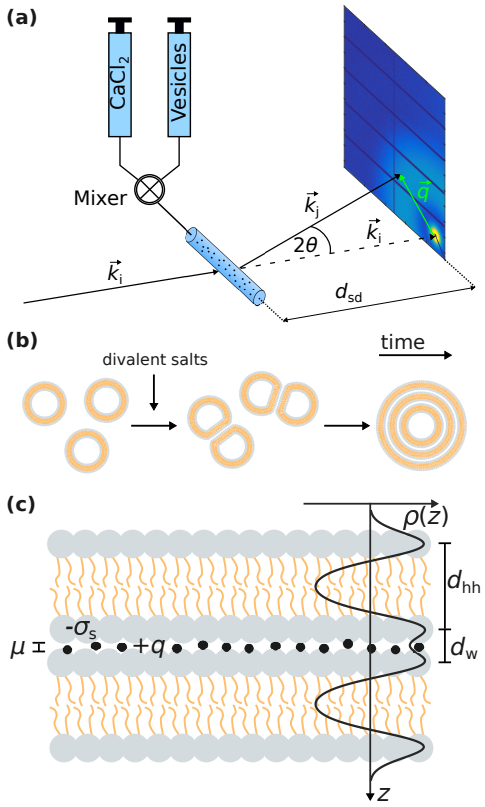

Fig. 3.1: (a) Illustration of the principle of SAXS combined with the stopped flow rapid mixing technique. The two components ($CaCl_2$ and unilamellar lipid vesicles both prepared in ultra-pure water) are rapidly mixed and flowing into a flow-through capillary cell adapted to the mixing chamber. For time-resolved data collection, the X-ray beam is synchronized with the mixing device. The two-dimensional diffraction pattern is measured by an area detector. The distance between the sample plane and the detector is denoted by d_{sd}. The momentum transfer vector is given by $\vec{q} = \vec{k}_j - \vec{k}_i$, where $\vec{k}_i$ and $\vec{k}_j$ are the wave vectors of the incident and the scattered X-ray beam, respectively. (b) Sketch of the structural dynamics of the phase transition from unilamellar vesicles toward multilamellar vesicles upon mixing with divalent salts. An intermediate state of docked vesicles can be distinguished in the structural analysis of the SAXS data. (c) Illustration of the strong coupling theory on lipid membranes. Two like-charge membranes with the surface charge density $-\sigma_s$ are in close proximity induced by ion correlations, where the ions have the valency $+q$. In the SAXS analysis the effective electron density profile (EDP) $\rho(z)$ is modeled by the sum of three Gaussians (one Gaussian for each headgroup region and one Gaussian for the hydrophobic chain region). The bilayer thickness d_{hh} is given by the distance between the two headgroup's maxima within the bilayer. The inter-membrane distance d_w is defined as the distance between two opposing headgroup maxima. The Gouy-Chapman length μ is a measure for the ion-layer thickness. Note, that σ_s and q are both positive by definition.

the Debye screening length is

$$\lambda_{\mathrm{D}} = \left(\frac{\epsilon_0 \epsilon_r k_B T}{\sum_i n_{0,i} e^2 q_i^2} \right)^{1/2} , \tag{3.3}$$

where $n_{0,i}$ is the number density of ions species i. The Debye length describes a characteristic length for which the electrostatic interactions between two charges in the presence of all other ions of the solution are screened.

Together, these three length scales are sufficient to describe all regimes of linear electrostatics in solution. As mentioned above, the dominant attraction between like-charge membranes when adhesion is induced by divalent ions is described by the so-called strong coupling theory [71, 74, 135, 72], which is characterized by ion bridging and/or ion correlation effects. In contrast, mean-field electrostatics which neglect ion-ion correlation effects is denoted as the weak coupling regime [75, 76]. The two regimes are delineated by the unitless coupling parameter $\Xi = \tilde{l}_{\mathrm{B}}/\mu$, where $\tilde{l}_{\mathrm{B}} = q^2 l_{\mathrm{B}}$. The Poisson-Boltzmann approximation is valid for $\Xi \ll 1$, while $\Xi \gg 1$ is denoted as the strong coupling regime. In the strong coupling regime, an analytical expression for the interaction pressure is given as

$$P_{\mathrm{sc}}(d_{\mathrm{w}}) = 2\pi l_{\mathrm{B}} \sigma_{\mathrm{s}}^2 k_{\mathrm{B}} T \left(-1 + \frac{2\mu}{d_{\mathrm{w}}} \right) . \tag{3.4}$$

To describe the balance of forces and the equilibrium distance between bilayers in the docking state (see Fig. 3.2 below), the electrostatic attraction of the strong coupling regime is superimposed to the repulsive hydration potential, which we write as [31]

$$f_{\mathrm{hyd}}(d_{\mathrm{w}}) = P_{\mathrm{h}} \lambda_{\mathrm{h}} \exp\left(-\frac{d_{\mathrm{w}}}{\lambda_{\mathrm{h}}} \right) , \tag{3.5}$$

where the prefactor $(P_{\mathrm{h}}\lambda_{\mathrm{h}})$ is typically on the order of a few $k_{\mathrm{B}}T$ Å^{-2}, and the decay length λ_{h} is in the range of 1 to 3 Å. The superposition of the strong coupling potential as found by integration of the interaction pressure given above and of the hydration potential is plotted in Fig. 3.2(d) for the given parameters.

3.3 Materials and Methods

3.3.1 Microfluidics devices

X-ray compatible microfluidics devices were built in a multi-step process following the protocol in [155]. First, SU-8 2150 negative photo resist (MicroChem, Newton, MA, USA) is processed by means of standard photolithography on a 2-inch silicon wafer. During the soft bake step, an edge bead removal is performed to ensure a better contact between the substrate and the photo mask (Selba S. A., Versoix, Switzerland) in the mask aligner. The resulting channels have a width of 200 μm as defined by the lithography mask, and a height of 200 μm as measured with a profilometer (Veeco Dektak 6). Subsequently, a PDMS copy (Sylgard, Dow Corning, Midland, USA) was made from the wafer. The PDMS stamp was used to print the structure in UV-curable glue (NOA 81, Norland Optical Adhesives, Cranberry, USA) on a glass slide as support which is cured under a UV-lamp (366 nm). A stack of aluminium foil, the glass slide and a 300 μm COC foil (Topas 8007, Topas Advanced Polymers GmbH, Frankfurt, Germany) with a glass transition temperature $t_G = 78\,^{\circ}\mathrm{C}$ was placed in a preheated laboratory hotpress at 130 °C for 10 min. Subsequently, it was pressed with 2.3 kN for 5 min. Holes for the inlets and outlets are punched in the COC with a 0.5 mm biopsy punch (Harris Unicore, Sigma-Aldrich, St. Louis, Missouri, USA). The device is sealed with a 20 μm COC foil (Topas 8007, Topas Advanced Polymers GmbH, Frankfurt, Germany) with a glass transition temperature $t_G = 78\,^{\circ}\mathrm{C}$ in a heat and pressure controlled lamination machine.

In order to tightly connect the microfluidics device and the tubing in a leak-free manner, the device was integrated into a sample holder. The sample holder consists of two plates made of aluminium, which are designed with a gab to expose the channels. The two plates sandwich a PVC (polyvinylchloride) plate and the device itself. The front metal plate and the PVC plate have five small holes matching the holes of the device to attache the tubing to the device. For sealing, the tubing was further threaded through o-rings. A photograph of the sample holder integrated at the GINIX endstation at the P10 beamline is shown in Fig. 3.5.

To establish certain flow velocities on all four inlets and to be able to control the flow remotely the neMESYS pump system (Cetoni GmbH, Korbussen, Germany) is used in combination with Hamilton Gastight Syringes (Hamilton Bonaduz AG, Switzerland).

3.3.2 Simulation of the microfluidic flow

Both the flow conditions and the distribution of lipid vesicles and Ca^{2+}-ions in the microfluidics device have been studied using finite element method (FEM) simulations with COMSOL Multiphysics 5.3 (COMSOL GmbH, Göttingen, Germany). Due to the small cross-section of the device and the small flow rates, the flow can be described as laminar flow, hence the stationary Navier-Stokes equation was solved, applying the no-slip boundary condition at the channel walls. The distribution of lipid vesicles and the Ca^{2+}-ions in the channel was calculated, setting the initial concentration of both substances to the arbitrary value 1 mol/m^3. The diffusion coefficient of the lipid vesicles has been calculated according to the Stokes-Einstein equation, $D_{\text{vesicle}} = k_B T/(6\pi\eta r)$, with vesicle radius $r_{\text{vesicle}} = 20\,\text{nm}$. The diffusion of Ca^{2+}-ions was modelled with a diffusion constant $D_{Ca^{2+}} = 7.92 \times 10^{-10}\,\text{m}^2/\text{s}$ [156].

3.3.3 Sample preparation

Lipid vesicles with a size of approximately 100 nm in diameter were prepared by extrusion through polycarbonate membranes. The lipids dioleoylphosphatidylcholine (DOPC) and dioleoylphosphatidylserine (DOPS) were purchased as lyophilized powders from Avanti Polar Lipids (Alabaster, AL, USA). DOPC and DOPS were dissolved in chloroform and mixed at the desired molar ratio. Subsequent evaporation of chloroform was performed under a stream of nitrogen. The resulting dried lipid film was hydrated either with a 100 mM glucose solution or ultra-pure water to a final lipid concentration of 10 mg/ml for the flow-through SAXS and the microfluidic SAXS experiments, and to 20 mg/ml for the stopped-flow SAXS experiments. Note that by adding glucose the vesicle volume can be quenched, as water in- or outflux is penalized by an osmotic pressure difference. For vesicle preparation, the suspension was first vortexed and subsequently extruded (35 times) through membranes with pore sizes of 100 nm in diameter by using a Mini-Extruder from Avanti Polar Lipids (Alabaster, AL, USA). Prior to the injection into both, the microfluidic and the stopped-flow rapid mixing devices, the samples were gently degassed to minimize air bubbles.

3.3.4 Small-angle X-ray scattering

SAXS experiments were performed at the undulator beamlines P10 at Deutsches Elektronen-Synchrotron (DESY) in Hamburg, Germany, and ID02 [157] at European

Synchrotron Radiation Facility (ESRF) in Grenoble, France. At P10, the GINIX (Göttingen instrument for nanoscale imaging with X-rays) endstation [158] was used for the experimental realization. The details of the experimental settings are given below.

3.3.4.1 Microfluidic SAXS

At P10, the beamline was operated at $E = 13.8$ keV photon energy monochromized by a Si(111) double crystal monochromator with an X-ray beam of size 2.5 μm (horizontal) $\times$ 1.3 μm (vertical) focused by a beryllium compound refractive lens (CRL) transfocator. The scattered X-rays were recorded using an Eiger 4M detector (Dectris, Switzerland) with 2070 $\times$ 2167 pixels, each of size 75 μm $\times$ 75 μm, at a sample-to-detector distance of 5.098 m.

At ID02, the photon energy was set to 12.56 keV by a Si(111) mono crystal monochromator. The beam size at the sample plane was 30 μm $\times$ 30 μm for microfluidics experiments. The scattered X-rays were recorded using an Rayonix MX-170HS CCD pixel detector (Rayonix L.L.C., USA) with 3840 $\times$ 3840 pixels at a sample-to-detector distance of 1.5 m.

3.3.4.2 Flow-through and stopped-flow SAXS

SAXS experiments using the flow-through capillary cell (1.6 mm in diameter), as well as the stopped-flow rapid mixing device (SFM-400, Bio-Logic Instruments, France) were performed at the beamline ID02 of the ESRF. For the stopped-flow SAXS experiments, the flow-through capillary cell was adapted to the mixing chamber. More details of the stopped-flow rapid mixing device implemented in the ID02 beamline can be found in [159, 160]. The measurements were performed during two different beamtimes. The beamline was operated at 12.56 keV photon energy for the data sets shown in Fig. 3.3(a,c), and at 12.45 keV photon energy for the data sets shown in Fig. 3.2 and Fig. 3.3(b). The sample-to-detector distance was 1.5 m to cover a q-range of approximately 0.067 to 5.124 nm^{-1}. The beam-size at the sample-plane was 100 μm $\times$ 100 μm.

3.3.4.3 SAXS analysis

In general, the analysis of SAXS data from lipid vesicles is well covered in literature, e.g. reviewed in [100]. In this work we follow the SAXS analysis described in [145], where we have shown, that the effective structural parameters of the lipid bilayer and

the water spacing between two bilayers in close proximity can be well obtained from the flat bilayer model [99, 145] and the docking model [145]. These models are based on the assumption, that the vesicles can be considered as a perfect powder of flat lipid bilayer patches with random orientations, without taking the spherical shape of the vesicles into account.

Briefly, we use the standard decomposition of the powder-averaged kinematic structure factor $S(q)$ and the bilayer form factor $F(q) = |f(q)|^2$ with the form factor amplitude $f(q)$ to write the scattering intensity $I(q) \propto \langle F(\vec{q})S(\vec{q})\rangle$, where $\langle ...\rangle$ denotes the orientational average. q is given by the modulus of the momentum transfer vector $q = |\vec{q}| = (4\pi/\lambda)\sin\theta$, where λ is the wavelength of the the X-rays and θ the half of the scattering angle relative to the incident beam. The electron density profile (EDP) $\rho(z)$ normal to the bilayer, which enters into the form factor by $F(q) = |f(q)|^2 = |\int \rho(z)\exp(iqz)dz|^2$, is parameterized by three Gaussian functions according to

$$\rho(\vec{r}) = \sum_{i=1}^{3} \rho_i \exp\left[-\frac{(z-z_i)^2}{2\sigma_i^2}\right], \tag{3.6}$$

representing both headgroup regions and the hydrophobic chain region with the amplitude ρ_i, the peak position z_i and the width σ_i of the respective Gaussian function (Fig. 3.1(c)).

The final expression for the scattering intensity of the docking model used in the analysis is given by [145]

$$I_{\mathrm{d}}(q) \propto \frac{1}{q^2}\left[\nu|f_{\mathrm{fb}}(q)|^2 S(q) + (1-\nu)|f_{\mathrm{fb}}(q)|^2\right], \tag{3.7}$$

where

$$S(q) = 2 + 2\cos(qd), \tag{3.8}$$

with the distance d, and

$$f_{\mathrm{fb}}(q) = \sqrt{2\pi}\left[\underbrace{2\sigma_{\mathrm{h}}\rho_{\mathrm{h}}\exp\left(-\frac{\sigma_{\mathrm{h}}^2 q^2}{2}\right)\cos(qz_{\mathrm{h}})}_{\text{Bilayer headgroups}} + \underbrace{\sigma_{\mathrm{c}}\rho_{\mathrm{c}}\exp\left(-\frac{\sigma_{\mathrm{c}}^2 q^2}{2}\right)}_{\text{Bilayer chain region}}\right], \tag{3.9}$$

taking into account the superposition of the scattering contribution of single (undocked) bilayers $(1-\nu)|f_{\mathrm{fb}}(q)|^2$, and of docked bilayers $\nu|f_{\mathrm{fb}}(q)|^2 S(q)$, respectively.

Therefore, the dimensionless parameter ν is a measure for the fraction of adhered bilayers in the ensemble of docked and undocked vesicles. For $\nu = 0$, Eq. 3.7 corresponds to the flat bilayer model. Note that even if all vesicles dock, $\nu < 1$, corresponding to the fraction of vesicle surface involved in adhesion. The factor q^{-2} takes the orientational average into account. The bilayer thickness and the interbilayer spacing are defined as $d_{\mathrm{hh}} = 2|z_{\mathrm{h}}|$ and $d_{\mathrm{w}} = d - d_{\mathrm{hh}}$, respectively.

Least-squares fit. To obtain structural parameters from SAXS data, the experimental scattering intensities $I_{\mathrm{exp}}(q_i)$ with data points $i = 1, ..., N$ recorded at q_i, were fitted by the model curve $I_{\mathrm{mod}}(q_i)$, accounting for a scaling factor and a constant background as

$$I_{\mathrm{tot}}(q) = c_1 \cdot I_{\mathrm{mod}}(q) + c_2 \,. \tag{3.10}$$

The quality of the fit was monitored by the reduced χ^2-function

$$\chi^2_{\mathrm{red}} = \frac{\sum_{i=1}^{N} \frac{[I_{\mathrm{exp}}(q_i) - I_{\mathrm{tot}}(q_i)]^2}{\sigma_i^2}}{N - p - 1} \,, \tag{3.11}$$

where p is the number of free model parameters and σ_i^2 is the variance of the intensity $I_{\mathrm{exp}}(q_i)$ for a measured data point i. Nonlinear least-squares fitting was implemented using the MATLAB function *lsqnonlin* of the MATLAB R2018b Optimization Toolbox.

For the bilayer structure, a symmetric profile was enforced, reducing the number of free parameters. The Gaussian parameters representing the headgroups are $\sigma_{\mathrm{h}} = \sigma_{\mathrm{h1}} = \sigma_{\mathrm{h2}}$ and $\rho_{\mathrm{h}} = \rho_{\mathrm{h1}} = \rho_{\mathrm{h2}}$. While the width σ_{c} of the Gaussian representing the chain region is a free parameter, the amplitude and the position were fixed to $\rho_{\mathrm{c}} = -1$ (arb. units) and $z_{\mathrm{c}} = 0$ (nm), respectively. The positions of the two outer Gaussians are denoted $z_{\mathrm{h1,2}} = \pm z_{\mathrm{h}}$. Estimation for standard deviation of the fit parameters was performed by calculation of the variance-covariance matrix approximated by $\mathrm{cov} = \mathrm{resnorm} \cdot (J^T J)^{-1}/N$.

3.4 Results and Discussion

3.4.1 Vesicle adhesion in the strong coupling regime

First, we have studied vesicle adhesion as a function of the divalent cations ($CaCl_2$, $SrCl_2$, and $ZnCl_2$) and as a function of the surface charge density σ_s by varying the content of DOPS in the DOPC:DOPS mixture. Previously, it was shown, that the addition of $CaCl_2$ and $MgCl_2$ to a suspension consisting of 100 nm extruded DOPC:DOPS (1:1) vesicles, resulted in a stable adhesion state [145]. The obtained interbilayer spacing was well reproduced by the strong-coupling theory. Moreover, d_w was approximately the same for $CaCl_2$ and for $MgCl_2$, and was independent of the concentration of the ions. Contrarily, ν was increased when increasing the ion concentration. This indicates, that the concentration of the divalent ions has a minor effect on the equilibrium interbilayer spacing, but indeed affects the fraction of adhered bilayers.

The characteristic shape of the SAXS signal from adhered vesicles is discussed in detail in [145]. Briefly, in the case of vesicle adhesion, structure factor modulations can be observed in a most pronounced manner between the characteristic form factor minima of the lipid bilayer (depending on the bilayer thickness, approximately in the q-range of 0.4 and 2.5 nm^{-1}). The structure factor modulations are superimposed by the bilayers form factor, so that the minima of the structure factor exhibit a smooth profile. The intermediate modulations of the structure factor vary in a characteristic manner with d_w.

Here, we extend the the previous study by using other divalent salts as well as by using different molar ratios in the DOPC:DOPS mixtures. Moreover, the results presented in Fig. 3.2 will be an important basis for the time-resolved SAXS experiments discussed later. Fig. 3.2(a,b) shows a series of SAXS data of lipid vesicles prepared in a 100 mM glucose solution, in which structural changes were induced by (a) $ZnCl_2$ and $SrCl_2$ for DOPC:DOPS (1:1), and by (b) $CaCl_2$ for DOPC:DOPS (1:1, 1:2, and 1:4). Comparing the SAXS signal with the pure lipid vesicle suspension, e.g. no salt added, structure factor modulations characteristic for the adhesion state can be observed for almost all cases except for DOPC:DOPS (1:4), where two Bragg peaks are visible. This indicates, that increasing the surface charge density by increasing the content of DOPS results in a collapse of the vesicles and to an rearrangement of the vesicles to a multilamellar state at a certain point. Previously, this observation was also made with pure DOPS vesicles suspended in ultra-pure water [145].

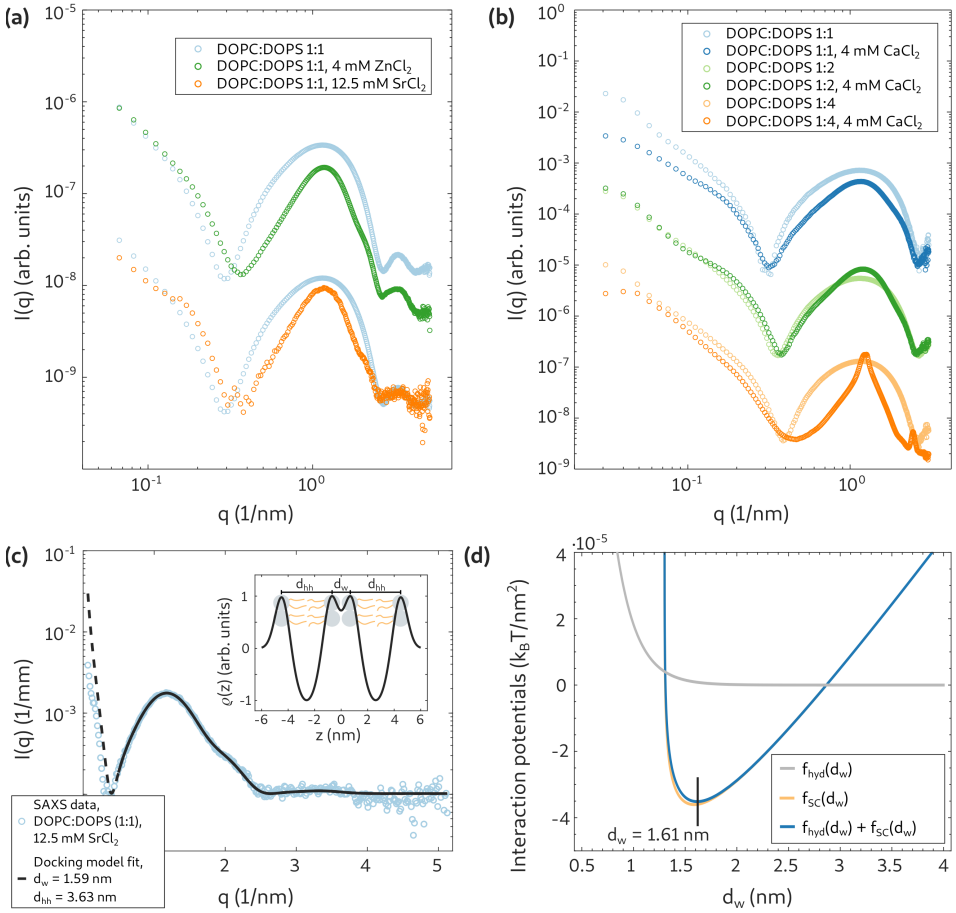

Fig. 3.2: SAXS experiments at ID02 using the flow through cell. (a) SAXS data of DOPC:DOPS (1:1) vesicles suspended in a 100 mM glucose solution, both with and without the addition of the divalent salts $ZnCl_2$ and $SrCl_2$. (b) SAXS data of DOPC:DOPS (1:1), (1:2), and (1:4) vesicles suspended in a 100 mM glucose solution, both with and without the addition of $CaCl_2$. (c) DOPC:DOPS (1:1), 12.5 mM SrCl2, docking model fit, $d_w = 1.59$ nm, $d_{hh} = 3.63$ nm. (d) The strong-coupling potential (orange line) yields an attractive interaction of like-charge membranes at small separations. By adding the hydration repulsion, an equilibrium water spacing of $d_w \approx 1.6$ nm is found, in agreement to the experimental finding. The following simulation parameters have been used: $\sigma_s = 0.5/64\, e/\text{Å}^2$ assuming an area per lipid headgroup of 64 Å^2, $l_B \simeq 7.11 \cdot 10^{-10}$ m, $\mu \simeq 1.43 \cdot 10^{-10}$ m, $d_h = 13 \cdot 10^{-10}$ m (FWHM, taken from the fit result in (c)), $\lambda_h = 2 \cdot 10^{-10}$ m, $P_h = 3.3 \cdot 10^9$ Jm^{-3}, $T = 294$ K.

The quantitative analysis of the adhesion state is exemplified in Fig. 3.2(c) for DOPC:DOPS (1:1) with the addition of 12.5 mM $SrCl_2$. From the docking model fit, the effective electron density profile (EDP) and the interbilayer spacing, here $d_w \approx 1.6$ nm, are obtained as indicated in the inset. The results are well in line with the previous studies [145] for $CaCl_2$ and $MgCl_2$. The structural parameters are summarized in Tab.3.1. The modeling of the interaction potentials by using the strong-coupling theory for the dominating attraction between the like-charge bilayers and an additional hydration potential for the repulsion is shown in (d) using the parameters described in the caption. The experimentally obtained interbilayer spacing of $d_w = 1.6$ nm can be well reproduced by the superposition of the strong-coupling potential and the hydration potential. Thus, the small bilayer separations, e.g. strong like-charge attraction between the bilayers, are the result of ion-correlation effects associated with strong coupling according to theory. The simulation parameters are as summarized in the caption of Fig. 3.2.

Note, that further flow-through SAXS experiments were performed to study the reaction between DOPC:DOPS (1:1) vesicles and the trivalent salts $FeCl_3$, $Al_2(S0_4)_3$, and $MgSO_4$ as shown in the supplementary material (Appendix A.2, Fig. A.9). In those cases, no signature was observed which could be attributed to the docking state of vesicles. Instead, phase transitions to different multilamellar states were observed.

Tab. 3.1: Structural parameters obtained by SAXS analysis using the docking model. For all fits a symmetric bilayer profile was applied, so that $\rho_h = \rho_{h1} = \rho_{h2}$ and $\sigma_h = \sigma_{h1} = \sigma_{h2}$. The amplitude of the Gaussian representing the chain region $\rho_c = -1$ (arb. units) for all fits.

Sample	ρ_h (a.u.)	σ_h, σ_c (nm)	d_{hh} (nm)	d_w (nm)	$(1-\nu)$	χ^2_{red}	Ref.
DOPC:DOPS (1:1), 4 mM CaCl2	1.39	0.44, 0.95	3.71	1.56	0.89	1.14	[145]
DOPC:DOPS (1:1), 4 mM MgCl2	1.34	0.39, 0.84	3.72	1.72	0.98	0.89	[145]
DOPC:DOPS (1:1), 12.5 mM SrCl2	1.14	0.54, 0.98	3.63	1.59	0.83	1.44	-
DOPC:DOPS (1:1), 4 mM ZnCl2	1.13	0.48, 0.89	3.63	1.59	0.85	101.76	-
DOPC:DOPS (1:2), 4 mM CaCl2	1.31	0.46, 0.91	3.75	1.26	0.85	17.63	-

3.4.2 SAXS combined with the stopped-flow rapid mixing device

Next, structural dynamics of vesicle adhesion and fusion upon mixing with divalent salts was studied by time-resolved SAXS combined with the stopped-flow technique. Fig. 3.3 shows the time-resolved SAXS data of DOPC:DOPS vesicles with the a molar ratio of (a) 10:1, (b) 1:1 and (c) 1:4, either mixed with 15 mM $CaCl_2$ (a,c) or 25 mM $SrCl_2$ (b). After mixing, the first SAXS image is recorded approximately 0.05 after starting the measurement script, subsequently following the reaction over a time window of approximately 92 s (a,c) and 316 s (b). However, subtracting the dead time of the stopped flow mixing time, the true kinetic time can be smaller down to the millisecond range, accounting for an offset between the elapsed time in the data acquisition and the kinetic time. In all data sets, different states along the reaction pathway can be distinguished as a function time. In particular, the transition of unilamellar vesicles to adhered vesicles is visible, even if the final states are different. For DOPC:DOPS (10:1), notably, the final state is difficult to attribute. The docking modulation seems to be superimposed with several smaller (structure factor) peaks indicative of short range order between several adhering bilayers. Osmotic shrinkage of vesicles may also contribute to the signal.

For DOPC:DOPS (1:4), the final state is clearly characterized by the structure factor of multilamellar vesicles. This state is reached from a transient docking state. As revealed by the least-square fits, the collapse of vesicles occurs at $\nu \approx 0.5$. For the observation of the intermediate state of adhered vesicles in this system, the time-resolved SAXS combined with the stopped-flow technique was essential. SAXS experiments using the flow-through cell could only reveal the initial state of unilamellar vesicles without mixing with $CaCl_2$, and the final state of multilamellar vesicles by measuring the equilibrated reaction upon mixing with $CaCl_2$ (cf. Fig. 3.2). The quantitative analysis of the adhesion state is exemplified in (d) for representative SAXS curves of each data set, where the typical structure factor modulation associated with docking are observed.

Fig. 3.4 shows the main structural results combining the analysis of the stopped-flow SAXS data and of the flow-through SAXS data. The structural parameters d, d_{hh} and d_{w} are displayed in (a) as a function of the molar ratio of DOPC:DOPS (10:1, 1:1, 1:2, and 1:4). For (10:1), (1:1), and (1:4) the structural parameters are the mean values from the time-course analyzed by docking model fits to the stopped-flow SAXS data (corresponding to the analysis of at least ten SAXS signals, where a clear adhesion state could be identified). As shown in Fig. A.9, the structural parameters d_{hh} and d_{w}

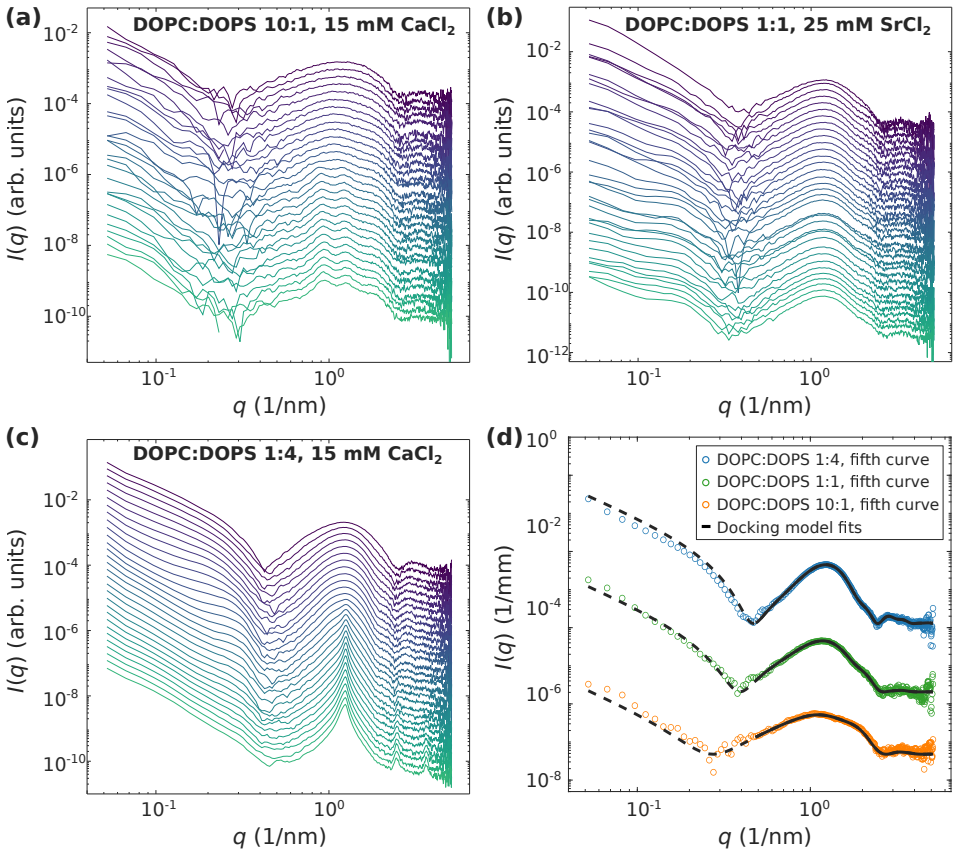

Fig. 3.3: Time-resolved SAXS data of 20 mg/ml DOPC:DOPS vesicles with varied surface charge density mixed with either 15 mM $CaCl_2$ (a,c) or with 25 mM $SrCl_2$ (b) obtained by using the stopped-flow rapid mixing device. The vesicles were either suspended in ultra-pure water (a,c) or in a 100 mM glucose solution (b). The background corrected SAXS data is shifted for clarity. (a) 30 frames, first frame 0.05 s after mixing, last frame 91.95 s. The exposure time was 0.005 s. (b) 35 frames, first frame 0.04 s after mixing, last frame 316.16 s. The exposure time was 0.02 s. (c) 30 frames, first frame 0.055 s after mixing, last frame 92.099 s. The exposure time was 0.01 s. (d) Representative docking model least-squares fits to the SAXS data from (a-c) show that adhesion states can be well identified, either as intermediate (a,c) or as final states (b). The SAXS data of DOPC:DOPS (1:1) and DOPC:DOPS (10:1) as well as the corresponding fits are shifted for clarity.

remain nearly constant over time. The error is given as the standard deviation of the mean. For the molar ratio of (1:2), the results are from the analysis of the flow-through SAXS data shown in Fig. 3.2(b). The error is calculated by the approximated parameter co-variance matrix of the least-squares fit.

In (a) it can be observed that with an increasing σ_s, i.e. increasing content of DOPS, the structural parameters d and d_w decrease, while d_{hh} shows a slight increase. While those parameters remain nearly constant over time, in (b) we can observe that $(1-\nu)$ as a measure of the fraction of single (undocked) bilayers decreases significantly as a function of time for all stopped-flow data sets shown here. The increase of the fraction of adhered bilayers is most pronounced for DOPC:DOPS (1:4), indicating that the surface charge density σ_s is an important factor for triggering the adhesion-reaction. Prior to the collapse of the DOPC:DOPS (1:4) vesicles (cf. Fig. 3.3(c)), inferred from the emerging Bragg peak, the fraction of adhered bilayers is $\nu \approx 0.5$. Contrary, for DOPC:DOPS (10:1) and for DOPC:DOPS (1:1) $\nu \approx 0.1$ and ≈ 0.2, respectively.

In (c), the structural parameter d_w obtained by the docking model analysis of the SAXS data (shown in (a)) is plotted as a function of $d_{w,sim}$ obtained from the simulations of the strong coupling theory. It can be observed, that the experimentally measured water spacings of the lipid bilayer, obtained for the different σ_s values, are well in line with the predictions from the strong coupling theory. For the simulated water distance predicted by strong coupling, the following parameters were chosen and kept constant for all systems: area per lipid headgroup $d_{AH} = 64$ Å^2, $l_B \simeq 7.11 \cdot 10^{-10}$ m, $\lambda_h = 2 \cdot 10^{-10}$ m, $P_h = 3.3 \cdot 10^9$ Jm^{-3}, and $T = 294$ K. In contrast, the thickness of the headgroup $d_{h,FWHM}$ is taken from the fit results of d_h by calculating the full width half maximum (FWHM), and more importantly, the surface charge density σ_s is varied corresponding to the molar ratios of the DOPC:DOPS mixtures and the Gouy-Chapman length μ is calculated accordingly. Further, it is of interest to also discuss the multi-lamellar final state of the DOPC:DOPS 1:4 system in view of strong coupling. From the position of the first Bragg peak $q_{n=1} \approx 1.208$ 1/nm, we obatain $d \approx 5.2$ nm, and by subtraction of the bilayer thickness (as obtained from the least-square fit of the adhesion state), the water layer can be determined to $d_w \approx 5.2 - 3.935 = 1.27$ nm, again in good agreement with the predicted value $d_{w,sim} \approx 1.25$ nm. All additional fit results, in particular for d_{hh} and d_w as a function of time are shown in the appendix (Fig. A.8).

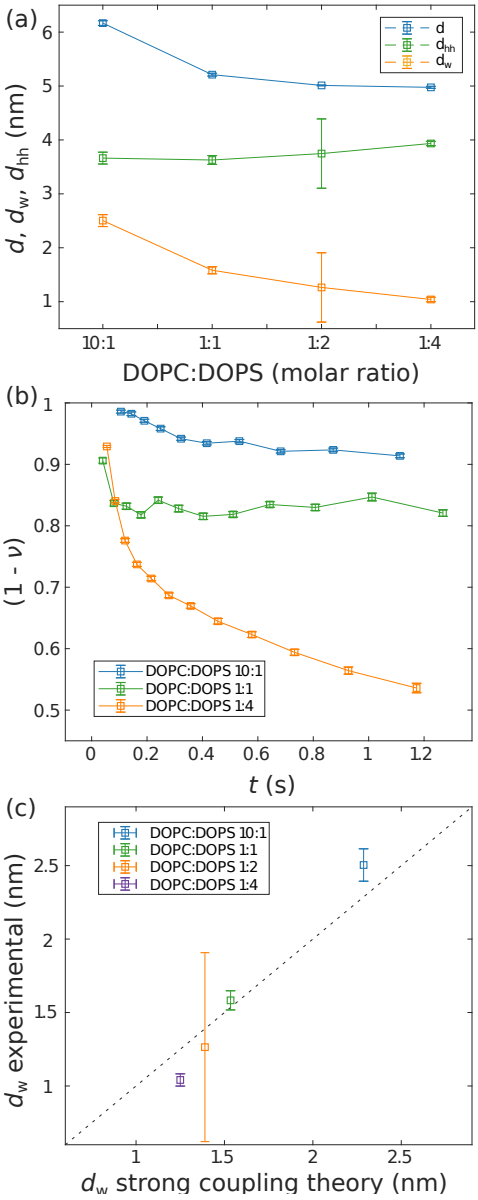

Fig. 3.4: Analysis of the vesicle adhesion. (a) Structure of the adhesion state: The structural parameters d, d_{hh} and d_w for different molar ratio of DOPC:DOPS. The values for molar ratios (10:1), (1:1), and (1:4) are the mean of all least-square fit results for curves corresponding to the adhesion state in the stopped-flow SAXS series shown in Fig. 3.3. The corresponding standard deviation of the mean is taken as errorbar. For the molar ratio (1:2) the parameters are obtained from the flow-through SAXS data shown in Fig. 3.2. Here, the errorbar is given by the estimated standard deviation of the least-squares analysis. (b) Kinetics of adhesion: The surface fraction $(1-\nu)$ of non-adhered bilayers as a function of time, obtained from least-squares analysis of the stopped-flow SAXS. (c) Analysis of the strong coupling regime: each data point represents a different system with varied charge density σ_s and corresponding coupling parameters, notably $\Xi_{(10:1)} = 3.97$, $\Xi_{(1:1)} = 19.84$, $\Xi_{(1:2)} = 26.19$, and $\Xi_{(1:4)} = 29.76$. The experimentally determined water layer thickness d_w is plotted against the value predicted by the strong coupling theory. We can deduce that within the probed range of the four different coupling parameters, prediction and measurement are reasonably close, with a correlation coefficient $r = 0.9948$. The fact, however, that only 2 out of the 4 points are within error bars may suggest that the experimental error is slightly underestimated.

3.4.3 SAXS combined with microfluidics

After the evaluation of stopped-flow SAXS for vesicle adhesion, it is of interest to briefly address the suitability of a microfluidics setup for similar studies. Note that stopped flow and microfluidics sample environment could potentially access regimes, which are complementary in temporal resolution. With typical flow velocities on the order of $v_F \simeq 1 - 10$ mm/s and minimal spatial sampling $\delta x \simeq 1 - 10$ μm defined by the relevant diffusion lengths and/or beam size, smallest reaction times would range in 100 μs $\leq t_{min} \leq$ 10 ms, well below those accessible by the stopped flow chamber. At the same time, a SAXS image of the interaction zone is obtained by scanning SAXS, and potentially a down-scaling of the total volume. On the other hand, a tighter beam focus will compromise SAXS data quality. Further, the material and window choices compatible with microfluidics devices are more restrictive than those for stopped flow. To evaluate suitability, limitations and instrumental settings, we have carried out two exploratory microfluidics SAXS experiments, the first one using scanning SAXS with a micro-focused beam of 2.5 μm (horizontal) $\times$ 1.3 μm (vertical) at the GINIX endstation of the P10 beamline (PETRAIII storage ring, DESY), the second using a 30 μm (horizontal) $\times$ 30 μm (vertical) collimated beam defined by slits at the ID02 beamline (ESRF). For both experiments, identical home-built microfluidics devices made of Topas were used, placed vertically in a device holder with adaptation for tubing. The device holder was then positioned in the beam on the sample stage.

Fig. 3.5 presents an overview of the setup and illustrates the micro-focus SAXS experiment at GINIX. In Fig. 3.5(a) a photo of the microfluidics device is shown, mounted on the sample tower, for alignment and subsequent scanning in x, y, and z. Coarse alignment and inspection of the flow was enabled by an on-axis video camera (OAV). A microfluidics layout with four-inlet/one-outlet channels was chosen for all devices. Flow properties were simulated by finite elements (COMSOL), see Fig. 3.5(b). Lipid vesicles were simulated as particles with 60 nm in diameter with the diffusion constant of $D \approx 8 \cdot 10^{-12}$ m^2/s and injected into the upper diagonal inlet. The flow rates are 100 μL/h and 25 μL/h for the diagonal inlets and for the side inlets, respectively. In this configuration, the side inlets focus the flow from the diagonal inlets. Along the outlet, diffusion of the particles outside of the focused stream can be observed. Finally, Fig. 3.5(c,d) show examples of integrated scattering intensity maps (darkfield maps), as recorded by scanning-SAXS with 1s accumulation time for each frame. As indicated, 10 mg/ml extruded DOPS vesicles and 10 mM $CaCl_2$ suspended in ultra-pure water were injected through the diagonal inlets at the flow rates of 25 μl/h to study the

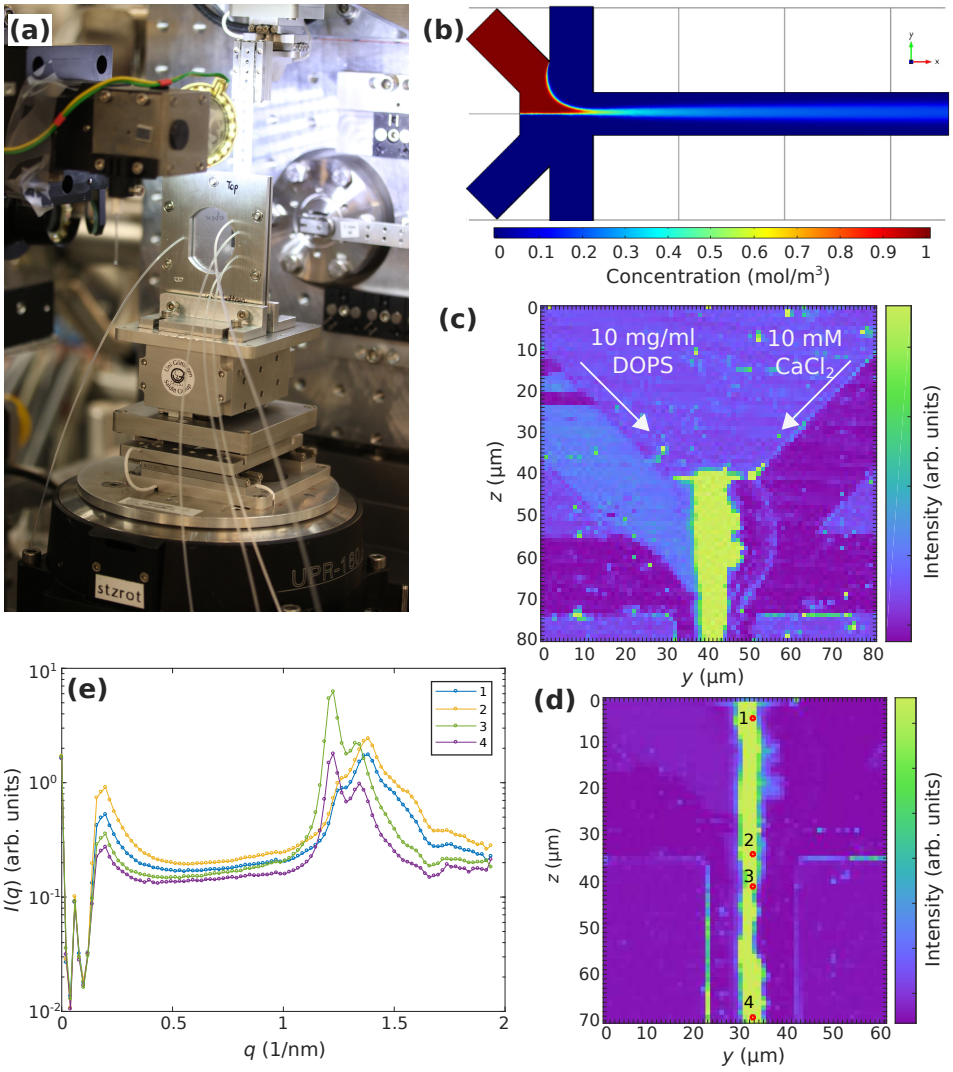

Fig. 3.5: (a) Photograph of the microfluidics setup integrated into the GINIX endstation at P10, DESY. (b) COMSOL simulation of a microfluidic flow profile showing the concentration of the particles representing lipid vesicles with the diffusion constant of $D \approx 8 \cdot 10^{-12}$ m^2/s. (c) Darkfield of the microfluidics device obtained by scanning-SAXS. 10 mg/ml DOPS vesicles are mixed with 10 mM $CaCl_2$ suspended in ultra-pure water and injected through the diagonal inlets with the flow-rates of 25 μl/h. Ultra-pure water is injected through the side inlets with the flow-rates of 100 μl/h. (d) Darkfield of the microfluidics device shown in (c) obtained by scanning-SAXS, showing a larger scan of the outlet. (e) Selected 1d curves corresponding to the positions marked in (d). Along the reaction path (position 1 to 4), a transition from an rather aggregated state (1,2) to a co-existing multilamellar state can be observed.

reaction upon mixing along the outlet. Ultra-pure water was injected through the side-inlets at the flow rates of 100 μl/h. Each pixel represents the integrated photon counts from a single 2d-diffraction pattern. The darkfield images show an increase of the intensity in the vesicle inlet as well as in the mixing region, corresponding to the scattering from vesicles. In particular, a large increase of the intensity can be observed after the mixing of DOPS vesicles with $CaCl_2$. The one-dimensional curves $I(q)$ vs. q, obtained by azimuthal integration of the 2d diffraction patterns, are exemplified in Fig. 3.5(e) for selected points along the reaction line. The corresponding locations are indicated by numbers in Fig. 3.5(d). Note that the raw data are shown before background subtraction. Qualitatively, the curves 1 and 2 show an aggregated state of vesicles with an emerging multilamellar Bragg peak modulated by the bilayer form factor. Along the outlet, a phase coexistence regime of different multilamellar states can be observed, see Bragg peaks of curves 3 and 4. From previous experiments it is known that DOPS vesicles mixed with $CaCl_2$ show a transition to a monophasic multilamellar state [145]. Accordingly, the multilamellar state obtained from the microfluidics SAXS experiments shown here has not reached its equilibrium state.

The darkfield maps and the SAXS curves reveal the limitations of the configuration: high background and limited q-range. Aside from background generated by the chamber itself, the micro-focusing by compound refractive lenses (CRL) and the relatively large beam path in air both compromise the SAXS quality. While the strong multilamellar signals can still be extracted under these conditions, the much weaker signal of unilamellar vesicles (see the vesicle inlet in the darkfield map) does not reveal much structural information. For this reason, the second experiment at ID02/ESRF used a much more optimized configuration for SAXS, and keeping air paths at minimum, albeit sacrificing spatial and hence also temporal resolution.

Fig. 3.6 and 3.7 presents examples of SAXS data recorded in this configuration. In this setting, it became possible to study vesicle adhesion of DOPC:DOPS mixtures at varied molar ratios mixing with $CaCl_2$. Fig. 3.6 shows the results obtained by microfluidics SAXS for DOPC:DOPS (1:1) vesicles mixed with a 4 mM $CaCl_2$ solution suspended in ultra-pure water. The samples were injected through the diagonal inlets as indicated in (a) by the darkfield obtained by scanning SAXS of the microfluidic device. The flow rates were 100 μl/h and 0 μl/h for the diagonal and the vertical inlets, respectively. For a point-wise background subtraction, the device was previously measured with only ultra-pure water being injected in the channels. (b) shows an example of a background corrected SAXS signal corresponding to the position $\boxed{1}$ highlighted in the darkfield. The background corrected SAXS signal were analyzed by fitting the docking model

to the SAXS data as exemplified in (c) for three SAXS signals, corresponding to the positions 1, 2 and 3 highlighted in the darkfield. For the positions 1 and 3 no reaction with $CaCl_2$ is expected, while position 2 corresponds to the mixing region. The fraction of adhered bilayers quantified by ν is slightly increased for the SAXS signal from position 2 ($\nu = 0.04$ at position 2, compared to $\nu = 0.01$ at position 1, and 3), indicating that a small adhesion-reaction can be observed. The water spacing $d_w \approx 1.7$ nm is well in line with the results obtained by flow-through and stopped-flow SAXS discussed above.

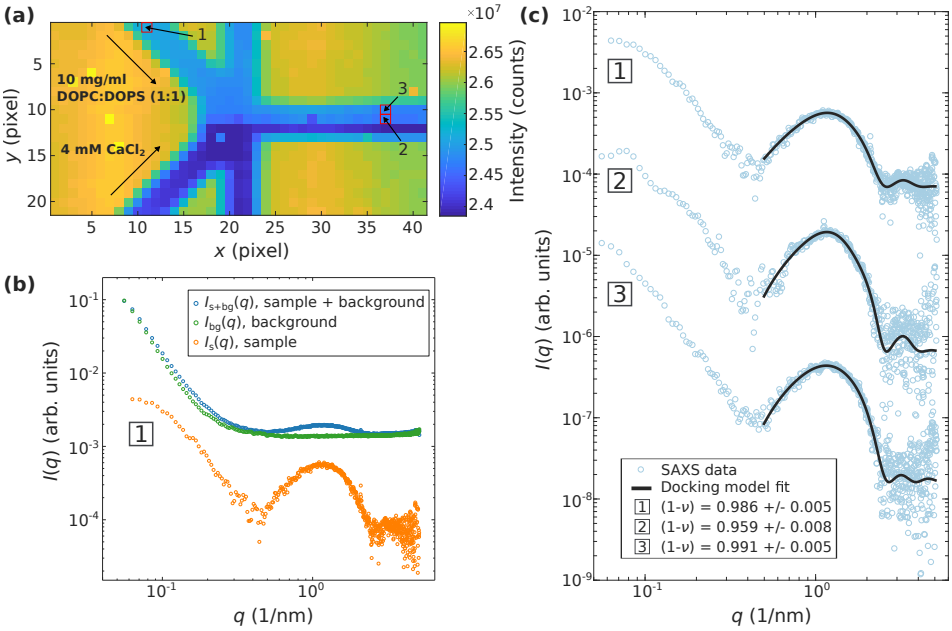

Fig. 3.6: Scanning-SAXS combined with microfluidics for the investigation of the reaction of 10 mg/ml DOPC:DOPS (1:1) vesicles with 4 mM $CaCl_2$, both suspended in ultra-pure water, in a microfluidic flow. (a) Darkfield of the microfluidics device obtained by scanning-SAXS. The exposure time was 1 s for each pixel. The value shown in each pixel is the integrated intensity of the two dimensional SAXS pattern recorded at the respective position. The flow rates are 100 μl/h and 0 μl/h for the diagonal and the vertical inlets, respectively. The inlets of the DOPC:DOPS (1:1) vesicles and the $CaCl_2$ solutions are as indicated. (b) Example of a background corrected SAXS signal $I(q) = I_{s+bg}(q) - I_{bg}(q)$ obtained from DOPC:DOPS (1:1) vesicles. The background (ultra-pure water) was measured separately by scanning SAXS in the same microfluidics device, so that background correction can be performed at the same position. (c) Docking model fits to SAXS data corresponding to the positions 1, 2 and 3 highlighted in the darkfield in (a). The structural parameter $(1 - \nu)$ is significantly lower for the SAXS data from position 2, indicating adhesion of vesicles in the mixing region.

Fig. 3.7 shows much stronger evidence for the adhesion state for DOPC:DOPS (10:1)

vesicles and 10 mM $CaCl_2$, again along with the corresponding least-square fits. However, this signal is observed only at the stagnation point (almost zero flow rate), and not at other points in the channel with higher flow rates, see the darkfield map in (a) with the point of stagnation highlighted by a red box $\boxed{1}$. The scattering curves $I(q)$ vs. q taken from the point of stagnation show indeed the characteristic structure factor modulations corresponding to adhesion of the vesicles, which is exemplified in (b) by the background corrected SAXS signal corresponding to the position marked in (a). The docking model analysis reveals an interbilayer spacing of $d_w = 2.4$ nm, which is in good agreement with the results obtained by the stopped-flow SAXS data and the theory of strong coupling, as discussed above.

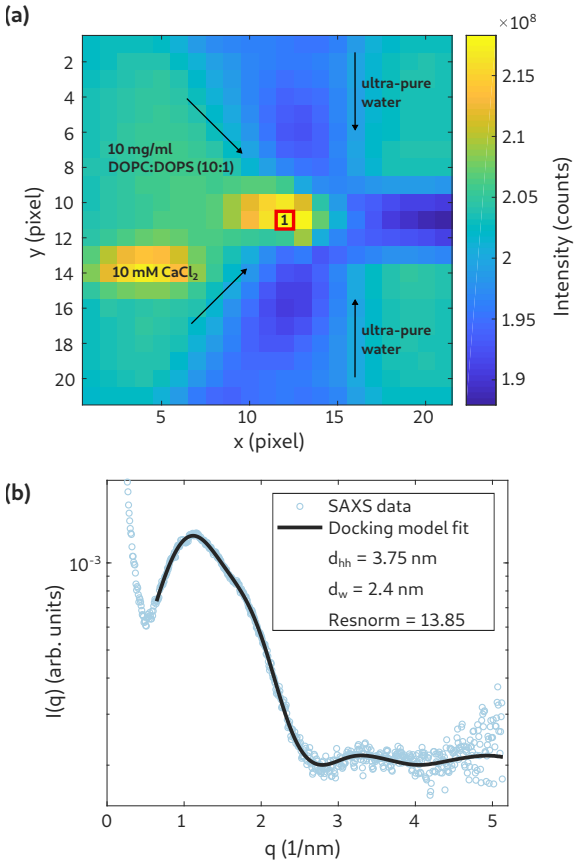

Fig. 3.7: Scanning-SAXS combined with microfluidics for the investigation of the reaction of 10 mg/ml DOPC:DOPS (10:1) vesicles with 10 mM $CaCl_2$, both suspended in ultra-pure water, in a microfluidic flow, with a particular focus on the point of stagnation. (a) Darkfield of the microfluidics device obtained by scanning-SAXS. The exposure time was 1 s for each pixel. The value shown in each pixel is the integrated intensity of the two dimensional SAXS pattern recorded at the respective position. The flow rates are 50 μl/h and 100 μl/h for the diagonal and the vertical inlets, respectively. The inlets of the DOPC:DOPS (10:1) vesicles and the $CaCl_2$ solutions are as indicated. (b) Docking model fit to the background corrected SAXS curve $I(q)$ vs. q corresponding to the position highlighted in (a) by the red rectangle.

3.5 Conclusions

We conclude that time-resolved SAXS with a stopped-flow chamber reveals a transient adhesion state induced by divalent ions for vesicles with high charge density before the system transforms to a multilamellar phase. This transient state could not have been observed with static SAXS, and gives important clues about the conditions of arrested adhesion, i.e. meta-stable vesicle binding versus topological transformation into multilamellar vesicles. The first scenario, which we have already observed before by static SAXS, applies to low and moderate charge density, and is associated with only a small adhesion zone (low parameter ν). Contrarily, the full reaction to a multilamellar state is preceded by a large surface of adhesion, presumingly providing the energy required to overcome the barriers of vesicle rupture. At the same time the water layer thickness in the adhesion zone is in both cases governed by strong electrostatic interaction.

The current study has also solidified and extended the experimental basis of this very interesting effect of like-charge attraction, predicted by the theory of strong coupling. For the first time, the surface charge density of the bilayers and hence the coupling parameter was varied to study the corresponding variation in water layer distance. To this end, different molar ratios of the DOPC:DOPS mixtures were probed. Our previous study of vesicle adhesion in a DOPC:DOPS (1:1) mixture [145] was also extended concerning the type of divalent ions used. As we have shown, adhesion is induced not only by $CaCl_2$ and $MgCl_2$, but also by $SrCl_2$ and $ZnCl_2$. Importantly, variation of ions results only in small changes of the water layer thickness, as expected from strong coupling theory. Whether ion radius and polarizability can account for these differences remains to be investigated. The interbilayer spacings for different surface charge densities, i.e. for different coupling parameters ranging from $\Xi \approx 4 \ldots 30$, were in good agreement with the strong coupling theory. Deviations between the experiments and the simulations of the strong coupling theory could eventually be attributed to a change of the effective dielectric constant of water, which was kept constant ($\epsilon = 80$) for all coupling parameters. Recent water-explicit numerical simulations of nanometer-separated charged surfaces revealed a surface charge-induced reorientation of hydration water, which modifies the dielectric constant of water as well es the hydration repulsion [161].

Concerning experimental settings, we conclude that the signal quality of scanning SAXS with focused beams, while desirable in terms of temporal and spatial resolution, strongly compromises data quality at the present configurations. Future improvements

will address more options for cleaning of the beam as well as a configuration with tightly evacuated flight paths. Further reduction of the chamber background scattering for example by thinner windows (presently 120 μm total thickness), and possibly also by the processing protocol are also important. Finally, a layout with 5 inlets would be well suited to avoid a stagnation point, which often led to unwanted formation of large lipid aggregates which in turn impeded proper microfuidic flow.

With all of these improvements in place, we anticipate that both microfluidics and stopped flow experiments will enable kinetic studies of vesicle transformation and reactions in a complementary manner. Already in the present proof-of-concept study and under current parameters, the time-resolved SAXS data has allowed us to probe the structure of a transient adhesion state of highly charged vesicles induced by calcium injection. Importantly, the binding of like-charged vesicles in this state results in a spacing which is in very good agreement with strong binding theory, predicted more than fifteen years ago. This example demonstrates, that transient vesicle states can not only be evidenced but that the corresponding structures can be described in quantitative terms. This opens up an interesting perspective in applications of this approach for biological vesicles undergoing shape transformations and functionally important transitions. Understanding the docking and fusion reaction of synaptic vesicles (SVs), for example, is of significant interest in view of a quantitative understanding of chemical synapses. To this end, we include a first test exposure of SVs in a microfluidics device, comparing the present data quality with respect to static SAXS (Fig. A.10).

Acknowledgments

We thank Theyencheri Narayanan and Michael Sprung for excellent working conditions and advice at beamlines ID02/ESRF and P10/PETRAIII (DESY), respectively, and Theyencheri Narayanan in particular for the introduction to the stopped-flow instrumentation. We acknowledge Diego Pontoni and Pierre Lloria for sharing their resources and expertise and the entire support provided in the framework of the Partnership for Soft Condensed Matter (PSCM) before and during our beamtimes at ESRF. We thank Yihui Xu, Kilian Frank and Max Scheu, for support during beamtimes, and Susanne Hengst for help in sample preparation. We also thank Julia Preobraschenski, Marcelo Ganzella and Reinhard Jahn for a related collaboration on synaptic vesicle SAXS, which has motivated some of the technical aspects of this study, and which will be reported in a forthcoming publication. Further, we acknowledge ESRF and DESY photon

science for beamtime. This work was supported financially by Sonderforschungsbereich 803 "Functionality Controlled by Organization in and between Membranes", and by Sonderforschungsbereich 1286 "Quantitative Synaptology", funded by Deutsche Forschungsgemeinschaft.

Neurotransmitter uptake and fusion of synaptic vesicles studied by X-ray diffraction

4

Karlo Komorowski, Julia Preobraschenski, Marcelo Ganzella, Jette Alfken, Charlotte Neuhaus, Reinhard Jahn, and Tim Salditt
Unpublished work (2021)

The size, polydispersity, and electron density profile of synaptic vesicles (SVs) can be studied by small-angle X-ray scattering (SAXS), i.e. by X-ray diffraction from purified SV suspensions in solution. Here we show that size and shape transformations, as they appear in the functional context of these important synaptic organelles, can also be monitored by SAXS. In particular, we have investigated the active uptake of neurotransmitters, and find a mean vesicle radius increase of about 8% after the uptake of glutamate, which indicates an unusually large extensibility of the vesicle surface, likely to be accompanied by conformational changes of membrane proteins and rearrangements of the bilayer. Changes in the electron density profile (EDP) give first indications for such a rearrangement. Details of the protein structure are screened, however, by SVs polydispersity. To overcome the limitations of large ensemble averages and heterogeneous structures, we therefore propose serial X-ray diffraction by single free electron laser pulses. Using simulated data for realistic parameters, we show that this is in principle feasible, and that even spatial distances between vesicle proteins could be assessed by this approach.

4.1 Introduction

Neurotransmission at chemical synapses relies on synaptic vesicles (SVs) as highly specialized small organelles containing neurotransmitters. Triggered by an influx of

Ca^{2+} during neuronal stimulation, SVs fuse with the plasma membrane (exocytosis), release their neurotransmitter content into the synaptic cleft, and are recovered again by endocytosis only to be refilled with neurotransmitter for the next round of exocytosis [1, 3]. A comprehensive molecular model integrating all quantitative data on the protein and lipid composition of the SV has been presented in [4], and is shown in Fig. 4.1(a). SVs and in particular the SNARE (soluble N-ethylmaleimide-sensitive-factor attachment receptor) protein machinery regulating SV fusion have been intensively studied [17, 23, 15]. While molecular composition of SVs can be well analyzed by various biochemical techniques, and the structure of its protein constituents by structural biology techniques [162], structural details at level of the organelle level, in particular regarding the arrangement of proteins and lipids are difficult to obtain directly from microscopy techniques. Given the small SV radius around $R \simeq 19$nm, imaging of SVs by fluorescence microscopy requires super-resolution techniques [163] or electron microscopy (EM) of cryogenically vitrified sections [4], in which inner and outer protein layers can be discerned, however, without much structural details. Using small-angle x-ray scattering (SAXS), our group has investigated the size and structure of purified SVs directly in solution [104]. Based on a scattering model [107, 104], which is illustrated in Fig. 4.1(b), we could deduce detailed size and density parameters for the protein layers, as well as structural information about the lipid bilayer. A laterally anisotropic structure for the protein shell, indicative for protein microdomains yielded very satisfactory least-square fits of the measured SAXS, while a rotationally symmetric density profile fitted the data less well [104].

A prerequisite for analysis, both chemical and structural, is the purification of SVs in sufficient quantity. Even measurements of size as the presumingly most basic structural parameter, can in fact be already quite challenging for biological vesicles [164, 165, 166]. For SVs, measurements are facilitated by the large SV abundance in brain tissue and the relative size and shape homogeneity. Compared to most other vesicles and organelles, the polydispersity of SVs is relatively small, but not small enough to enable cryo-EM single particle reconstructions, which requires monodisperse particles. SAXS analysis is also significantly affected by polydispersity, as discussed further below in this work. For this reason, SAXS is also very well suited to validate purification protocols. However, at some point the intrinsic heterogeneity associated with the physiological processes of SV formation and recycling, as well as the corresponding variations in copy numbers will set a limit to most analysis techniques. This may come as a nuisance, but also reflects an important physiological fact which can shed light on the robustness of functional processes. As active energy-driven processes, uptake, fusion, release and

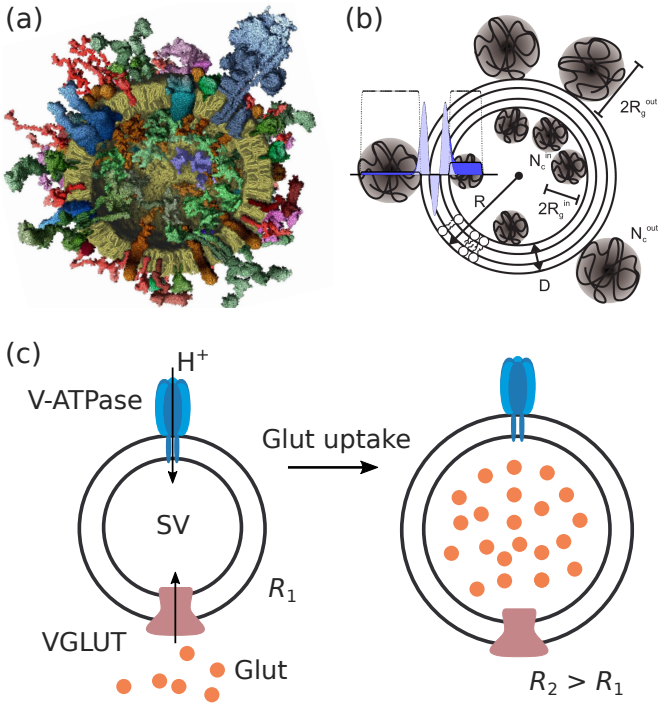

Fig. 4.1: Structure and function of synaptic vesicles (SVs). (a) Molecular model of an average SV based on biochemical knowledge, adapted from [4]. (b) Sketch of the anisotropic SAXS model. The radial electron density profile (EDP) of the lipid bilayer is modeled by the sum of three Gaussians (one Gaussian for each headgroup region and one Gaussian for the hydrophobic chain region). The inner and outer protein layers are modeled as Gaussian chains. (c) Illustration of glutamate (Glut) uptake by SVs. Glutamate is loaded by the vesicular glutamate transporter (VGLUT) into SVs. The driving energy for neurotransmitter uptake is provided by an electrochemical gradient established by a vacuolar-type ATPase (V-ATPase), which translocates protons (H^+) into the vesicle interior using the energy derived from ATPhydrolysis.

recycling require tight temporal and spatial control, and beyond the basic 'anatomy' of SVs, the next challenge is to shed more light on these processes and their structural dynamics. A particular case in point is the neurotransmitter uptake based on active pumping, for example by the vesicular glutamate transporter 1 (VGLUT1) energized by V-ATPase, as sketched in Fig. 4.1(c). Much is known already on the regulation of VGLUT1 and other vesicular neurotransmitter transporter [167], as well as on the relationship between neurotransmitter transport activity and vesicle filling [168]. The transport is driven by the V-ATPase-dependent electrochemical proton gradient ($\Delta\mu H^+$) and can be stimulated by low concentration of Cl^-. Using a reconstitution approach, it was shown that VGLUT1 contains two anion binding sites and one cation binding site, allowing the transporter to adjust to the changing ionic conditions during vesicle filling without being dependent on other transporters or channels [12]. In addition to glutamate transport, VGLUT1 can also perform bidirectional phosphate transport and may play a role in neuronal phosphate homeostasis [169].

In this work, we use SAXS combined with active SV preparations to study the size increase associated with glutamate uptake. The starting point of our investigation was the surprisingly large increase in SV radius R after glutamate uptake, up to 25%, reported in [14], corresponding to about a doubling of the volume! The effect was first observed by fluorescence correlation spectroscopy (FCS). To rule out that this was only an apparent size increase resulting from changes in the hydrodynamic radius or the diffusion properties, the authors verified the result by cryo-EM. The authors did not observe the size increase if SV-specific proteins notably SV2A (synaptic vesicle glycoprotein 2A) were absent, and discussed different models accounting for the vesicle expansion. To this end, they distinguished three different mechanisms: (i) an island model with the vesicle surface composed of non-expandable lipids and of a second phase composed of expandable protein components, (ii) a virus-like model exhibiting expandable breathing modes, and (iii) a matrix-swelling model where a gel formed by SV2A sugar moieties binds the glutamate even if the membrane ruptures upon expansion. The first goal of this work is to verify the size increase by using solution SAXS. Note that while FCS probes structural changes only indirectly via diffusion properties, cryo-EM gives direct access to the size of individual particles, but only in the vitrified state. Further cryo-EM is limited to a relatively small number of particles which can be probed. Contrarily, SAXS probes the average structure of a large ensemble, but in contrast to a direct imaging method such as cryo-EM requires least-square fitting to a parameterized model, see for example [170]. The advantage here is the fact that potentially more structural parameters can be extracted, in particular a parameterized

density profile with more details on the structural rearrangements for example in the inner and outer SV protein layers. As we show here, SAXS can confirm the size increase, albeit by a factor of about $\Delta R/R \simeq 0.08$, hence about a factor of three smaller than the largest values reported in [14]. Further, we obtain some indications for significant protein rearrangmenents (possibly conformational changes) in the protein layers. The second goal is more technical and concerns the further development of SAXS for functional SV studies in general, including not only neurotransmitter uptake or release, but also adhesion and fusion. With our earlier study of equilibrium SVs suspensions as a SAXS benchmark [104], we now ask about the potential and limitations of solution SAXS concerning functional dynamics and out-of-equilibrium processes. As we show here, while some insight and additional information can be derived from uptake studies, the level of details which can be robustly derived from the model fits is largely limited by the intrinsic polydispersity of the SV suspension. As a solution to this problem, we propose high throughput single particle coherent diffractive imaging with femtosecond X-ray free electron laser (XFEL) pulses in the outlook of this paper, and corroborate feasibility by numerical simulations.

The manuscript is organized as follows: after this introduction, the methods section details sample preparation, SAXS measurements, and also gives a brief recapitulation of the SAXS model and data analysis. In the results section we then first consider polydispersity and the improvements in purification and correspondingly homogeneity, before we address structural changes associated with SV functions. Aligned with the main goal of this work, we present the SAXS results for SVs after glutamate uptake, and quantify the associated size increase. We then also include first results of a fusion experiment monitored by SAXS. After the results section, we discuss the limiting effects of polydispersity in deducing structural parameters from scattering, and close with an outlook proposing an alternative approach based on sequential single-pulse coherent diffraction with XFEL radiation, which we substantiate with numerical simulations. In addition, dynamic light scattering (DLS) analysis of SVs and additional SAXS data as well as additional technical details are included as Supporting Material A.3.

4.2 Materials and Methods

4.2.1 Preparation of the uptake experiment

Synaptic vesicles were purified from rat brain, as described in [4, 171]. After purification, SV samples were frozen and stored at $-80°$ C. Further sample preparation was performed directly before the SAXS experiments. First, the SVs were thawed on ice for approximately 15 minutes. For buffer exchange, the SVs were dialysed against the buffer consisting of 300 mM glycine, 10 mM KCl, 5 mM HEPES, 2 mM $MgS0_4 \times 7H_2O$ (pH 7.3) at 4° C for approximately three hours. To this end, the SV samples were injected into Slide-A-Lyzer cassettes (Thermo Fisher Scientific, Waltham, MA) with a molecular weight cutoff of 2 kDa. For the uptake experiment and for the control experiment, 10 mM K-glutamate and 1 mM Mg-ATP, and 10 mM K-glutamate, respectively, was added to the SV sample and incubated in a thermo-mixer at 37° C for 10-15 minutes just before the samples were injected into the sample chamber for the SAXS experiments.

4.2.2 Preperation of proteoliposomes

For fusion of SVs with proteoliposomes, we have prepared lipid vesicles containing the ΔN acceptor complex (containing the SNAREs syb2(49-96), syx1A(183-288) and SN25(1-206)). Protein expression and purification, as well as the preparation of SNARE-liposomes was described in detail in [145, 23]. Briefly, liposomes composed of DOPC:DOPE:DOPS:Chol (molar ratio of 5:2:2:1) were prepared in a 150 mM KCl, 20 mM HEPES (pH 7.4) buffer by reverse-phase evaporation and subsequently by extrusion through polycarbonate membranes (pore sizes of 100 nm in diameter) using a Mini-Extruder from Avanti Polar Lipids (Alabaster, AL, USA). The lipids were purchased as lyophilized powders from Avanti Polar Lipids and used without any further purification. For protein reconstitution, the vesicles were mixed with n-OG (n-octyl-β-D-glucoside) and the ΔN-complex purified in 1% n-OG at a lipid-to-protein ratio 500:1, and dialyzed against buffer (again 150 mM KCl, 20 mM HEPES, pH 7.4) over-night at 4° C to remove excess n-OG using Slide-A-Lyzer cassettes (Thermo Fisher Scientific, Waltham, MA) with a molecular weight cutoff of 2 kDa.

4.2.3 Small-angle X-ray scattering

4.2.3.1 SAXS measurements

SAXS experiments were performed at the undulator beamline ID02 [157] at European Synchrotron Radiation Facility (ESRF) in Grenoble, France. The beamline was operated at 12.45 keV photon energy. The beam size at the sample-plane was 100×100 μm. The samples were measured at two sample-to-detector distances, 1.5 m and 5 m, to cover a q-range of approximately 0.02 to 3.37 nm^{-1} after merging the SAXS signals. The scattered X-rays were recorded by a Rayonix MX-170HSCCD pixel detector (Rayonix L.L.C., USA) with 3840×3840 pixels. The two-dimensional isotropic diffraction pattern was calibrated to the absolute scale (water reference). For the SAXS measurements, the samples were loaded into a flow-through capillary cell (1.6 mm in diameter). The sample chamber was heated to 37° C. For each measurement, 10 SAXS signals were recorded with an exposure time of 1 s, and averaged after azimuthal integration. The SAXS signals obtained at the two detector distances were then merged. For background subtraction, the matched buffer was measured separately.

4.2.3.2 SAXS analysis

For completeness and notational clarity we include a brief recapitulation of the SAXS analysis for SVs, as developed in [104, 107], and summarized also in [86]. The incident x-ray beam with wave vector $\vec{k}_i$ and wave number $|\vec{k}| = 2\pi/\lambda$ for wavelength λ is scattered from an isotropic suspension of SVs. The scattered x-rays with wave vector $\vec{k}_j$ and momentum transfer $\vec{q} = \vec{k}_j - \vec{k}_i$ are recorded on the 2d area detector. The isotropic diffraction pattern depends only on the scattering angle 2θ, or correspondingly the modulus of the momentum transfer $q = |\vec{q}| = 4\pi/\lambda \sin\theta$. The intensity for a dilute, polydisperse system of particles of radius R with the number size distribution $p(R)$ follows from an incoherent polydispersity integration, is modeled by

$$I_{mod}(q) = \Delta\rho^2 \int_0^\infty p(R) V_\mathrm{p}(R)^2 F(q,R) \mathrm{d}R \,, \tag{4.1}$$

where $\Delta\rho$ is the average electron density contrast between the solvent and the particle, $V_\mathrm{p}(R)$ is the volume of the particle. Here this volume corresponds to the total volume of the SV minus the volume of the vesicle lumen (core). The relationship between scattering curve and particle structure is contained in the form factor $F(q,R) = \langle |f(\vec{q},R)|^2 \rangle$ with the form factor amplitude $f(\vec{q},R)$ and $\langle ... \rangle$ denoting the powder average. For

$p(r)$, we used a bimodal size distribution composed of two Gaussian distributions accounting for size distribution for the SVs, as well as for larger membranous particles in the sample.

The SAXS model for SVs is schematically illustrated in Fig. 4.1. The radial electron density profile (EDP) $\rho(r)$ for the lipid bilayer is modeled by three Gaussians, which also includes contributions of transmembrane proteins and amino acid residues associated with the headgroups. Further, the proteins of the inner and outer protein shell are modeled as Gaussian chains. It is important to note that the Gaussian chains, which break the spherical symmetry, are proxies for distinct protein patches. They are characterized by an effective radius of gyration R_g and an effective copy number of protein patches N_c. The scattering length density profile of the lipid bilayer with partial and symmetrized protein contributions is accounted for

$$\rho(r) = \sum_i \rho_i \exp\left(-\frac{(r-R_i)^2}{2t_i^2}\right), \tag{4.2}$$

where R_i is the peak position, ρ_i is the amplitude and t_i, $i \in \{in, out, tail\}$ is the width, for each of the Gaussians representing the headgroups and the tail region. The thickness of the bilayer is defined as $D = \sqrt{2\pi}(t_{in} + t_{tail} + t_{out})$, where $t_{in} = t_{out}$ is chosen to describe a symmetric bilayer. In this work, the vesicle radius R is defined by the center of the bilayer, i.e. by R_{tail}, in contrast to [104], where it was defined as the outer bilayer surface $R = R_{out} + t_{out}\sqrt{2\pi}/2$. The total excess scattering length of the bilayer with respect to the aqueous buffer is β_b. The Gaussian chains are distributed randomly and without correlations forming the inner and outer protein shell with effective copy numbers N_c^{in} and N_c^{out}, respectively. They are further characterized by their radii of gyration, R_g^{in} and R_g^{out}, and by their average excess scattering length density ρ_c. The distance between the inner headgroup and the center of mass of the Gaussian chains facing the lumen is $t_{in}\sqrt{2\pi}/2 + R_g^{in}$, and the distance between the outer headgroup and the center of mass of the Gaussian chains facing outwards is $t_{out}\sqrt{2\pi}/2 + R_g^{out}$. In this way, the Gaussian chains partly overlap with the tails of the bilayer profile, but do not fully penetrate the bilayer. The combination of these results

leads to the following form factor

$$\begin{aligned} F(q,R) = \frac{1}{M^2} \times [\quad & \beta_b^2 F_b^2(q,R) \\ & + \sum_{i=in,out} N_c^i \beta_c^{i\,2} P_c^i(q) \\ & + \sum_{i=in,out} 2N_c^{i\,2} \beta_b \beta_c^i S_{b\,c}^i(q,R) \\ & + \sum_{i=in,out} N_c^i (N_c^i - 1) \beta_c^{i\,2} S_c^i(q,R) \\ & + S_c^{in\,out}(q,R) \prod_{i=in,out} N_c^i \beta_c^i \,] \,. \end{aligned} \tag{4.3}$$

The different terms are now described in the following. $M = \beta_b + N_c^{in}\beta_c^{in} + N_c^{out}\beta_c^{out}$ denotes the excess scattering length, with $\beta_c^i = \frac{4\pi}{3} {R_g^i}^3 \rho_c$ the total excess scattering length of a single Gaussian chain in the modeled protein layer and with $i = in, out$, as in all following equations. The first term contains the normalized amplitude of the self-correlation of the bilayer profile, given by

$$F_b(q,R) = \sum_{i=in,tail,out} \frac{F_{b\,i}(q,R_i)}{M_{b\,i}} + F_{lumen} \,, \tag{4.4}$$

with

$$F_{b\,i}(q,R_i) = 4\sqrt{2} t_i \rho_i \exp\left(-\frac{t_i^2 q^2}{2}\right) q^{-1} \left[t_i^2 q \cos(qR_i) + R_i \sin(qR_i)\right] , \tag{4.5}$$

and $F_{lumen} = \rho_{lumen} V (\sin qR_v - qR_v \cos(qR_v))/(qR_v)^3$ the form factor of the vesicle lumen modeled as an ideal sphere with radius $R_v = R - (t_{in} + t_{tail}/2)\sqrt{2\pi}$ and the excess scattering length density ρ_{lumen} (i.e. the density contrast to the buffer) to account for changes in density due to neurotransmitter uptake. Note that in the original model $\rho_{lumen} = 0$ [104], since in that work only inactive SVs were considered. $M_{b\,i} = \rho_i \frac{4\pi}{3}((R_i + t_i\sqrt{2\pi}/2)^3 - (R_i - t_i\sqrt{2\pi}/2)^3)$ is the excess scattering length of one peak of the bilayer profile. The second term in the form factor describes the self-correlation terms of the Gaussian chains:

$$P_c^i(q) = \frac{2[\exp(-x^i) - 1 + x^i]}{x^{i\,2}} \,, \tag{4.6}$$

with $x^i = q^2 R_g^{i\,2}$. The third term accounts for the interference cross-terms $S^{in}_{b\,c}(q,R)$ and $S^{out}_{b\,c}(q,R)$ between the bilayer and the Gaussian chains, given by

$$S^{i}_{b\,c}(q,R) = F_b(q,R)\psi^i(x^i)\frac{\sin(q[R_{tail} \mp (D/2 + R_g^i)])}{q[R_{tail} \mp (D/2 + R_g^i)]}\,, \tag{4.7}$$

where $\psi^i(x^i) = [1 - \exp(-x^i)]/x^i$ the effective form factor amplitude of the Gaussian chains. Finally, the fourth term describes the interference of chains inside and outside the bilayer

$$S^{i}_{c}(q,R) = [\psi^i(x^i)\frac{\sin(q[R_{tail} \mp (D/2 + R_g^i)])}{q[R_{tail} \mp (D/2 + R_g^i)]}]^2\,, \tag{4.8}$$

and the interference between the chains of the inner and outer shells across the bilayer is taken into account by the fifth term

$$S^{in\;out}_{c}(q,R) = \prod_{i=in,out} \psi^i(x^i)\frac{\sin(q[R_{tail} \mp (D/2 + R_g^i)])}{q[R_{tail} \mp (D/2 + R_g^i)]}\,. \tag{4.9}$$

Least-squares fit. To obtain structural parameters from SAXS data, the experimental scattering intensities $I_{\mathrm{exp}}(q_i)$ with data points $i = 1, ..., N$ recorded at q_i, were fitted by the model curve $I_{\mathrm{mod}}(q_i)$, accounting for a scaling factor and a constant background as

$$I_{\mathrm{exp}}(q) = c_1 \cdot I_{\mathrm{mod}}(q) + c_2\,. \tag{4.10}$$

The quality of the fit was monitored by the reduced χ^2-function

$$\chi^2_{\mathrm{red}} = \frac{\sum_{i=1}^{N} \frac{[I_{\mathrm{exp}}(q_i) - I_{\mathrm{tot}}(q_i)]^2}{\sigma_i^2}}{N - p - 1}\,, \tag{4.11}$$

where p is the number of free model parameters and σ_i^2 is the variance of the intensity $I_{\mathrm{exp}}(q_i)$ for a measured data point i. Nonlinear least-squares fitting was implemented using the MATLAB function *lsqnonlin* of the MATLAB R2020b Optimization Toolbox.

4.3 Results and Discussion

4.3.1 Polydispersity und Purity

Notwithstanding well established protocols and almost two decades of experience [4, 171], reproducible and contamination-free SV preparations extracted and purified from rat brain is always a primary concern. This is accentuated by the rather large quantities required for scattering experiments. More generally, at the organelle level, almost any fractionation and purification from higher animals is quite challenging. At the same time, the purity of the preparation is crucial for structural studies by ensemble techniques such as scattering or spectroscopy. In scattering, whether with light, X-rays or neutrons, large particle contaminations have particular strong weight in the signal, since the signal scales with the squared volume, i.e. R^6 for the model case of solid spheres. As a consequence, a small fraction of larger aggregates caused by contamination (aggregated or fused SVs, ruptured membrane debris, etc.), compared to the size of SVs ($R \approx 19$ nm), has a considerable impact on the scattering curve. In fact, the SAXS data measured by Castorph et al. could only be modeled by including an additional size distribution accounting for contamination [104]. Large membranous particles, i.e. contamination, were also observed by cryo-EM [104], but can of course be vetoed out in direct microscopic observations, while they remain always in the scattering volume (cuvette) of ensemble techniques. At the same time, scattering is therefore very sensitive to detect contaminations, even if orders of magnitude smaller than the main fraction. The first point of this study therefore concerned the reproducibility of our previous results measured a decade ago [104], and whether there was any improvement in the level of contaminations due to refinements of the preparation protocol. To this end, we first show and compare the SAXS data of SVs measured during this study to the SAXS data published a decade ago by Castorph et al. [104].

Fig. 4.2 presents the comparison of the SV data and the analysis of contamination. By inspection of the scattering curves shown in (a), and already before any fitting, we can directly recognize the characteristic modulations of the SAXS curve in both the old and the new data sets indicating qualitative reproducibility. At the same time small differences can be observed in the functional shape, in particular for small q, where the more shallow slope for the new SV data indicates a smaller contribution from larger aggregates, i.e. a cleaner purification. This observation is quantified by least-squares fits using the anisotropic SAXS model for both data sets. The fit of the SV data measured during this study was parameterized as follows. The amplitudes of

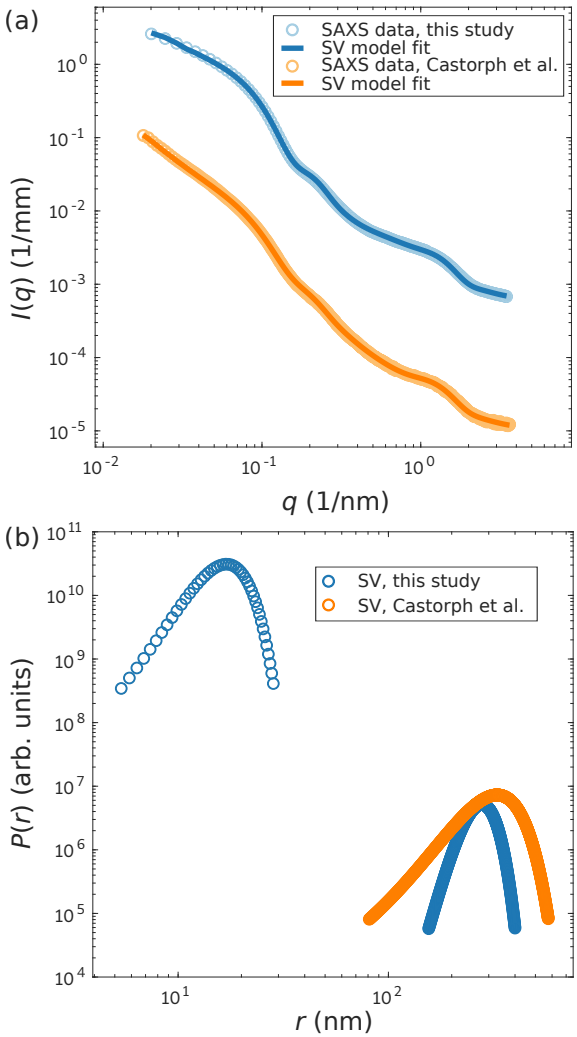

Fig. 4.2: (a) Comparison of SAXS data $I(q)$ vs. q obtained from (blue) SVs measured during this study and (orange) from SVs published a decade ago by S. Castorph et al. [104], and least-squares fits (SAXS data, this study: $\chi^2_{\text{red}} = 67.8$, and SAXS data S. Castorph et al.: $\chi^2_{\text{red}} = 4.99$). (b) Bimodal Gaussian size distributions obtained from the fits shown in (a) for SVs (this study) and SVs (S. Castorph et al.), accounting for the actual SV size distribution, and for contamination (for example, large membranous particles). The size distribution of the SV fraction was modeled as a Gaussian, fitted to the new SAXS data, and then kept constant in the fit of the Castorph et al. data. For this reason of enforced equality, (b) shows only a single color (blue) for this fraction. Contrarily, the contamination fraction was fitted freely in both datasets (see the corresponding curves in the two respective colors). The results show that the size distribution of the contamination is larger for the 'old' SV purification (S. Castorph et al.), as compared to the purification used in this study. Fitting parameters are tabulated in Tab. 4.1.

the EDP as well as the scale were kept constant, while all other parameters were free to vary. In other words, the protein and lipid headgroup and tail electron density was fixed at literature reference values (see Tab.4.1), but the protein number density and radius of gyration was free. For the least-squares fit of the SAXS data from Castorph et al. [104], the amplitudes of the EDP and the small size distribution was kept constant, but the other structural parameters could vary freely and independently. All fit results are listed in Tab. 4.1. As a result we see that the EDP and the small size distribution, i.e. the main fraction of the SVs is well reproduced, while the amplitude of the large size distribution, i.e. the contaminations, have been reduced in the new data. The resulting size distributions are plotted in Fig. 4.2(b). The large size distribution for the SAXS data from Castorph et al. shows a higher fraction as compared to the SV sample measured during this study, i.e. higher amplitude. Please also note the double-logarithmic scale and the fact that in the new data set, a suppression by four orders of magnitude is achieved for the large size fraction, underlining the quality of the preparation. Interestingly, the χ^2_{red}-values of the SAXS data from Castorph et al. is substantially lower, which may be attributed to the fact that larger polydispersity screens some of the systematic errors of the model. In other words, the discrepancy of the stil overly simplistic SV SAXS model become more apparent for the high quality preparation. Note that compared to inhouse or second generation SAXS instruments, the higher brilliance of the ID02 undulator beamline results in very small statistical errors of the SAXS data points, and hence $\chi^2 \simeq \mathcal{O}(1)$ is much more difficult to reach.

Tab. 4.1: Parameters corresponding to the least-squares fits shown in Fig. 4.2, comparing the SV fractions of this study to [104]. ρ_i is the amplitude and t_i, $i \in \{in, out, tail\}$ is the width, for each of the Gaussians representing the headgroups and the tail region. R_g^i and N_c^i, $i \in \{in, out\}$, denote the radii of gyration, and the copy numbers of the Gaussian chains, and σ_c the corresponding electron density. All (excess) densities denote the density difference to the buffer solution. The thickness of the bilayer is $D = \sqrt{2\pi}(t_{in} + t_{tail} + t_{out})$, with $t_{in} = t_{out}$, since the bilayer is assumed to be symmetric. R denotes the vesicle radius defined as the center of the bilayer. σ_R denotes the Gaussian width of the SV polydispersity, and a its amplitude. R_{large} and $\sigma_{R,large}$ denote the corresponding parameters for the contamination fraction.

Model fit parameter	SVs, this study	SVs, Castorph et al.	Unit
$\rho_{\text{in}}, \rho_{\text{out}}$	46.8	46.8	$e^-\text{nm}^{-3}$
ρ_{tail}	-28.8	-28.8	$e^-\text{nm}^{-3}$
$t_{\text{in}}, t_{\text{out}}$	1.6	1.79	nm
t_{tail}	2.33	2	nm
R_g^{in}	2.51	2.86	nm
R_g^{out}	4.38	5.3	nm
$N_c^{in}/(4\pi(R - D - R_g^{in})^2)$	0.0179	0.0084	nm^{-2}
$N_c^{out}/(4\pi(R + R_g^{in})^2)$	0.00136	0.0009	nm^{-2}
ρ_{c}	52.1	52.1	$e^-\text{nm}^{-3}$
R	16.95	16.95	nm
σ_R	3.92	3.92	nm
amplitude	248.19	248.19	arb. units
R_{large}	277.84	328.58	nm
$\sigma_{R,\text{large}}$	40.8	82.5	nm
$\text{amplitude}_{\text{large}}$	0.43	1.22	arb. unit
scale	1.0097	0.0838	-
constant background	0.00109	0.00019	1/mm

4.3.2 Structure of SVs upon glutamate uptake

Next, we have investigated the structure of SVs upon the uptake of K-glutamate. Fig. 4.3 shows the superimposed SAXS curves obtained from (blue) SVs without glutamate and ATP, (green) SVs with added glutamate but without ATP as a control experiment, and (orange) SVs with added glutamate and ATP as the uptake experiment. The curves differ in particular for low-q values, showing an increase in $I(q \to 0)$ for the uptake and the control experiment with respect to the SV reference without added metabolites. Note that in this low-q values, the ATP-driven glutamate transmembrane transport

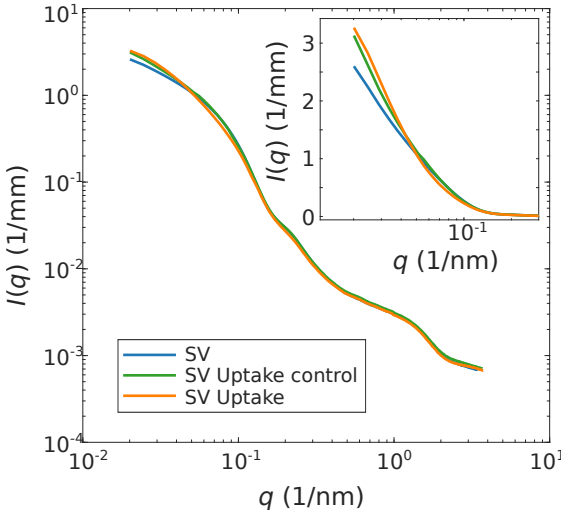

Fig. 4.3: Comparison of SAXS data $I(q)$ vs. q obtained from (blue) inactive SVs and (yellow) active SVs upon the addition of 1 mM ATP and 10 mM K-glutamate. For the control experiment, 10 mM K-glutamate, without ATP, was added to the SV suspension (green curve). The inset shows the SAXS data set for lower q-values, where main differences can be observed between the different SAXS signals.

and ATP-devoid 'control' curves both show an intensity increase with respect to the SV reference, but the effect is more pronounced for the active system than for the control. Importantly, the SAXS curve of the active system differs from the control over the entire q-range, by a significant amount, with respect to the statistical errors. The SAXS data of the uptake experiment was then fitted with the anisotropic SV-SAXS model, see Fig. 4.4. The data and the least-squares fits (solid curves) are presented in Fig. 4.4(a), shifted vertically for clarity, for (blue) SVs, (green) SV uptake control, and (orange) SV uptake. All resulting fit parameters are tabulated in Tab. 4.2. The parameters were freely and independently varied for all three cases, including the now added parameter ρ_{lumen} to

account for the uptake effect (see above). The fits resulted in satisfactory χ^2_{red}-values, of $\chi^2_{\text{red}} = 14.6, 38.4, 106.6$ for SVs, SVs uptake control, and SVs uptake, respectively. Fig. 4.4(b) shows the resulting size distributions (normalized to 1). An increase is observed in the mean radius R for the uptake experiment ($R = 18.42$ nm) compared to $R = 16.42$ nm for the inactive SVs, and the control experiment ($R = 17.56$ nm). Note that by our definition, R refers to the bilayer center, and hence is smaller by half the bilayer thickness D, when one compares to cryo-EM data such as in [104]. At the same time, the width of the size distribution shows a slight decrease both for the control and the uptake experiment. More importantly, the corresponding EDPs which are displayed in (c) for (blue) SVs, (green) SV uptake control, and (orange) SV uptake, show a significant rearrangement of protein and lipid moieties. This may be taken at an indication of significant conformational changes of SV proteins which are plausible given the high level of vesicle expansion. The increase in the thickness of the outer protein layer, the decrease in local protein density (both inner and outer layer) and the decrease in the central bilayer density are the most prominent changes in the EDP. Interestingly, the local protein density decreases (dotted lines) while the average density (dashed lines) of the inner protein shell increases. This suggests a more uniform coverage of the inner vesicle monolayer with protein moieties accompanied with the uptake and vesicle swelling. Of course, the changes in the EDPs have to be regarded with caution with respect to possible over-parameterisation. Alternative fitting strategies with fixed EDPs, hence ignoring possible rearrangements in the bilayer or protein layer, are included as supporting material. They result in substantially higher χ^2_{red}, but confirm the main finding of the SV size increase to be a robust result. Notably, the fitted values of the mean radius are very similar to the results shown in Fig. 4.4. Interestingly, the parameter ρ_{lumen} which denotes the density difference of the lumen with respect to the buffer solution, is negative in sign, but very small. This is not unlikely, since the density of glutamate solutions of molality around 0.1 mol/kg differs from water by less than 1% at 37°C [172]. Note that no literature values are available for the higher molality encountered here for SVs with estimated 8000 glutamate molecules per vesicle [13]. Finally, in order to further corroborate the robustness of the observed size increase with respect to alternative fitting strategies/models, the supporting material includes an approach where the large fraction is also freely varied as well as an isotropic fitting model composed of concentric shells.

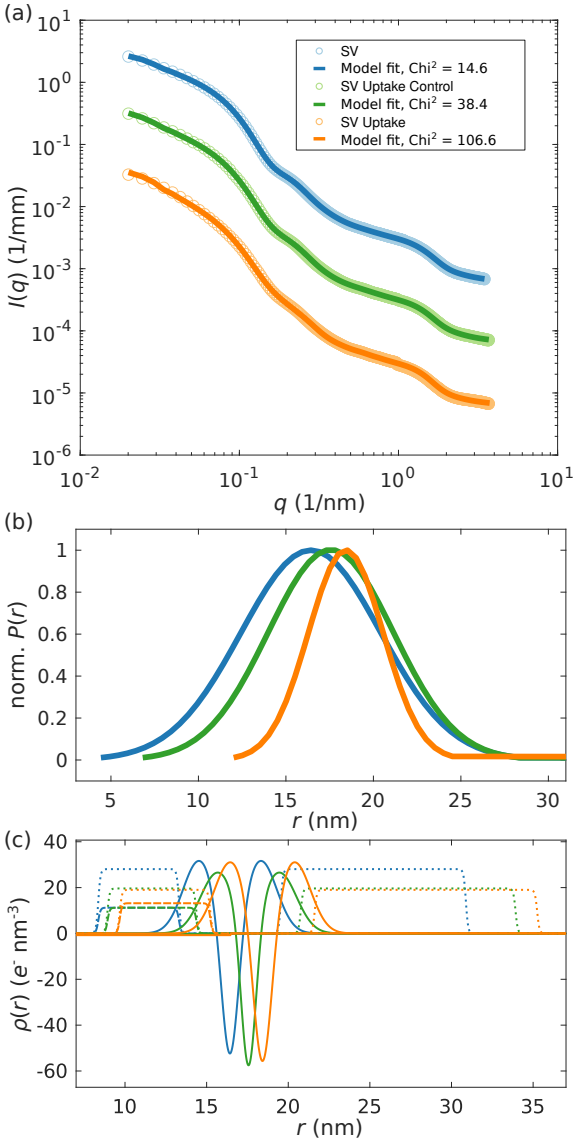

Fig. 4.4: Structural changes of SVs after neurotransmitter uptake. (a) SAXS data and anisotropic-SV model fits for SV only (blue, $\chi^2_{\text{red}} = 14.6$), SV uptake control (green, $\chi^2_{\text{red}} = 38.4$), and SV uptake (orange, $\chi^2_{\text{red}} = 106.6$). (b) Normalized Gaussian size distributions obtained from least-square fits shown in (a) with the corresponding colors. (c) Electron density profiles obtained from the least-squares fits with the corresponding colors. (Solid line) EDP of the lipid bilayer, (dotted line) Gaussian chains local, and (dashed line) Gaussian chains spherically averaged. The electron density of the inner lumen differs only slightly from zero for each EDP. For details, the fitting parameters are tabulated in Tab. 4.2.

Tab. 4.2: Parameters corresponding to the least-squares fits shown in Fig. 4.4, presenting the uptake experiments. Symbols are defined as in Tab.4.1. In addition to the parameters of Tab. 4.1, the parameter ρ_{lumen} denotes the density difference of the lumen with respect to the buffer solution.

Model fit parameter	SV	SV uptake control	SV uptake	Unit
$\rho_{\text{in}}, \rho_{\text{out}}$	31.7	26.53	31.16	$e^{-}\text{nm}^{-3}$
ρ_{tail}	-62.45	-67.92	-64.75	$e^{-}\text{nm}^{-3}$
ρ_{lumen}	-0.3	-0.2	-0.75	$e^{-}\text{nm}^{-3}$
$t_{\text{in}}, t_{\text{out}}$	2.47	2.62	2.5	nm
t_{tail}	0.65	0.58	0.7	nm
R_g^{in}	2.47	2.72	2.77	nm
R_g^{out}	5.67	6.58	6.82	nm
$N_c^{in}/(4\pi(R-D-R_g^{in})^2)$	0.032	0.038	0.044	nm^{-2}
$N_c^{out}/(4\pi(R+R_g^{in})^2)$	0.00102	0.00081	0.00107	nm^{-2}
ρ_{c}	28.06	19.63	19.02	arb. unit
R	16.42	17.56	18.42	nm
σ_R	4	3.58	2.14	nm
amplitude	35.64	35.75	35.51	arb. units
R_{large}	273.62	274.32	267.8	nm
$\sigma_{R,\text{large}}$	42	42.88	39.92	nm
$\text{amplitude}_{\text{large}}$	0.05	0.08	0.18	arb. unit
scale	10.62	10.92	5.44	-
constant background	0.0011	0.0012	0.0012	1/mm

4.3.3 Fusion of SVs with proteoliposomes

As we saw above, SAXS is well suited for structural characterization of activated SVs. Next, we consider the applications of SAXS for structural studies of SV fusion. In the synapse the fusion of neurotransmitter-filled synaptic vesicles with the presynaptic plasma membrane [4] and the subsequent release of neurotransmitters are mediated by the soluble *N*-ethylmaleimide-sensitive factor attachment protein receptors proteins (SNAREs). Neuronal SNAREs comprise both synaptobrevin 2 (Syb), situated in the membrane of the synaptic vesicle, as well as syntaxin 1a (Syx) and SNAP-25 (SN25), which are anchored in the presynaptic plasma membrane [17]. Fusion is initiated by the formation of the four-helix bundle, named the SNARE complex, which provides the driving force [17, 23, 94]. In the present *in vitro* model, SVs are incubated with proteoliposomes containing the ΔN-complex (syb2(49-96), syx1A(183-288) and SN25(1-206)). Our main questions here is to which extent this can be followed by SAXS to resolve structural details such as fusion efficiency, increase in radius of the fused vesicle, or protein re-partitioning.

Fig. 4.5 shows a set of SAXS data obtained from (blue) SVs, (red) ΔN-liposomes, (yellow) SVs mixed with ΔN-liposomes (molar ratio 1:2) as the fusion experiment, and (purple) SVs mixed with ΔN-liposomes previously incubated with syb(1-96) to block the ΔN-complex (molar ratio 1:2) as the fusion control experiment. The SAXS curve shown in green color is obtained by incoherent superposition $I(q) = (1/3I_{\mathrm{SV}}(q) + 2/3I_{\Delta\mathrm{N}}(q))/2$ of the SAXS intensity obtained from SVs and obtained from ΔN-liposomes. The prefactors of $1/3$ and $2/3$ account for the dilution of the individual contributions. The incoherent superposition represents the scattering curve expected when no reaction occurs upon mixing. Fig. 4.5(b) shows a Kratky plot $I(q) \times q^2$ vs. q of the same set of SAXS data. When comparing the fusion experiment to the control experiments, distinct differences can be observed for low-q values. In this particular region, the SAXS signal is sensitive to the vesicles size and polydispersity, so that the (raw) SAXS data does indeed give good indication of fusion. Stated differently, the hypothesis that the two populations mix without fusion can be rejected. This is of course not surprising. The more interesting question is whether we can learn about any of the structural parameters mentioned above. Unfortunately, all our efforts to fit the data to a model were not yet convincing. In brief, the data did not discriminate well enough against different scenarios. There are two main reason for this: the first is the broad polydispersity of SVs and liposomes which sort of washes out details as we saw already in the first part of this section, the second is the finite fusion efficiency which means

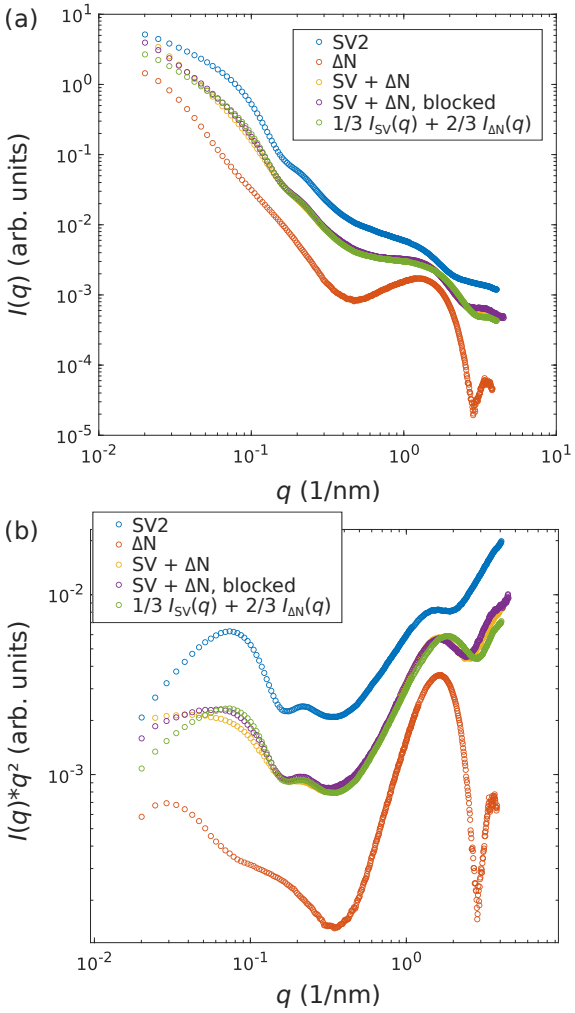

Fig. 4.5: Fusion of SVs with ΔN-liposomes. (a) $I(q)$ vs. q, and (b) Kratky plot $I(q) \times q^2$ vs. q for (blue) SVs, (red) ΔN-liposomes, (yellow) SVs mixed with ΔN-liposomes (molar ratio 1:2) as the fusion experiment, (purple) SVs mixed with ΔN-liposomes previously incubated with syb(1-96) (molar ratio 1:2) as the fusion control experiment, and (green) the incoherent superposition $I(q) = (1/3I_{SV}(q) + 2/3I_{\Delta N}(q))/2$ of the SAXS intensity obtained from SVs and obtained from ΔN-liposomes.

that fused and unfused fractions have to be modeled and superimposed. Altogether we must conclude that three populations (SVs, proteoliposomes, and contamination) are simply too many to fit the model without over-parameterisation. In the outlook below we therefore propose an entirely different approach for SV structural dynamics based on single pulse coherent diffractive imaging.

4.4 Conclusion and Outlook

As we have seen above, the increase in vesicle radius upon uptake of neurotransmitter reported in [14] can be qualitatively confirmed by SAXS. With about 8% relative increase in radius, however, the expansion was not quite as large as the maximum value observed in [14]. This may very well be attributed to the fact that the dense suspension of SVs used here may require still higher ATP concentration than 1 mmol/l. In other words, it may be possible that the uptake experiment here was ATP limited. For a free EDP fit, there is some indication of significant rearrangement in the protein layers in agreement with what one would expect from the two first models proposed in [14]. The electron density of the glutamate loaded vesicle lumen was found to be very close but slightly lower than that of pure buffer. From the simulation and dependencies of the SAXS curve on the different parameters, we can also conclude that polydispersity is the main limiting factor for SAXS analysis of SVs. This also screens details on the conformational changes in the protein shells.

In order to unlock the potential of diffraction for SV structural studies in a more complex functional context, we essentially have three different options: Firstly, improvement of purification and size fractionation: this may be difficult since we are most probably facing the intrinsic poydispersity of SVs, rather than an effect of non-ideal preparation. Secondly, we may increase data diversity by contrast variation, which is not easily possible for SAXS but which is quite straightforward for small-angle neutron scattering (SANS) based on selective deuteration. Here it would be interesting for example to measure the glutamate concentration in the vesicle lumen by variation of the contrast in this moiety (using deuterated glutamate). In fact, with regard to SAXS, the electron density of a glutamate solution does not differ sufficiently from the pure buffer solution to deduce the glutamate concentration. For fully activated SVs, we can estimate approximately 8000 glutamate molecules contained in the lumen [13], roughly corresponding to 1500 mM. With the literature values for room temperature density of glutamate solutions, this results only in a minor increase in electron density.

Note as well that even in the absence of ATP, glutamate may partition differently due to osmotic and electro-osmotic effects.

Third, and finally we may measure SVs not in a large ensemble, but in sequential high throughput mode using single particle coherent diffractive imaging (CDI) with single XFEL pulses, an approach already demonstrated for viruses [173, 174] and scalable to smaller biomolecular assemblies and macromolecules [175, 176, 177], which are delivered by aerosol electrospray methods [178]. In fact, in view of the limitations outlined above, we want to advocate single-particle CDI for the important problem of SV functional dynamics. In this way, the main limitation of conventional solution SAXS due to polydispersity and loss of information by ensemble average could be overcome in a fundamental manner. In addition, by the *diffract-before-destroy* principle we could significantly increase the signal without any risk of radiation damage.

Fig. 4.6 illustrated both the feasibility and information gain of a single-SV CDI experiment by a numerical simulation. The simulation of the diffraction pattern in (a) was performed by using the open-source software package *Condor* [179], with the simulation parameters listed in the caption of Fig. 4.6. We have used the molecular model of a SV shown in Fig. 4.1(a) for the simulations. Details on how the molecular model of a SV is built, regarding the lipid vesicle and the composition of proteins, can be found in [4]. All atom positions are converted into a PDB file, which was used as an input file for *Condor*. Fig. 4.6(b) shows the projected electron density of the SV used for the simulation, as well es the reconstruction of the real-space image from the diffraction pattern in (a). Phase reconstruction was performed by using the software package *HAWK* [180]. It can be observed, that the overall shape of the SV can be quite well reconstructed, as well as the two ATPases can be identified.

However, due to the intrinsically heterogeneous nature of SVs in view of size polydispersity and to some extent of the molecular composition, a 3D reconstruction from many diffraction patterns obtained from different orientations of the SVs will be challenging and accompanied by a loss of information on the molecular level. Therefore, in addition to phase retrieval, the anisotropic SV SAXS model can be used to analyze the data in reciprocal space by using an “in silico cleaned” monodisperse ensemble. To this end, SV diffraction patterns will be added up, following a veto-strategy to rule out images with aggregates, and radially integrated. This approach is roughly equivalent to sub-tomogram averaging in cryo-EM and will prevent loss of information by heterogeneous ensembles and thus increase structural resolution compared to conventional solution SAXS. Fig. 4.6(c) shows simulated SAXS curves using the anisotropic SV SAXS

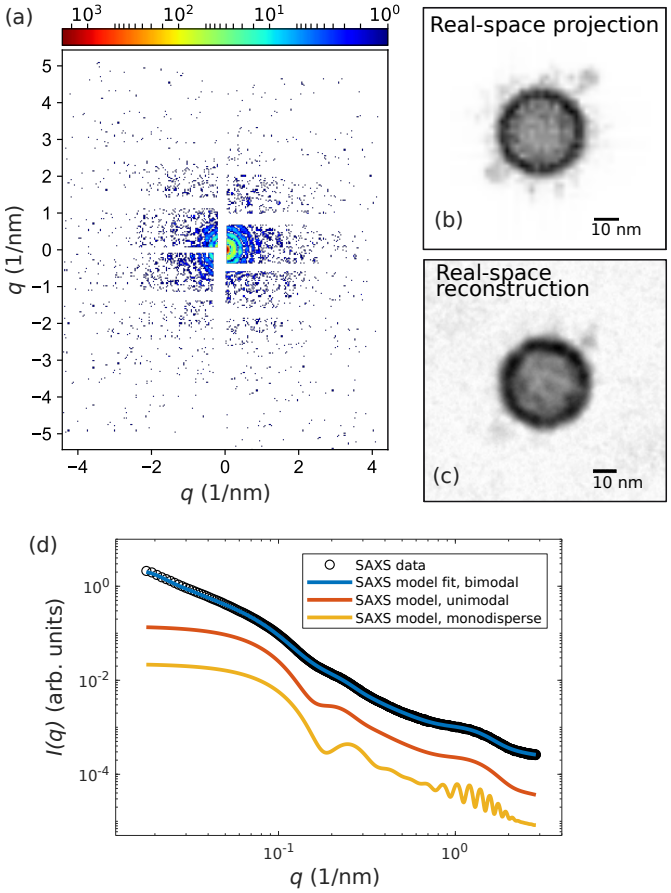

Fig. 4.6: (a-c) Simulation results of a single-SV CDI experiment and phase reconstruction using Condor and HAWK, taking the estimated Poisson noise and the detector gaps into account. (a) Simulated single-SV diffraction pattern for the orientation of the SV shown in (b) using the following simulation parameters: 6 keV photon energy, 1 mJ pulse energy, 500 nm focus, AGIPD detector geometry with 4x downsampling and 0.75 m sample-to-detector distance. (b) Projected electron density of a SV based on the molecular model in (a). Scalebar: 10 nm. (c) Reconstruction of the real space image from (a) using the difference-map algorithm with 20000 iterations, Scalebar: 10 nm. It shows that the two ATPases can be identified. (d) SAXS data [104] of a polydisperse ensemble of SVs with a model fit using a bimodal size distribution accounting for contaminations. This is compared to simulations with a unimodal size distribution of SVs and a monodisperse ensemble of SVs, as can be achieved by sub-ensemble averaging, in contrast to synchrotron SAXS.

model for (red) an unimodal size distribution (without contamination), and (yellow) an unimodal size distribution and monodisperse ensemble of SVs, which are compared to SAXS data obtained from SVs and the corresponding SAXS model fit including a bimodal size distribution. It can be clearly observed, that a bimodal size distribution in the first place, but also polydispersity of only an unimodal size distribution, washes out distinct features in the scattering curve, hence less structural information.

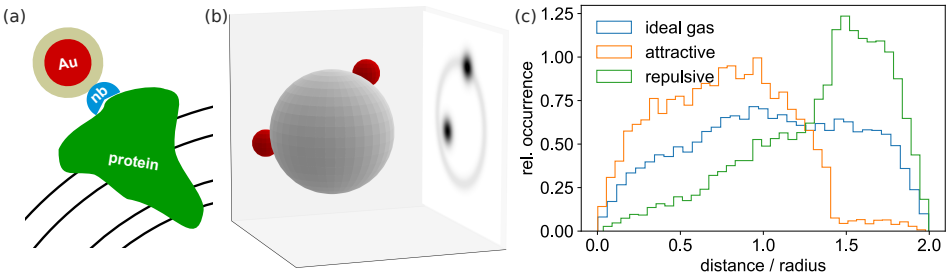

Fig. 4.7: Nanobody-nanogold labeling. (a) Sketch of the gold particle attachment principle: maleimide (brown)-coated gold 1.4 nm gold particles (red) are selectively bound to desired proteins (green) such as VGLUT1 by a nanobody (blue). Black lines illustrate the lipid bilayer. (b) Schematic of an experiment probing the distribution of gold-labeled proteins (red spheres) on the SV surface. (c) From the distance histograms of the simulated 2D projections, protein interaction potentials can be inferred. Here 19'900 pairs drawn at random with a Boltzmann weight have been evaluated, for the interaction-free case (ideal gas distribution on the sphere), as well as for attractive and repulsive potentials.

To gain information on the molecular level another promising approach is the use of nanobody-nanogold labels on specific proteins [181]. Spatial proximity of proteins on the SV surface plays a role in their concerted function. Individual large proteins or protein clusters must therefore be identified in reconstructed images of individual SVs to study functional units. To achieve this goal, individual proteins can be labeled with a specific gold-nanobody probe, as illustrated in Fig. 4.7(a). Namely, a maleimide-coated 1.4 or 5 nm gold particle is bound to a protein with a nanobody to site-selectively enhance the scattering contrast. The larger number of photons in the diffraction pattern will also help in phase retrieval and localization of the labels. In this way, we can study protein co-localization on individual SVs and unravel attractive or repulsive interaction potentials between proteins from the histogram of projected distances, see Fig. 4.7(b). Nanobodies which specifically address single synaptic proteins, such as VGLUT1, have already been successfully expressed [182]. Of course, sample delivery is also a challenge; an aerosol injection into the vacuum of the beam path has already been developed, and is compatible even with megahertz data acquisition [174] at the

European x-ray free electron laser. In this respect, we can expect a bright future for diffraction studies of functional states of synaptic vesicles and maybe even further synaptic organelles, yielding high throughput quantitative data potentially at very low sample consumption. The only bottleneck at this point is the still very limited beamtime available at the one or two instruments which are capable to provide the required beam and instrumental settings. Beamtime provided, a bright future may be ahead.

Acknowledgments

We thank Theyencheri Narayanan and Lewis Sharpnack for excellent working conditions and advice at the beamline ID02/ESRF. We acknowledge Diego Pontoni and Pierre Lloria for sharing their resources and expertise and the entire support provided in the framework of the Partnership for Soft Condensed Matter (PSCM) before and during our beamtimes at ESRF. We thank Kilian Frank and Max Scheu, for support during beamtimes, and Susanne Hengst for help in sample preparation. Further, we acknowledge ESRF for beamtime. This work was supported financially by Sonderforschungsbereich 803 "Functionality Controlled by Organization in and between Membranes", and by Sonderforschungsbereich 1286 "Quantitative Synaptology", funded by Deutsche Forschungsgemeinschaft.

Summary and Outlook

5

In this thesis, we have used X-ray diffraction, in particular synchrotron small-angle X-ray scattering, for the investigation of vesicle adhesion, fusion and neurotransmitter uptake. To this end, SAXS analysis, sample preparation protocols, as well as different experimental setups have been evaluated and optimized.

In the analysis of SAXS data, SAXS models have been adapted and extended to describe different states and forms of vesicles, including lipid vesicles, proteoliposomes and synaptic vesicles. In view of the vesicle fusion pathway, adhesion of vesicles has been induced in model systems of charged lipid vesicles by divalent salts, and the adhesion (docking) state could be clearly distinguished from other states by SAXS. The latter has proven to be a powerful technique to structurally characterize adhering vesicles, and structural details of the bilayer and the interbilayer spacing have been obtained on the sub-nanometer length scale. We have shown that the deduced interbilayer spacing can be well modeled by theoretical interaction potential models. As a main result of this thesis, the adhesion of charged vesicles induced by divalent salts with characteristic bilayer separations in the range of $d_w \approx 1 \ldots 2.4$ nm can be well predicted by evaluating the interaction forces of the electrostatic strong-coupling theory according to R. R. Netz, A. G. Moreira and coworkers. This is important, since there are very few other experimental tests of the strong-coupling theory on membranes [147]. In view of a possible relevance for biological membrane docking and fusion, we note that the water layer thickness can also be compared to the critical distance where the stalk phase appears (0.9 ± 0.05 nm), an intermediate prior to fusion [34]. It may be speculated whether calcium-induced adhesion also plays a role in the context of biological fusion, for example by lowering energy barriers. At the same time, we found that the strength of the interaction by means of the fraction of adhering membranes in the entire ensemble quantified by ν specifically depends on the type of the counterion. At constant counterion concentration, adhesion was much more favorable for Ca^{2+} than for Mg^{2+}, which possibly might play a role in the physiological scenario of calcium-dependent fusion.

Further, SAXS studies of vesicles were extended to probe transient, strongly interacting

as well as non-equilibrium states of vesicles by using time-resolved SAXS with the stopped-flow mixing technique. In this way, transient adhesion states of vesicles induced by divalent salts could be revealed prior to the transformation to a multilamellar phase in the case of high charge density. Importantly, the transient adhesion state gives important clues about the conditions of the transformation into a multilamellar state: The phase transition is preceded by a large surface area of adhesion, as inferred from the parameter ν, which likely is the main driving force of vesicle rupture and subsequent fusion. At the same time, the bilayer separation in the adhesion state remained approximately constant over time and was governed by electrostatic interactions in the strong coupling regime.

In addition to the stopped-flow mixing technique, continuous-flow mixing of vesicles and divalent ions has been studied in microfluidics devices. Comparison of the signal quality for two different beam characteristics revealed, that scanning SAXS of a microfluidic flow with a small focal spot size is feasible, however, at the cost of compromising data quality. Nevertheless, the heterogeneity of the samples in the microfluidic flow could be well characterized by scanning-SAXS, and different intermediate states upon mixing vesicles with divalent salts could be distinguished and quantitatively analyzed. Based on our experiments, there is still plenty of room for improvement and different suggestions have been made. In particular, a new design of the microfluidics device avoiding a point of stagnation would be of advantage for time-resolved measurements. Compared to established stopped-flow SAXS devices, not only the complementary accessible time scales after mixing, but also the potential reduction of sample consumption is of particular importance in view of future extensions towards microfluidics SAXS of SVs.

Finally, we have employed SAXS to study vesicles in a more physiological setting. An important goal of this work was to show that size and shape transformations of SVs in the functional context of fusion and neurotransmitter uptake can be monitored and studied by SAXS. Studies on structural changes of SVs after glutamate uptake revealed an increase in radius R of about 8% as well as indications of significant rearrangements of the membrane including membrane proteins and the lipid bilayer, and only a minor change of the inner electron density of the lumen. Such rearrangements of the membrane are likely to play an important role to account for the large extensibility of the vesicle surface in agreement with proposed models in [14]. At the same time, the polydispersity is the main limiting factor for SAXS analysis of SVs, also regarding to details of the conformational changes in the protein patches. This also explains why we could not deduce much information on the fusion experiment. The same holds

for the adhesion and fusion experiments using model proteoliposomes as discussed in Chapter 2. Whether no characteristic docking signature in the SAXS signal was observed due to low adhesion efficiency or due to loss of information in the SAXS signal by averaging over the entire population remains to be seen. Further improvement of purification and size fractionation might be helpful in particular in view of eliminating large membranous contaminations, however, at some point we are most probably facing the intrinsic polydispersity of SVs.

To overcome the main limitations of conventional solution SAXS, loss of information by ensemble average and polydispersity, we propose to employ single-particle coherent diffractive imaging (CDI) which is now possible with the availability of X-ray free electron lasers. To this end, the vesicles may be measured in a sequential high throughput mode using aerosol spray sample delivery [183, 184], an approach already demonstrated for heterogeneous organelles and viruses [185, 186, 187]. Based on numerical simulations, we have illustrated both the feasibility and information gain of a single-SV CDI experiment under realistic parameters. At the same time, such an aerosol particle injector is not limited to XFELs, and could potentially be also used in a serial synchrotron SAXS experiment, in particular in view of fourth-generation synchrotrons. Using X-ray pulses in the range of picoseconds and a focus in the sub-micron range smaller ensembles of SVs may be measured, aiming at increasing structural information by lowering the polydispersity and background scattering and potentially also at reducing sample consumption.

Appendix

A.1 Supporting Material: Vesicle adhesion and fusion studied by small-angle X-ray scattering

A.1.1 Dynamic Light Scattering

Dynamic light scattering (DLS) measurements were performed by using an ALV/-CGS-3 DLS/SLS Laser Light Scattering Goniometer System (ALV GmbH Langen, Germany). The setup is equipped with a 22 mW polarized HeNe-Laser operating at a wavelength of $\lambda = 632.8$ nm (UNIPHASE, model 1145P), and an ALV-7004 Multiple Tau Digital Correlator. Scattering intensities were recorded using an ALV high quantum efficiency avalanche diode at a scattering angle of 90°. Cylindrical borosilicate cuvettes with a diameter of 10 mm (Fisher Scientific), closed with polymer caps (Carl Roth GmbH, Karlsruhe, Germany), were used as sample cells. For matching the refractive index of the cuvettes the measurement cell in the setup was filled with toluene. In all experiments the samples were diluted $1 : 500$ with Milli-Q water, which was additionally filtered through a membrane of 20 nm pore size. For each sample, three runs of ten seconds were performed to calculate the intensity correlation functions. These correlation functions were than averaged to obtain the averaged intensity autocorrelation function $g_2(\tau) = \langle I(t)I(t+\tau)\rangle_t / \langle I\rangle_t^2$, which is related to the resulting normalized amplitude correlation function $g_1(\tau)$ by the Siegert relation $g_2(\tau) = 1 + \beta|g_1(\tau)|^2$ with the coherence factor β. Data analysis was performed with the ALV-Correlator Software (ALV-7004 for Windows, V.3.0.5.4) using a constrained regularization method for applying nonlinear fits to $\beta|g_1(\tau)|^2$. Fig. A.1 shows size distributions of vesicles obtained by DLS for different lipid compositions with respect to the preparation step. DLS measurements were performed directly after the respective preparation step involving sonication in the first step and subsequently serial extrusion through polycarbonate membranes with pore sizes of 100, 50 and 30 nm diameter, in this order. In general, we observe that the extrusion steps affect the structure of the vesicles for both parameters, the mean radius and the polydispersity of the vesicle

suspension, compared to sonicated vesicles. Both parameters are generally slightly decreased after each extrusion step. Only for DOPS huge differences can be observed for the polydispersity. Nevertheless, direct sonication of the suspension already leads to comparatively small vesicles. Note that DLS is particularly sensitive to contamination by larger aggregates, and size distribution are often 'corrected' by weighting functions, see for example [125]. Here we show only unweighted distributions.

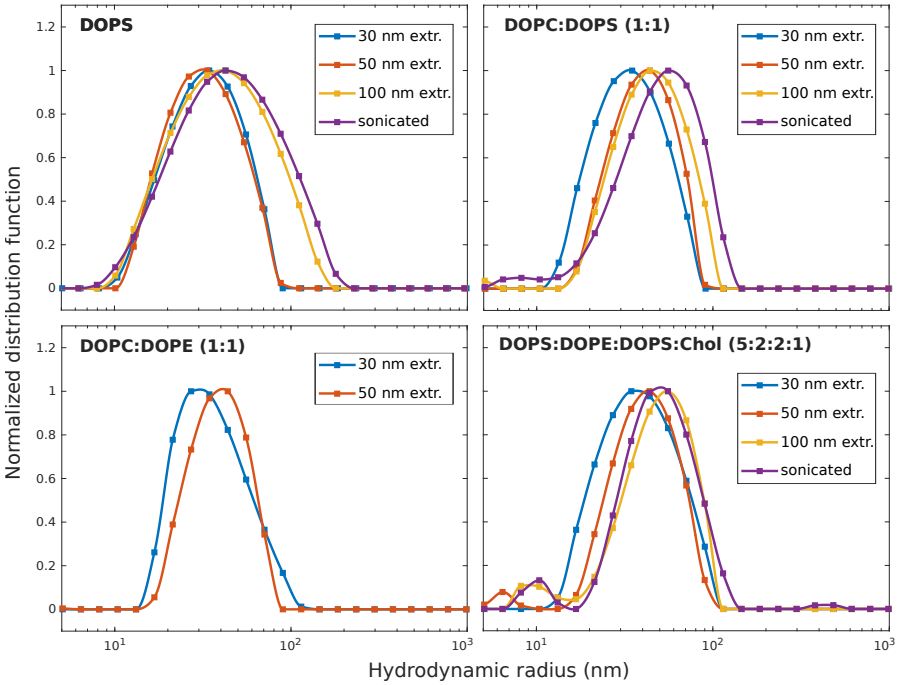

Fig. A.1: Size distributions of lipid vesicles obtained by DLS for different lipid compositions with respect to the preparation step. The vesicles were first sonicated, then extruded through polycarbonate membranes with pore sizes of 100 nm, 50 nm, and 30 nm, in this order.

A.1.2 Non-interacting vesicles: additional figures and tables

Fig. A.2 shows a series of SAXS profiles $I(q)$ vs q of vesicles in ultra-pure water for different lipid compositions. The measurements were performed immediately after the respective preparation step (subsequent extrusion through membranes of 100 nm, 50 nm and 30 nm pore size). As already discussed in the main text, we observe that vesicles containing DOPS achieve unilamellarity easily for each data set. Contrary, unilamellar vesicle using DOPC:DOPE mixtures are only achieved for DOPC:DOPE (1:1) after the final step of extrusion through 30 nm pores.

Next, we present additional fits of non-interacting vesicles without proteins, and focus in particular on the influence of different background models. Note that the workflow always included background subtraction in form of a pure buffer measurement. However, residual errors occur if this subtraction is not completely correct for example by issues of self absorption. This can be accounted for by an additional parameterized background model (additive with either sign).

Spherical vesicle model fits with different background models. Fig. A.3 shows SAXS data of (a) DOPC:DOPE (1:1)-vesicles and (b) DOPS-vesicles (black circles) as well as least-squares fits based on the spherical vesicle model (blue lines) assuming a symmetric bilayer profile. The subplots show least-squares fits for different background models: (top) Without a background model, (center) with an additional constant background model and (bottom) with an additional power-law background model (orange lines). The structural parameters and the χ^2_{red}-values obtained from the least-squares fits are summarized in Tab. A.1,A.2,A.3. If no background model was added to the spherical vesicle model, we observe discrepancies between the least-squares fits and the SAXS data in particular for the form factor minima. In the case of a constant background model, a good match can be observed for higher q-values, whereas discrepancies still appear in the lower q-region. The discrepancies are most pronounced for DOPC:DOPE vesicles. For DOPS vesicles the differences are less obvious, but at a closer look we observe modulations of the least-squares fit in the very low q-range which do not match with the experimental data. Using a power-law background model, we observe a good match between the least-squares fits and the data over the entire q-range. Consequently, the χ^2_{red}-values are reduced. The comparison of the two power-law backgrounds (Fig. A.3, bottom) indicates that the background depends on the lipid composition of the vesicles. We conclude that the background model describes discrepancies between the SAXS data and the spherical vesicle model rather than a

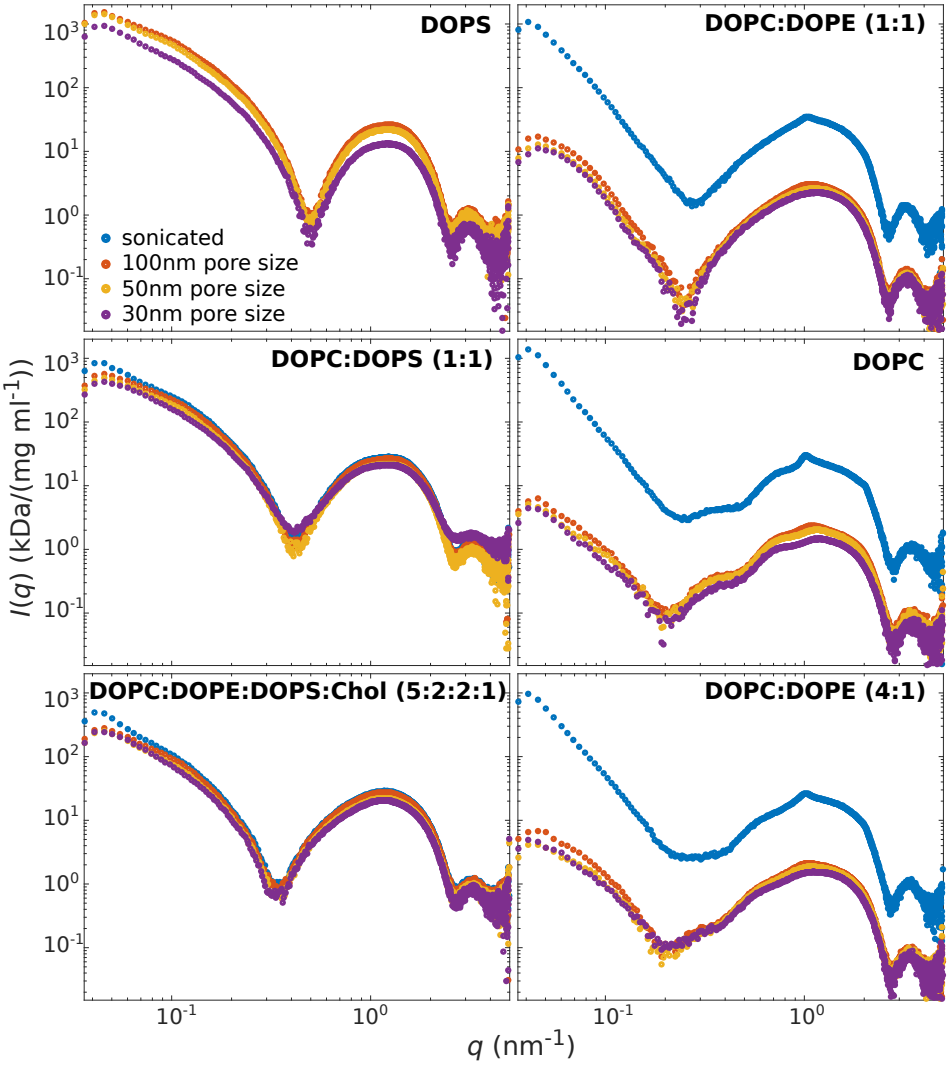

Fig. A.2: SAXS data $I(q)$ vs. q for vesicles of different composition and preparation steps in ultra-pure water. The vesicles were first sonicated (blue circles), then gradually extruded through polycarbonate membranes with pore sizes of 100 nm (red circles), 50 nm (yellow circles), 30 nm (purple circles), in this order.

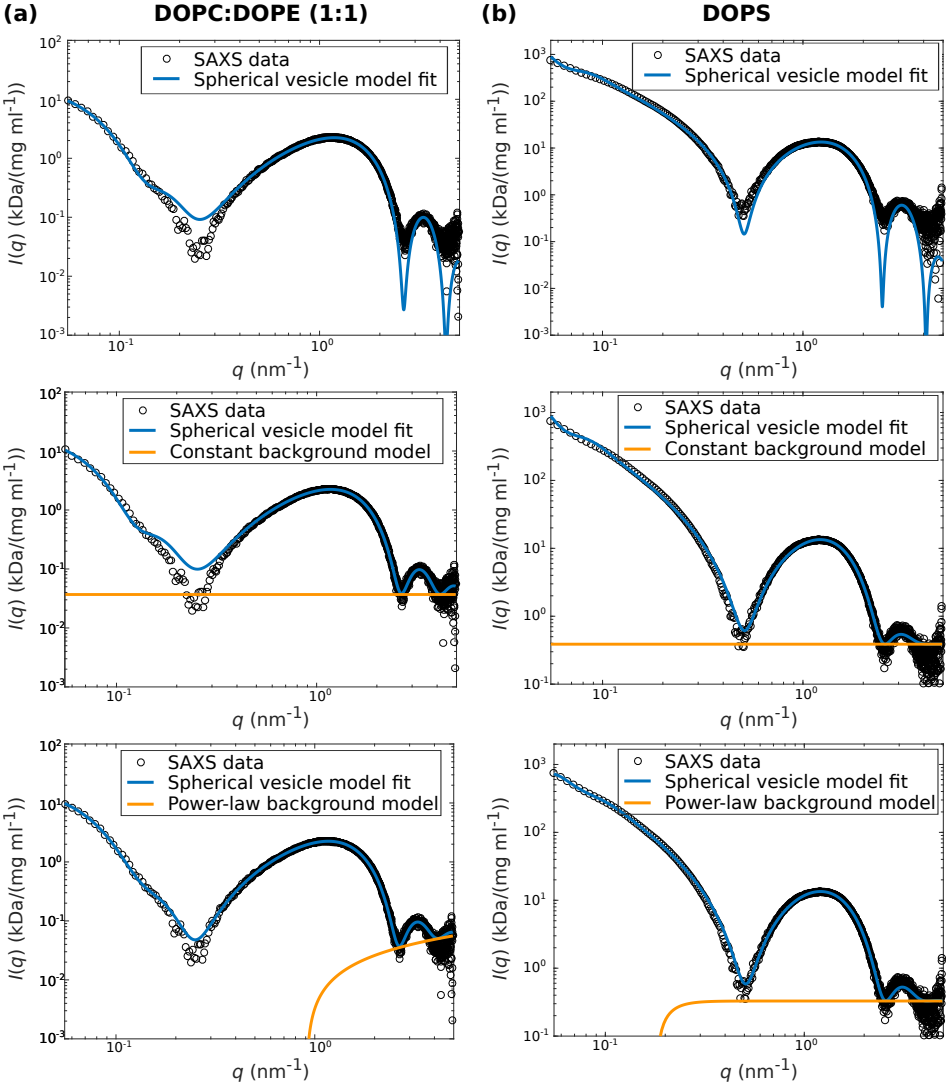

Fig. A.3: Comparison of different background models (orange lines) for (a) 30nm extruded DOPC:DOPE (1:1)-vesicles and (b) 30 nm extruded DOPS-vesicles (black circles). Analysis includes spherical vesicle model least-squares fits (blue lines) without a background model (top), with a constant background model (center) and with a power-law background model (bottom).

real effect of flawed experimental background, for example, due to deviations from a spherical structure. In the following we investigate how structural parameters depend on the background model.

Structural results for each data set, a model-based discussion. Fig. A.4 displays the structural parameters for each lipid composition along with the corresponding preparation step as obtained from the least-squares analysis using the flat bilayer model with an additional constant background (blue circles), or the spherical vesicle model with either an additional constant background (green circles) or a power-law background model (red circles). The structural parameters as well as the χ^2_{red}-values can be further found in the Tab. A.1 (flat bilayer model, constant background), A.2 (spherical vesicle model analysis, constant background) and A.3 (spherical vesicle model analysis, power-law background). The four upper plots display the obtained bilayer parameters σ_{h}, σ_{c}, ρ_{h} and d_{hh}, while the two lower plots show the vesicle parameters R_0 and σ_{R}. In the case of the spherical vesicle model analysis, we observe that the obtained structural parameters depend on the underlying background model. The dependence is less pronounced for the bilayer parameters, but strong for the mean radii. By visual inspection (cf. Fig. A.3), the spherical vesicle model with a constant background was not able to match the data in the lower q-region.

Comparing the results of the spherical vesicle model analysis to those of the flat bilayer model analysis, we observe that the structural bilayer parameters obtained from the flat bilayer model are systematically closer to those of the spherical vesicle model using an additional power-law background. This observation indicates that the results obtained from the spherical vesicle model with a power-law background are reasonable at least for the bilayer parameters. Still for the spherical vesicle model with a power-law background, major changes in the radius occur between vesicles extruded through 50 nm pore sizes and through 30 nm pore sizes. DOPC:DOPE (1:1)-vesicles are an exception, since for both preparation steps a radius of approximately 14 nm is obtained. Simultaneously, DOPC:DOPE (1:1)-vesicles show the smallest radius as compared to the other lipid compositions. One explanation for no or only minor changes in the radius between the preparation steps sonication and extrusion through pores of 50 nm diameter could be that already the sonication step leads to small mean radii. The mean radii obtained from the spherical vesicle model analysis with an additional constant background are significantly higher for each lipid composition. Unexpectedly, the mean radius shows an increase from the sonication step to the step of extrusion through 100 nm pores for DOPC:DOPS (1:1) and DOPC:DOPE:DOPS:Chol (5:2:2:1).

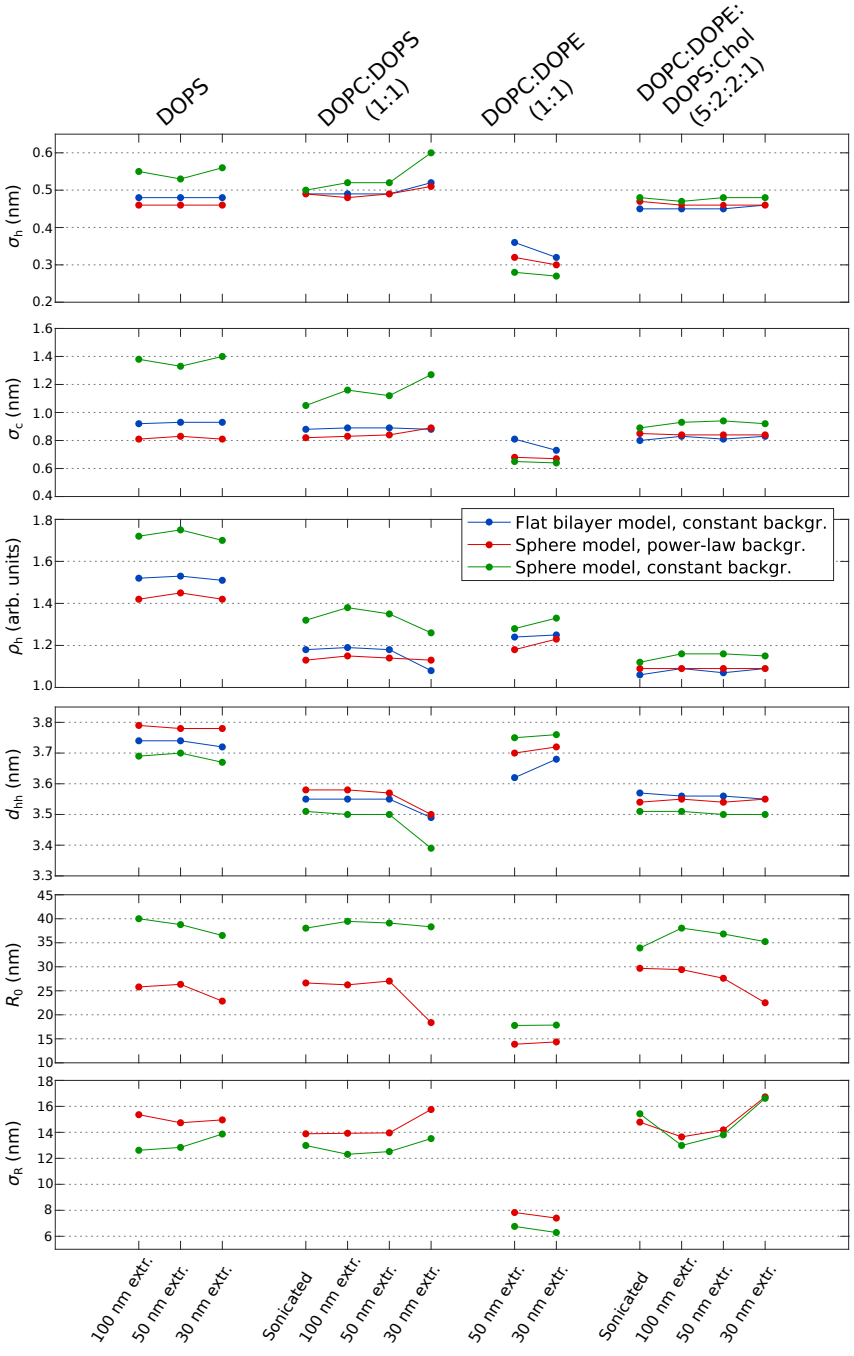

Fig. A.4: Structural parameters obtained from least-squares fits using the flat bilayer model and the spherical vesicle model with different background models for 13 data sets (four different lipid compositions and up to four different preparation steps).

Nevertheless, independently of the background model we observe the smallest radii for DOPC:DOPE (1:1) vesicles ($\sim$ 14 to 18 nm). This observation is well in line with the fact that contrary to the other lipid compositions the net charge of the mixture is zero. Thus, there is no long-range repulsion due to a negatively charged surface. The values for the standard deviation σ_{R} of the size distribution of the vesicle suspension appear to be high with respect to the corresponding mean radius (for almost each lipid composition approximately $\sigma_{\mathrm{R}}/R_0 = 0.5$). The lowest values for σ_{R} can be found for DOPC:DOPE (1:1) vesicles.

Tab. A.1: Structural parameters obtained from flat bilayer model fits to SAXS data of various lipid compositions with respect to the preparation (sonicated and extruded through polycarbonate membranes with pore sizes 100 nm, 50 nm and 30 nm in diameter). The model fits are based on a symmetric electron density profile, thus the amplitude and width of the inner and outer leaflet are $\rho_{\mathrm{h}} = \rho_{\mathrm{h1}} = \rho_{\mathrm{h2}}$ and $\sigma_{\mathrm{h}} = \sigma_{\mathrm{h1}} = \sigma_{\mathrm{h2}}$. The amplitude of the Gaussian representing the chain region is selected to $\rho_c = -1$ (arb. units) for all fits.

Lipid composition	Preparation	ρ_{h} (arb. u.)	σ_{h}, σ_{c} (nm)	d_{hh} (nm)	χ^2_{red}	c_1	c_2
DOPS	100 nm extr.	1.52	0.48, 0.92	3.74	5.19	23.34	0.64
	50 nm extr.	1.53	0.48, 0.93	3.74	3.66	19.66	0.57
	30 nm extr.	1.51	0.48, 0.93	3.72	2.30	11.92	0.35
DOPC:DOPS (1:1)	sonicated	1.18	0.49, 0.88	3.55	4.95	38.90	0.89
	100 nm extr.	1.19	0.49, 0.89	3.55	3.57	36.24	0.82
	50 nm extr.	1.18	0.49, 0.89	3.55	2.67	30.36	0.68
	30 nm extr.	1.08	0.52, 0.88	3.49	3.94	31.31	1.45
DOPC:DOPE (1:1)	50 nm extr.	1.24	0.36, 0.81	3.62	2.79	3.87	0.05
	30 nm extr.	1.26	0.32, 0.73	3.68	1.15	3.56	0.04
DOPC:DOPE:DOPS:Chol (5:2:2:1)	sonicated	1.06	0.45, 0.80	3.57	2.00	43.47	0.78
	100 nm extr.	1.09	0.45, 0.83	3.56	1.73	40.79	0.73
	50 nm extr.	1.07	0.45, 0.81	3.56	1.72	33.57	0.61
	30 nm extr.	1.09	0.46, 0.83	3.55	1.73	30.88	0.55

Tab. A.2: Structural parameters obtained from spherical vesicle model fits $I_{\text{tot}}(q) = c_1 I_{\text{sphere}}(q) + c_2 q^{-c_3} + c_4$ to SAXS data of various lipid compositions with respect to the preparation (sonicated and extruded through polycarbonate membranes with pore sizes 100 nm, 50 nm and 30 nm in diameter). The model fits are based on a symmetric electron density profile, thus the amplitude and width of the inner and outer leaflet are $\rho_{\text{h}} = \rho_{\text{h1}} = \rho_{\text{h2}}$ and $\sigma_{\text{h}} = \sigma_{\text{h1}} = \sigma_{\text{h2}}$. The amplitude of the Gaussian representing the chain region is selected to $\rho_c = -1$ (arb. units) for all fits.

Lipid composition	Preparation	ρ_{h} (arb. u.)	σ_{h}, σ_{c} (nm)	d_{hh} (nm)	R_0 (nm)	σ_R (nm)	χ^2_{red}	c_1	c_2	c_3	c_4
DOPS	100 nm extr.	1.42	0.46, 0.81	3.79	25.8	15.36	9.14	0.014	$-7.42 \cdot 10^{-6}$	6.52	0.61
	50 nm extr.	1.45	0.46, 0.83	3.78	26.34	14.74	5.92	0.011	$-2.93 \cdot 10^{-6}$	6.77	0.54
	30 nm extr.	1.42	0.47, 0.81	3.78	22.85	14.96	3.77	0.008	$-5.15 \cdot 10^{-6}$	6.42	0.33
DOPC:DOPS (1:1)	sonicated	1.13	0.49, 0.82	3.58	26.63	13.89	7.56	0.022	$-2.54 \cdot 10^{-7}$	7.43	0.86
	100 nm extr.	1.15	0.48, 0.83	3.58	26.24	13.93	5.61	0.021	$-1.36 \cdot 10^{-6}$	6.88	0.79
	50 nm extr.	1.14	0.49, 0.84	3.57	27.02	13.96	3.63	0.017	$-3.24 \cdot 10^{-7}$	7.28	0.65
	30 nm extr.	1.13	0.51, 0.89	3.5	18.38	15.76	3.79	0.026	$-2.52 \cdot 10^{-5}$	5.8	1.41
DOPC:DOPE (1:1)	50 nm extr.	1.18	0.32, 0.68	3.7	13.87	7.83	3.34	0.009	1010.85	$-3.97 \cdot 10^{-5}$	-1010.85
	30 nm extr.	1.23	0.3, 0.67	3.72	14.35	7.4	1.42	0.007	808.51	$-4.05 \cdot 10^{-5}$	-808.51
DOPC:DOPE:DOPS:Chol (5:2:2:1)	sonicated	1.09	0.47, 0.85	3.54	29.68	14.79	3.05	0.021	$-3.04 \cdot 10^{-12}$	10.77	0.76
	100 nm extr.	1.09	0.46, 0.84	3.55	29.41	13.65	2.47	0.020	$-9.71 \cdot 10^{-10}$	8.96	0.71
	50 nm extr.	1.09	0.46, 0.84	3.54	27.61	14.19	2.1	0.018	$-8.22 \cdot 10^{-10}$	8.93	0.59
	30 nm extr.	1.09	0.46, 0.84	3.55	22.51	16.73	2.08	0.019	$-1.97 \cdot 10^{-10}$	9.34	0.53

Tab. A.3: Constant Background. Structural parameters obtained from spherical vesicle model fits to SAXS data of various lipid compositions with respect to the preparation (sonicated and extruded through polycarbonate membranes with pore sizes 100 nm, 50 nm and 30 nm in diameter). The model fits are based on a symmetric electron density profile, thus the amplitude and width of the inner and outer leaflet are $\rho_h = \rho_{h1} = \rho_{h2}$ and $\sigma_h = \sigma_{h1} = \sigma_{h2}$. The amplitude of the Gaussian representing the chain region is selected to $\rho_c = -1$ (arb. units) for all fits.

Lipid composition	Preparation	ρ_h (arb. u.)	σ_h, σ_c (nm)	d_{hh} nm)	R_0 (nm)	σ_R (nm)	χ^2_{red}	c_1	c_2
DOPS	100 nm extr.	1.72	0.55, 1.38	3.69	40.01	12.62	58.38	0.004	0.39
	50 nm extr.	1.75	0.53, 1.33	3.70	38.78	12.84	34.58	0.006	0.60
	30 nm extr.	1.70	0.56, 1.40	3.67	36.52	13.87	21.58	0.007	0.71
DOPC:DOPS (1:1)	sonicated	1.32	0.50, 1.05	3.51	38.04	12.99	22.37	0.012	0.88
	100 nm extr.	1.38	0.52, 1.16	3.50	39.46	12.31	26.72	0.010	0.84
	50 nm extr.	1.35	0.52, 1.12	3.50	39.11	12.52	15.89	0.009	0.68
	30 nm extr.	1.26	0.60, 1.27	3.39	38.32	13.52	15.25	0.011	1.48
DOPC:DOPE (1:1)	50 nm extr.	1.28	0.28, 0.65	3.75	17.78	6.76	4.89	0.006	0.04
	30 nm extr.	1.33	0.27, 0.64	3.76	17.86	6.29	2.39	0.005	0.04
DOPC:DOPE:DOPS:Chol (5:2:2:1)	sonicated	1.12	0.48, 0.89	3.51	33.91	15.43	3.42	0.015	0.77
	100 nm extr.	1.16	0.47, 0.93	3.51	38.05	12.99	4.65	0.012	0.72
	50 nm extr.	1.16	0.48, 0.94	3.50	36.83	13.81	3.44	0.010	0.60
	30 nm extr.	1.15	0.48, 0.92	3.50	35.24	16.62	2.52	0.010	0.54

A.1.3 Adhesion of vesicles: additional figures and tables

Based on the analysis of the SAXS data of $CaCl_2$- and $MgCl_2$-induced adhesion of lipid vesicles presented in the main manuscript (Fig. 2.5, Tab. 2.2), we further compare the EDPs upon addition of the divalent ions and of the control (without divalent ions) in Fig. A.5. Both for $CaCl_2$ and $MgCl_2$ a swelling of the lipid bilayer is observed. Subtraction of the EDPs ($\rho_{CaCl_2} - \rho_{control}$ and $\rho_{MgCl_2} - \rho_{control}$) gives pronounced peaks close to the headgroup maxima (identified as the phosphorus), revealing the position of the condensated Ca^{2+} and Mg^{2+} ions. Accordingly, the ions are located near the bilayer surface with a rather small penetration depth into the headgroup region (the insertion is less for Ca^{2+}).

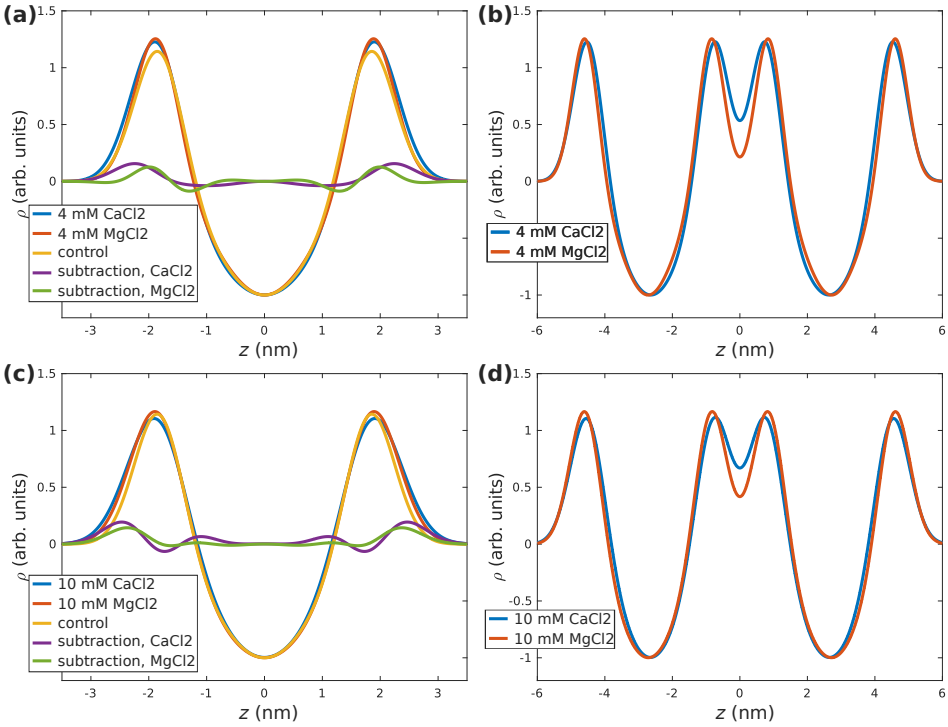

Fig. A.5: Reconstructed EDPs of DOPC:DOPS (1:1) with (a,b) 4 mM $CaCl_2$/$MgCl_2$ and (c,d) 10 mM $CaCl_2$/$MgCl_2$ using the structural parameters obtained from the flat bilayer model fits and from the docking model fits presented in the main manuscript in Fig. 2.5 and Tab. 2.2. The EDPs indicated as control correspond to the flat bilayer analysis of the SAXS data without added salts.

Next, we present data obtained in a soft adhesion regime with inter-bilayer water

distances much larger than for the strong adhesion regime described in the main manuscript. This regime is observed when the addition of $CaCl_2$ is accompanied by monovalent salt (KCl). For the recording of that data, we have used $CaCl_2$ in a HEPES buffer (10mM $CaCl_2$, 150mM KCl and 20mM Hepes, pH 7.4). Fig. A.6 shows the corresponding series of SAXS curves $I(q)$ vs. q of vesicles initially suspended in ultra-pure water, as a function of the added $CaCl_2$ and KCl concentration. The SAXS profiles of the

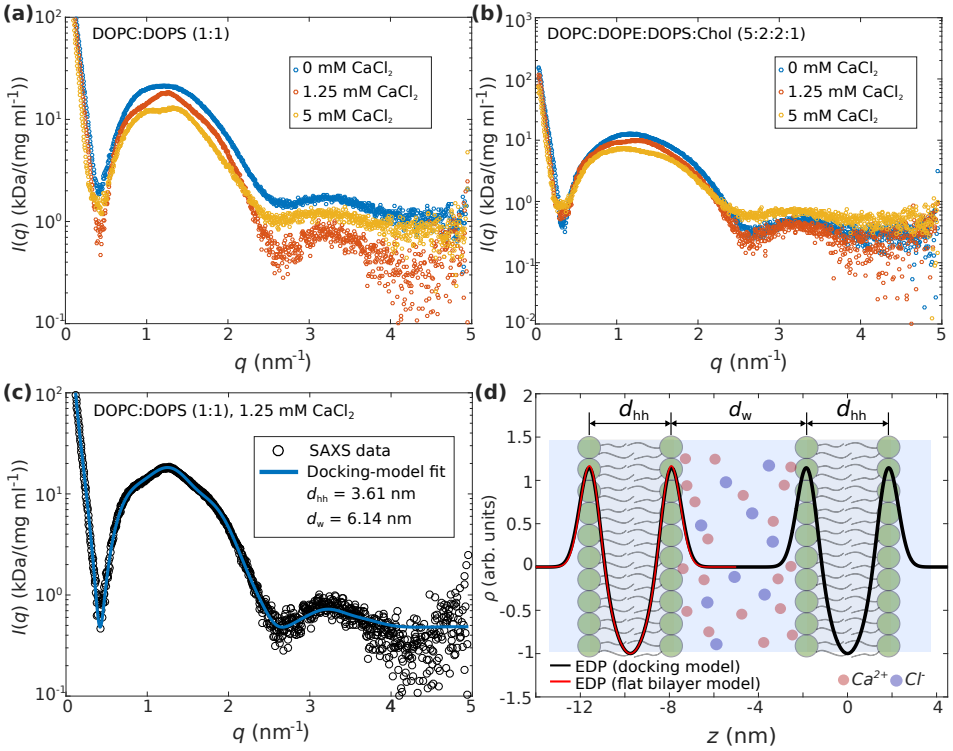

Fig. A.6: (a) SAXS data of DOPC:DOPS (1:1) vesicles in Milli-Q water with added $CaCl_2$ with concentrations of 0 mM (blue), 1.25 mM (red) and 5 mM (yellow). (b) SAXS data of DOPC:DOPE:DOPS:Chol (5:2:2:1) vesicles in Milli-Q water with added $CaCl_2$ with concentrations of 0 mM (blue), 1.25 mM (red) and 5 mM (yellow). (c) Scattering curve as obtained from DOPC:DOPS (1:1) vesicles in Milli-Q water upon addition of 1.25 mM $CaCl_2$ (black circles) and least-squares fit using the docking model (blue line). (d) EDP as obtained from the docking model fit indicated in (c). The structural parameters are summarized in Tab. A.4.

DOPC:DOPS (1:1) mixture (a) and the DOPC:DOPE:DOPS:Chol (5:2:2:1) mixture (b) show the characteristic structure factor modulations of two membranes in an adhering state. The modulation varying systematically with ion concentrations, indicating that the range of water layer spacings is much more variable than in the strong adhesion

regime. As an example, we explicitly show in (c) the analysis of the SAXS data of DOPC:DOPS (1:1) vesicles in the presence of 1.25 mM $CaCl_2$ and 18.75 mM KCl, based on the docking model with a constant background model. The structural parameters obtained from the least-squares fits to the docking model are listed in Tab. A.4 for each data set. In (d), the corresponding EDP of the two docked bilayers is displayed (black line). Next to the structural bilayer parameters, the interbilayer spacing (or water spacing) is quantified in a robust manner, yielding $d_w = 6.14$ nm. Furthermore, the EDP of unilamellar DOPC:DOPS (1:1) vesicles as obtained from the flat bilayer model fit is indicated (red line). In this example, the bilayer structure exhibits only minor changes due to the addition of $CaCl_2$. As is apparent from Tab. A.4, the water spacing is decreased for an increased $CaCl_2$ concentration ($d_w = 3.79$ nm in the case of 5 mM $CaCl_2$). For the more complex lipid mixture of DOPC:DOPE:DOPS:Chol (5:2:2:1), a similar trend can be observed. While the water spacing of $d_w = 5.48$ nm is again rather high for 1.25 mM $CaCl_2$, a decreased water spacing of $d_w = 3.03$ was obtained for 5 mM $CaCl_2$. Interestingly, comparing the values for d_w between the different lipid compositions at the same $CaCl_2$ concentration, we can see that the water spacing is always smaller for DOPC:DOPE:DOPS:Chol (5:2:2:1). This observation may result from the lower surface charge density σ in the 4-component mixture (20 mol% DOPS).

In summary, we observe the following: (1) An increase of the $CaCl_2$ and KCl concentration yields a decrease of the interbilayer spacing d_w and (2) an increase of σ at constant ion concentrations yields an increase of d_w.

Tab. A.4: Structural parameters as obtained from docking model fits to SAXS data of docked DOPC:DOPS (1:1) and DOPC:DOPE:DOPS:Chol (5:2:2:1) vesicles with respect to the $CaCl_2$ concentration. The model fits are based on a symmetric EDP, thus the amplitude and width of the inner and outer leaflet are $\rho_h = \rho_{h1} = \rho_{h2}$ and $\sigma_h = \sigma_{h1} = \sigma_{h2}$. The amplitude of the Gaussian representing the chain region is selected to $\rho_c = -1$ for all fits.

Lipid composition	$[CaCl_2]$ (mM)	[KCl] (mM)	ρ_h (a. u.)	σ_h, σ_c (nm)	d_{hh} (nm)	d_w (nm)	$(1-\nu_d)$	χ^2_{red}
DOPC:DOPS (1:1)	1.25	18.75	1.27	0.46, 089	3.61	6.14	0.96	1.7
	5	75	1.32	0.38, 0.75	3.79	4.82	0.97	2.2
DOPC:DOPE:DOPS:Chol (5:2:2:1)	1.25	18.75	1.09	0.46, 0.85	3.6	5.48	0.98	2.26
	5	75	1.02	0.47, 0.83	3.58	3.69	0.97	1.39

A.1.4 SNARE-mediated liposome fusion and docking experiments

To study SNARE-mediated liposome fusion intermediates, two types of experiments were performed. For the docking and fusion experiments liposomes reconstituted with either the mutant SybΔ84, or with SybWT, respectively, were used. For both experiments liposomes reconstituted with the ΔN complex as the acceptor complex were used. Fusion is distinctly inhibited by using the SybΔ84 mutant [23].

In Fig. A.7 (a) and (b) the SAXS curves $I(q)$ vs. q are shown for the fusion experiment (mixed SybWT- and ΔN-liposomes at a molar ratio of 1:1) and the docking experiments (mixed SybΔ84- and ΔN-liposomes at a molar ratio of 1:1), respectively. Furthermore, the SAXS data of the docking and fusion experiments are compared to the mean scattering of the individual SNARE-liposomes. The mean scattering curve would be the expected scattering curve if no reaction occurred upon mixing. Then the scattering intensity is the incoherent superposition $I(q) = (I_A(q) + I_B(q))/2$ of the two individual contributions. The factor $1/2$ accounts for the dilution of each individual SNARE-liposome population. By comparison of the mean scattering curves and the scattering curves from the docking and fusion experiments, we observe small but systematic differences in the low q-region, and a slight increase of the scattering intensity over the entire q-region.

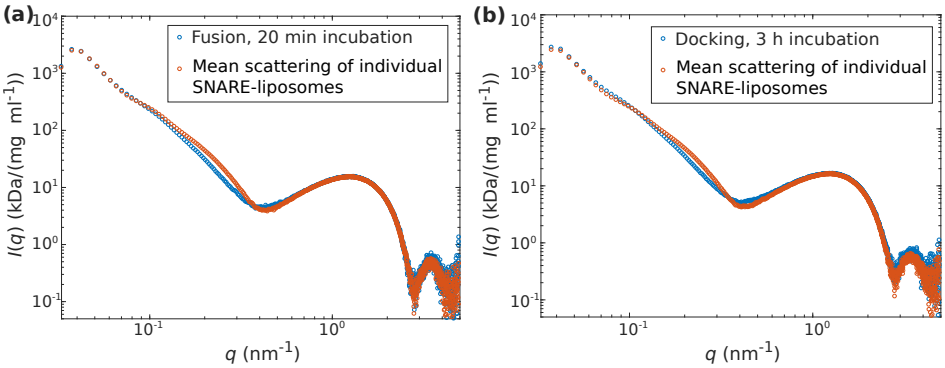

Fig. A.7: (a) and (b) show SAXS data of SNARE-mediated fusion (mixed SybWT- and ΔN-liposomes) and docking (mixed SybΔ84- and ΔN-liposomes) experiments compared to the calculated mean scattering curves $(I_{\mathrm{SybWT}}(q) + I_{\Delta\mathrm{N}}(q))/2$ in the case of the fusion experiments and $(I_{\mathrm{Syb\Delta84}}(q) + I_{\Delta\mathrm{N}}(q))/2$ in the case of the docking experiment

In the case of the docking experiments, the characteristic structure factor modulations observed in the calcium-induced vesicle adhesion are not observed. Therefore, it is

not possible to analyze the SAXS data by least-squares fits using the docking model to obtain the water spacing d_w. We conclude that the signal of the docking and fusion states may have been lost in the ensemble average of the SAXS experiment, i.e. that docking and fusion efficiencies have been insufficient. This conclusion is supported by the following estimate of the increase of the forward scattering intensity, made for the case of 100 % fusion efficiency, we consider a form factor model of a spherical shell. The scattering intensity $I_{\text{shell}}(q)$ is given by [188]

$$\begin{aligned} I_{shell}(q) &= \Delta\rho^2 V_{\text{shell}}^2 |f_{\text{shell}}(q)|^2 \\ &= \Delta\rho^2 V_{\text{shell}}^2 \left| \frac{V(R_{\text{out}}) f_{\text{sphere}}(q, R_{\text{out}}) - V(R_{\text{in}}) f_{\text{sphere}}(q, R_{\text{in}})}{V(R_{\text{out}}) - V(R_{\text{in}})} \right|^2 , \end{aligned} \tag{A.1}$$

where

$$f_{\text{sphere}}(q, R) = \frac{3(\sin(qR) - qR\cos(qR))}{(qR)^3} \tag{A.2}$$

is the form factor of a homogeneous sphere, $V(R) = 4/3\pi R^3$ is the volume of a sphere with the radius R, and $V_{\text{shell}} = 4/3\pi(R_{\text{out}}^3 - R_{\text{in}}^3)$ is the volume of the shell with the outer and inner radius R_{out} and R_{in}, respectively. For the forward scattering intensity $q \to 0$ the form factor of the spherical shell becomes $f_{\text{shell}} \approx 1$, so that

$$I_{\text{shell}}(0) \propto V_{\text{shell}}^2 \propto \left(R_{\text{out}}^3 - R_{\text{in}}^3\right)^2 . \tag{A.3}$$

For example, if we consider an outer radius of $R_{\text{out}} = 40$ nm and an inner radius $R_{\text{in}} = 35$ nm in the original state, then the radii of fused spherical shells are approximately $R_{\text{out}} = 50$ nm and $R_{\text{in}} = 45$ nm by assuming that the volume of the two spherical shells remain after fusion, that means $V_{\text{fused}} = 2V$ and thus $R_{\text{fused}} = 2^{1/3}R$. This assumption yields an increase of $\sim 56\%$ of the forward scattering intensity, which is far away from the experimental observations. Altogether, the results indicate that some reactions occurred, but we can not clearly distinguish between a docked and a fused state, most likely, due to a very low efficiency of the reactions.

A.2 Supplementary information: Vesicle adhesion in the strong coupling regime studied by time-resolved small-angle X-ray scattering

As supplemental figures, we include a plot of the bilayer structure parameters, obtained from the least-squares analysis of the stopped flow reaction as a function of time, see Fig. A.8, as well as additional SAXS data on vesicle reactions upon injection of trivalent salts, recorded in the flow-through capillary at ID02/ESRF, see Fig. A.9. Finally, as a first test we include a comparison of the SAXS curve as recorded in the flow-through capillary chamber, similar to our previous work in [107], and the SAXS curve as recorded from a SV solution in a microfluidics device (P10/PETRAIII), see Fig. A.10. As the comparison shows, the accessible q-range has to be extended by different improvements in background reduction.

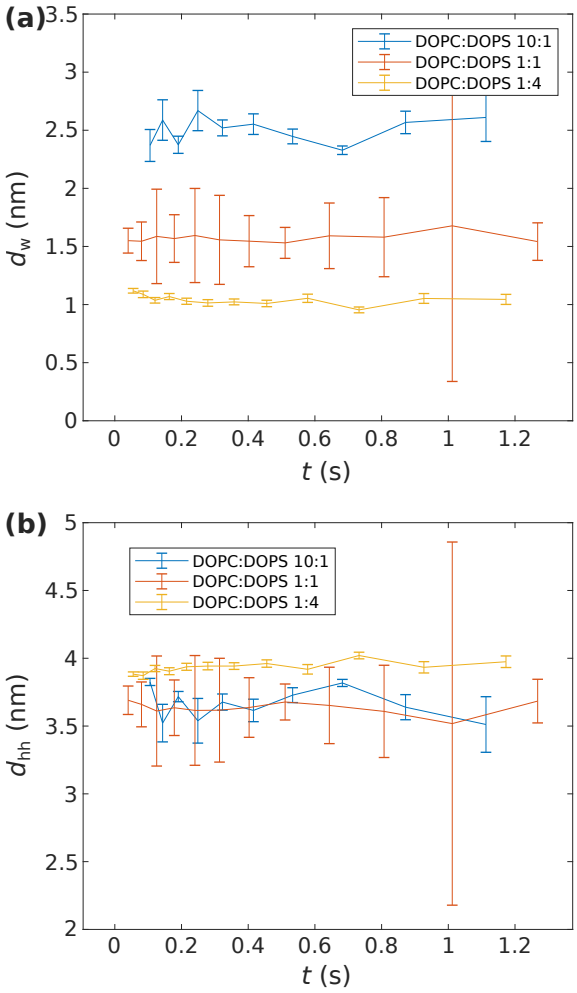

Fig. A.8: Structural parameters (a) d_w and (b) d_{hh} as a function of time as obtained from docking model fits to SAXS data measured by the stopped-flow technique.

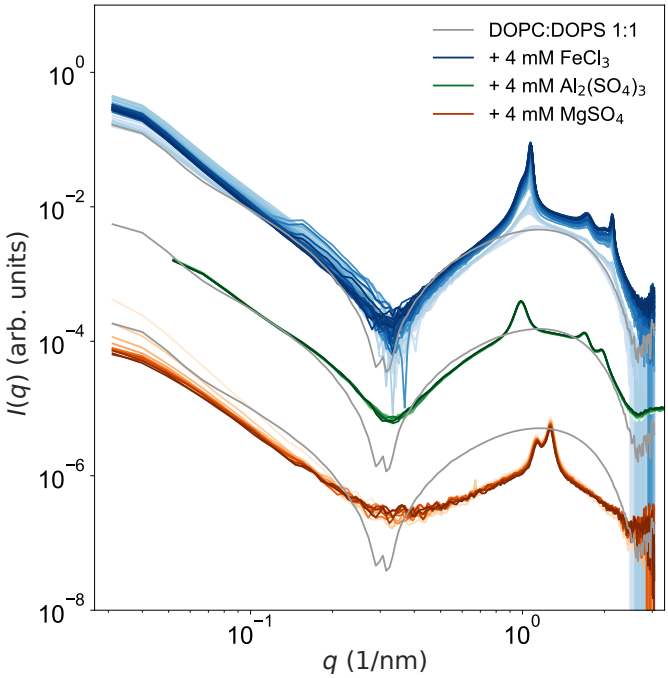

Fig. A.9: Additional flow-through SAXS data measured at ID02/ESRF using trivalent salts. SAXS curves $I(q)$ vs. q from DOPC:DOPS (1:1) vesicles mixed with 4 mM $FeCl_3$ (blue), 4 mM $Al_2(S0_4)_3$ (green), and 4 mM $MgSO_4$ are shown. No signature attributed to docking of vesicles can be observed, instead, phase transitions to multilamellar states can be inferred from the Bragg peaks.

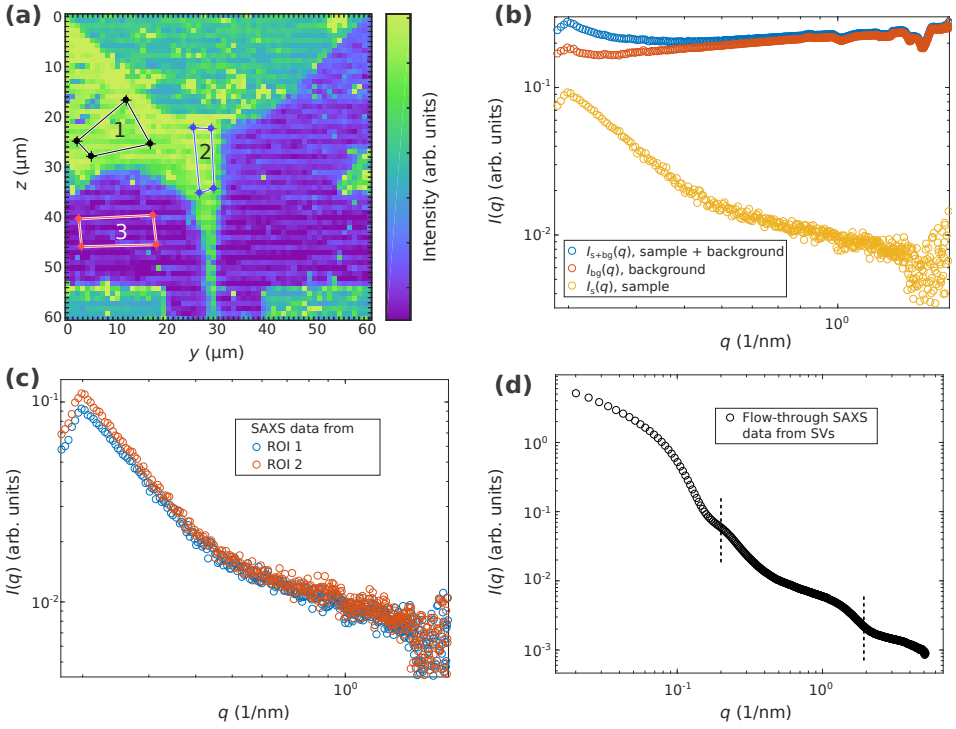

Fig. A.10: Scanning-SAXS combined with microfluidics for the investigation of the reaction of synaptic vesicles in buffer (150 mM KCl, 20 mM HEPES, pH 7.4) with 2 mM $CaCl_2$ in a microfluidic flow. The purification of synaptic vesicles was described in [171, 4]. (a) Darkfield of the microfluidics device obtained by scanning-SAXS. The exposure time was 1 s for each pixel. The SAXS data within the marked areas (black: SVs from the inlet, blue: SVs mixed with $CaCl_2$ from the point of stagnation, and red: buffer from the side-inlet) were averaged to obtain a stronger SAXS signal. (b) Example of a background corrected SAXS signal $I(q) = I_{s+bg}(q) - I_{bg}(q)$. Here, the averaged SAXS data from the inlet was used, and background corrected by the averaged SAXS data from the buffer. (c) Comparison of SVs in the inlet and of SVs in the point of stagnation (averaged SAXS signals from ROI 1 and ROI 2 in (a)). (d) For comparison, flow-through SAXS data (obtained at ID02/ESRF) is shown, covering a much larger q-space. The two vertical lines indicate the measured q-region by microfluidics SAXS shown in (a-c).

A.3 Neurotransmitter uptake and fusion of synaptic vesicles studied by X-ray diffraction: Supplemental Material

A.3.1 Supplementary data: dynamic light scattering (DLS)

For comparison with SAXS results, and as a more accessible instrument to many research teams, dynamic light scattering (DLS) was used to measure the hydrodynamic radius of synaptic vesicles after neurotransmitter uptake. The preparation of the samples was performed directly before the measurement. SVs were stored at −80° C and had to be thawed on ice for about 15 minutes before the samples were prepared. During a measurement the remaining SVs and chemicals were kept on ice. The SVs were diluted to the desired concentration (here concentrations between 1:125 and 1:2000 were used) in an uptake buffer containing 300 mM Glycine, 5 mM HEPES, 10 mM KCl and 2 mM $MgSO_4 \times 3H_2O$ in MilliQ. The pH was set to 7.3. Before dilution the uptake buffer was sterile filtered with 0.2 μm syringe filters (Whatman FP30/0.2 CA-S,UK). For the control measurement 10m M K-glutamate was added, for the uptake experiment 10 mM K-glutamate and 4 mM MgATP. For the measurement 500 μl of the sample solution was filled into thoroughly cleaned cylindrical borosilicate cuvettes with a diameter of 5 mm (ROTILABO®, Roth, Germany) and sealed with a cap.

DLS measurements were performed using an ALV/CGS-3 Laser light scattering goniometer system (ALV GmbH, Langen, Germany) equipped with a 22 mW HeNe-Laser ($\lambda = 632.8$ nm, UNIPHASE, model 1145P) and an ALV/LSE-5004 multiple tau correlator. The sample was placed into a heated (37° C) toluene bath. The sample was kept in this bath approximately 15 minutes before the measurement was started, allowing for thermal equilibration and settling of eventual dust particles. The scattered light intensity was recorded by an avalanche photo diode at a scattering angle of 90° to the incident beam. Each sample was measured for 6 runs of 30 s and an average intensity correlation curve ($g_2(\tau) - 1$) was automatically calculated by the autocorrelator system. An example for such curves is shown in Fig. A.11(a). Based on the relationship

$$g_2(\tau) - 1 = \beta \left| \int_0^\infty p(R_h) \exp(-q^2 D(R_h)\tau)\, dR \right|^2$$

with coherence/ contrast parameter β, momentum transfer vector q, diffusion constant

D and decay time τ, the distribution function of the hydrodynamic radius $p(R_h)$ can be obtained. Here, this was implemented based on an inverse Laplace transformation of the autocorrelation data, using the CONTIN algorithm as provided by the ALV-software [189]. The radius distribution was weighted by $1/R^6$.

The results are summarized in Fig. A.11. (a) Shows the intensity correlation function $(g_2(\tau) - 1)$ for the SV-measurement (SV) as well as the control experiment (SV+Glut) and the uptake experiment (SV+Glut+ATP) for a vesicle concentration of 1:1500. While the correlation curves of the SV and control measurement differ only by a small shift to higher τ, the correlation curve of the uptake experiment exhibits a large shift, i.e. indicating a much higher relaxation time. In (b) the size distribution (weighted hydrodynamic radius) extracted from the measurements in (a) is shown. The radii of the SV measurement and the control measurement are almost identical. Contrarily, the hydrodynamic radius of the uptake experiment ($R_{h,uptake} = 65.5\,nm$) is much larger. Similar observations (radius of the uptake experiment substantially larger) were made for all SV concentrations. However, the exact values for the radii differ substantially, without obvious correlation to the vesicle concentration. This can be concluded from a series of DLS measurements at different concentrations, see Fig. A.11(c), where the mean of the radius distribution for each measurement is indicated by an individual symbol and the median of these is indicated by a line. For concentrations of 1:500 and 1:1000 two samples were measured. The median of the hydrodynamic radii of the SV measurements ($\bar{R}_{h,SV} = 20.56\,nm$) and the control measurements ($\bar{R}_{h,SV+Glut} = 22.2\,nm$) differ by about 1.6 nm, which represents a similar increase as deduced from SAXS. Note that the definition of the radius in the SAXS model refers to the bilayer center, and the (outer radius), which should be associated with the hydrodynamic radius, must be correspondingly larger, by at least half the thickness of the lipid chain region plus the headgroup thickness. Therefore, the SAXS and the DLS results for the mean SV radius are in good agreement. The DLS results are also in good agreement with earlier studies [125]. The results for the uptake experiment, however, are puzzling. The apparent radius ($\bar{R}_{h,uptake} = 51.25\,nm$) is twice as large after uptake than before. This unrealistically large size increase must be certainly regarded as an artifact. It could possibly be a result of aggregation, or additional relaxation times associated with other dominating modes of the active vesicle. In view of vesicle size and vesicle concentration in the sample, a clustering of vesicles, resulting in slowing down, an apparent increase of vesicle size seems unlikely, but the relaxation times are certainly due to a similar indirect effect, not to single vesicle diffusion. This underlines the necessity to probe the structural effects by a structural probe such as diffraction or

imaging, rather than indirectly via dynamics.

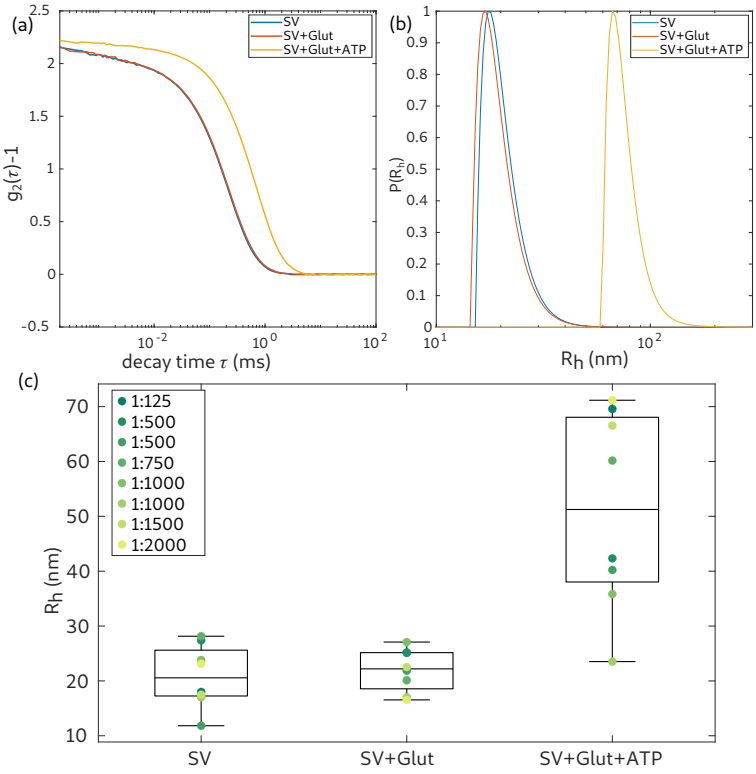

Fig. A.11: (a) Intensity correlation curves for the SV, SV control (SV+Glut) and SV uptake (SV+Glut+ATP) measurement using DLS. The vesicle concentration was 1:1500. (b) Hydrodynamic radius distribution obtained from the correlation curves in (a). The radii are weighted by $1/R_h^6$ and are normalized to a maximum value of 1. (c) Distribution of the hydrodynamic radii for different vesicle concentrations. The median of the distributions is indicated by a line. For vesicle concentrations of 1:500 and 1:1000 two individual samples were measured, which are individually plotted in the graph.

A.3.2 Supplementary SAXS data analysis: alternative fitting strategy

Fig. A.12 and Tab. A.5 present results of an alternative fitting strategy, where the electron density of the EDP components, namely protein, lipid headgroup, and lipid tail were kept fixed, while bilayer thickness, protein number density and radius of gyration, and both size distributions were freely varied for the SV reference. Next, for the SV uptake control and SV uptake data, only the size distribution of the small fraction was free, and all other parameters were kept fixed. No density contrast of the lumen was taken into account, i.e. $\rho_{\text{lumen}} = 0$. This setting was tested to rule out that the observed size increase is simply an artifact resulting from over-parameterisation. The fits show that the data can still fairly well be modeled by only the size increase, as the dominant effect causing the changes in the SAXS signal, see Fig. A.12. However, χ^2_{red}-values are much higher than in the freely varied case, indicating that the changes in the EDP are also significant.

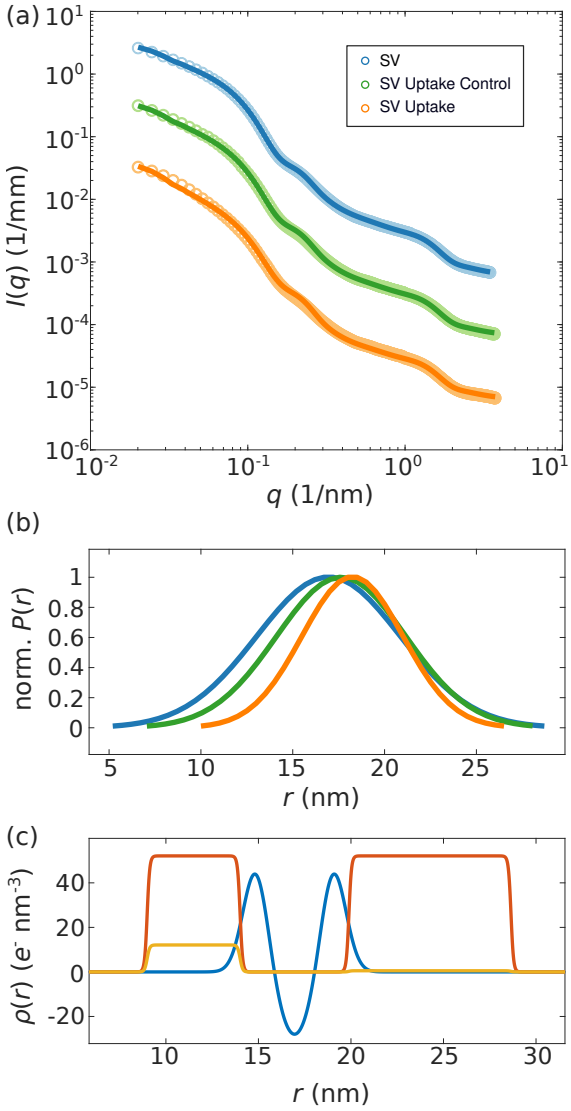

Fig. A.12: Structural changes of SVs after neurotransmitter uptake. (a) SAXS data and anisotropic-SV model fits for SV (blue, $\chi^2_{\text{red}} = 68.8$), SV uptake control (green, $\chi^2_{\text{red}} = 277.6$), and SV uptake (orange, $\chi^2_{\text{red}} = 770.3$). (b) Normalized Gaussian size distributions obtained from least-square fits shown in (a) with the corresponding colors. The size distribution of large particles was kept constant for each fit. (c) Electron density profile (EDP) obtained from the least-squares fit of SVs only. The structural parameters of the EDP were kept constant for the fits of SV uptake control and SV uptake. The EDP of the lipid bilayer is shown in blue, the Gaussian chains *local* in red and the Gaussian chains *averaged* in yellow.

Tab. A.5: Parameters corresponding to the least-squares fits shown in Fig. A.12, presenting an alternative fitting stategy of the uptake experiments, with fixed EDP.

Model fit parameter	SV	SV uptake control	SV uptake	Unit
$\rho_{\text{in}}, \rho_{\text{out}}$	46.8	46.8	46.8	$e^{-}\text{nm}^{-3}$
ρ_{tail}	-28.8	-28.8	-28.8	$e^{-}\text{nm}^{-3}$
$\sigma_{\text{in}}, \sigma_{\text{out}}$	0.68	0.68	0.68	nm
σ_{tail}	0.99	0.99	0.99	nm
R_g^{in}	2.51	2.51	2.51	nm
R_g^{out}	4.38	4.38	4.38	nm
$N_c^{in}/(4\pi(R-D-R_g^{in})^2)$	0.0179	0.0179	0.0179	nm^{-2}
$N_c^{out}/(4\pi(R+R_g^{in})^2)$	0.00136	0.00136	0.00136	nm^{-2}
ρ_{c}	52.1	52.1	52.1	$e^{-}\text{nm}^{-3}$
R	16.95	17.64	18.25	nm
σ_R	3.92	3.53	2.75	nm
amplitude	248.19	156.52	85.44	arb. units
R_{large}	277.84	277.84	277.84	nm
$\sigma_{R,\text{large}}$	40.8	40.8	40.8	nm
$\text{amplitude}_{\text{large}}$	0.43	0.43	0.43	arb. unit
scale	1.0097	1.3379	1.6731	-
constant background	0.00109	0.00121	0.00117	1/mm

Fig. A.13 and Tab. A.6 present a further validation, carried out to test a setting were at first only the large size distribution is varied (a,b). Indeed, the corresponding fits show higher χ^2_{red}-values, compared to the case where only the small fraction can change. Interestingly, the uptake control and uptake curves show an increase in the amplitude of the large fraction, which may partially be explained by the fact that larger aggregation now 'substitutes' the size increase. Finally, when reopening the degrees of freedom for the small fraction of the size distribution (after adjusting the large fraction), the χ^2_{red}-values decrease again (c,d). The corresponding model and fit parameters of these tests are tabulated in Tab.A.6 and Tab.A.7. Altogether these tests corroborate the findings of increased radius R after uptake.

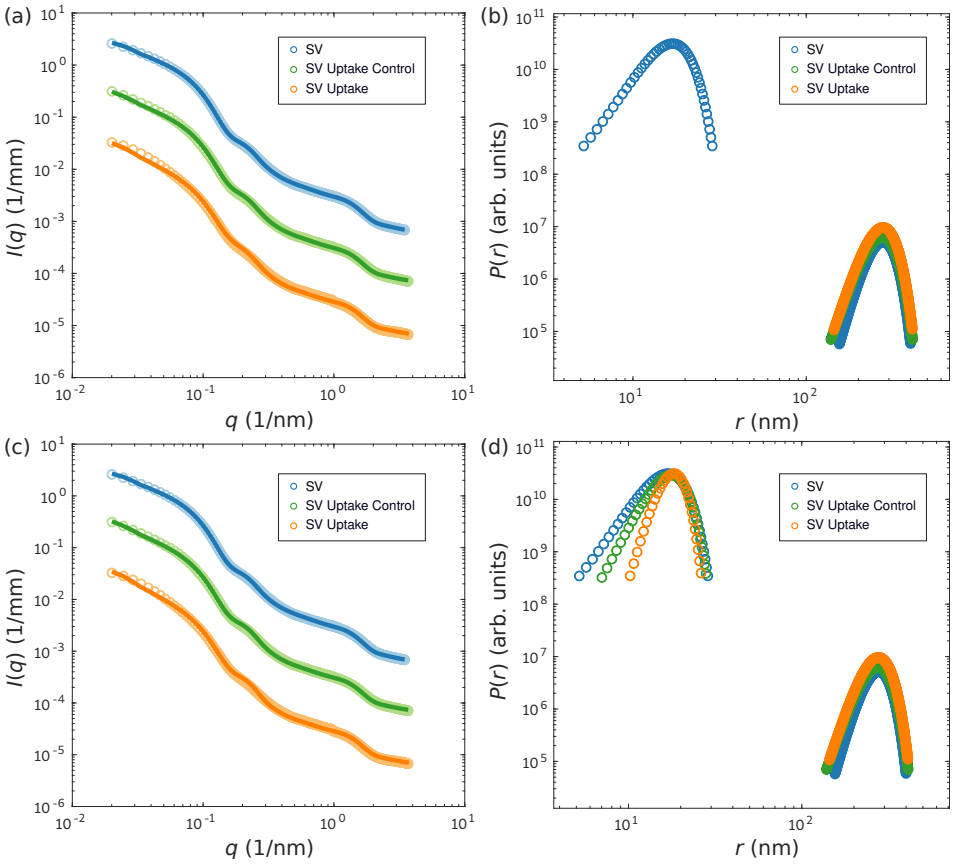

Fig. A.13: Least-squares fits to SAXS data and bimodal Gaussian size distributions obtained from least-squares fits of SVs (blue), SV uptake control (green), and SV uptake (orange). (a) SAXS data and least-squares fits. Using the parameters obtained from the fit to SV SAXS data, the model parameters were constant for SV uptake control and SV uptake, while the large size distribution, scale, and background were free to vary (SV: $\chi^2_{\text{red}} = 68.8$, SV uptake control: $\chi^2_{\text{red}} = 303.9$, SV uptake: $\chi^2_{\text{red}} = 848.7$). (b) Size distributions obtained from the fits in (a) with the corresponding colors. (c) SAXS data and least-squares fits. For parameterization, the fit results shown in (a,b) were used and kept constant, but the small size-distribution accounting for SVs was free to vary (SV: $\chi^2_{\text{red}} = 68.8$, SV uptake control: $\chi^2_{\text{red}} = 277.4$, SV uptake: $\chi^2_{\text{red}} = 773$). (d) Size distributions obtained from the fits in (c) with the corresponding colors.

Tab. A.6: Parameters corresponding to the least-squares fits shown in Fig. A.13(a), presenting a control of the fitting strategy, with variations only in the large size fraction of contaminations.

Model fit parameter	SV	SV uptake control	SV uptake	Unit
$\rho_{\text{in}}, \rho_{\text{out}}$	46.8	46.8	46.8	$e^{-}\text{nm}^{-3}$
ρ_{tail}	-28.8	-28.8	-28.8	$e^{-}\text{nm}^{-3}$
$\sigma_{\text{in}}, \sigma_{\text{out}}$	0.68	0.68	0.68	nm
σ_{tail}	0.99	0.99	0.99	nm
R_g^{in}	2.51	2.51	2.51	nm
R_g^{out}	4.38	4.38	4.38	nm
$N_c^{in}/(4\pi(R-D-R_g^{in})^2)$	0.0179	0.0179	0.0179	nm^{-2}
$N_c^{out}/(4\pi(R+R_g^{in})^2)$	0.00136	0.00136	0.00136	nm^{-2}
ρ_{c}	52.1	52.1	52.1	$e^{-}\text{nm}^{-3}$
R	16.95	16.95	16.95	nm
σ_R	3.92	3.92	3.92	nm
amplitude	248.19	248.19	248.19	arb. units
R_{large}	277.84	274.77	277.29	nm
$\sigma_{R,\text{large}}$	40.8	45.33	44.33	nm
$\text{amplitude}_{\text{large}}$	0.43	0.58	0.87	arb. unit
scale	1.0097	0.9357	0.7291	-
constant background	0.00109	0.00121	0.00117	1/mm

Tab. A.7: Parameters corresponding to the least-squares fits shown in Fig. A.13(b), presenting a control of the fitting strategy, where the SV size distribution is varied again, after keeping the large size fraction of contaminations at the values of Tab. A.6.

Model fit parameter	SV	SV uptake control	SV uptake	Unit
$\rho_{\text{in}}, \rho_{\text{out}}$	46.8	46.8	46.8	$e^-\text{nm}^{-3}$
ρ_{tail}	-28.8	-28.8	-28.8	$e^-\text{nm}^{-3}$
$\sigma_{\text{in}}, \sigma_{\text{out}}$	0.68	0.68	0.68	nm
σ_{tail}	0.99	0.99	0.99	nm
R_g^{in}	2.51	2.51	2.51	nm
R_g^{out}	4.38	4.38	4.38	nm
$N_c^{in}/(4\pi(R-D-R_g^{in})^2)$	0.0179	0.0179	0.0179	nm^{-2}
$N_c^{out}/(4\pi(R+R_g^{in})^2)$	0.00136	0.00136	0.00136	nm^{-2}
ρ_{c}	52.1	52.1	52.1	$e^-\text{nm}^{-3}$
R	16.95	17.63	18.28	nm
σ_R	3.92	3.54	2.68	nm
amplitude	248.19	208.93	170.53	arb. units
R_{large}	277.84	274.77	277.29	nm
$\sigma_{R,\text{large}}$	40.8	45.33	44.33	nm
$\text{amplitude}_{\text{large}}$	0.43	0.58	0.87	arb. unit
scale	1.0097	1.0053	0.8337	-
constant background	0.00109	0.00122	0.00117	1/mm

A.3.3 Supplementary SAXS data analysis: isotropic model composed of spherical shells

Fig. A.14 and Tab. A.8 presents an alternative model composed of spherical shells [101], see the sketch in Fig. A.14(a), and hence ignoring the patchiness of proteins on the SV surface. The EDP (Fig. A.14(b)) was parameterized as follows: the lipid bilayer is modeled by three shells, and the proteins by two layers (outer and inner). In addition, to account for possible density changes at high glutamate concentration, the vesicle lumen is allowed to have a different electron density from the buffer outside the vesicle. For $p(r)$, a single Gaussian distribution was used. In order to shed light on the effect which a density contrast (lumen to outside) has on the SAXS curve, we

first carried out a simulation, increasing the interior successively by 1 %, 5 %, 15 %, and 30 % (Fig. A.14(b,c)). Minor changes in the scattering curve can be observed for an increase of 1 %. Contrary, for a 5 % increase, distinct and significant differences can be observed at low-q-values, while the high-q data is almost unaffected. A free least-square fit to the data is shown in Fig. A.14(d), along with the corresponding EDP and size distribution (Fig. A.14(e,f)). The mean radius of $R = 17.3$ nm is in good agreement with the anisotropic model, but the overall discrepancies does not allow to deduce much further detail. This is in line with the conclusion put forward in [104, 107], that the existence of anisotropy resulting from protein patches has to be considered to achieve satisfactory fits of SV SAXS curves.

Tab. A.8: Structural parameters and fit results obtained from the isotropic six-shell model shown in Fig. A.14.

Parameters	Description	Fit results	Unit
t_c	thickness lipid chains	3 (const.)	nm
t_h	thickness lipid head groups	1 (const.)	nm
$t_{p,in}$	thickness proteins inside	5.46	nm
$t_{p,out}$	thickness proteins outside	5.05	nm
ρ_c	electron density lipid chains	275.08	$e^-\text{nm}^{-3}$
ρ_h	electron density lipid headgroups	420 (const.)	$e^-\text{nm}^{-3}$
$\rho_{p,in}$	electron density proteins inside	367.62	$e^-\text{nm}^{-3}$
$\rho_{p,out}$	electron density proteins outside	330.33	$e^-\text{nm}^{-3}$
$\rho_{s,in}$	electron density inside the vesicle	345.98	$e^-\text{nm}^{-3}$
$\rho_{s,out}$	electron density outside the vesicle	334 (const.)	$e^-\text{nm}^{-3}$
R	mean radius	17.32	nm
σ_R	standard deviation (width) of the size distribution	9.7	nm
scale		4.5e-07	-
background		0.00135	mm^{-1}

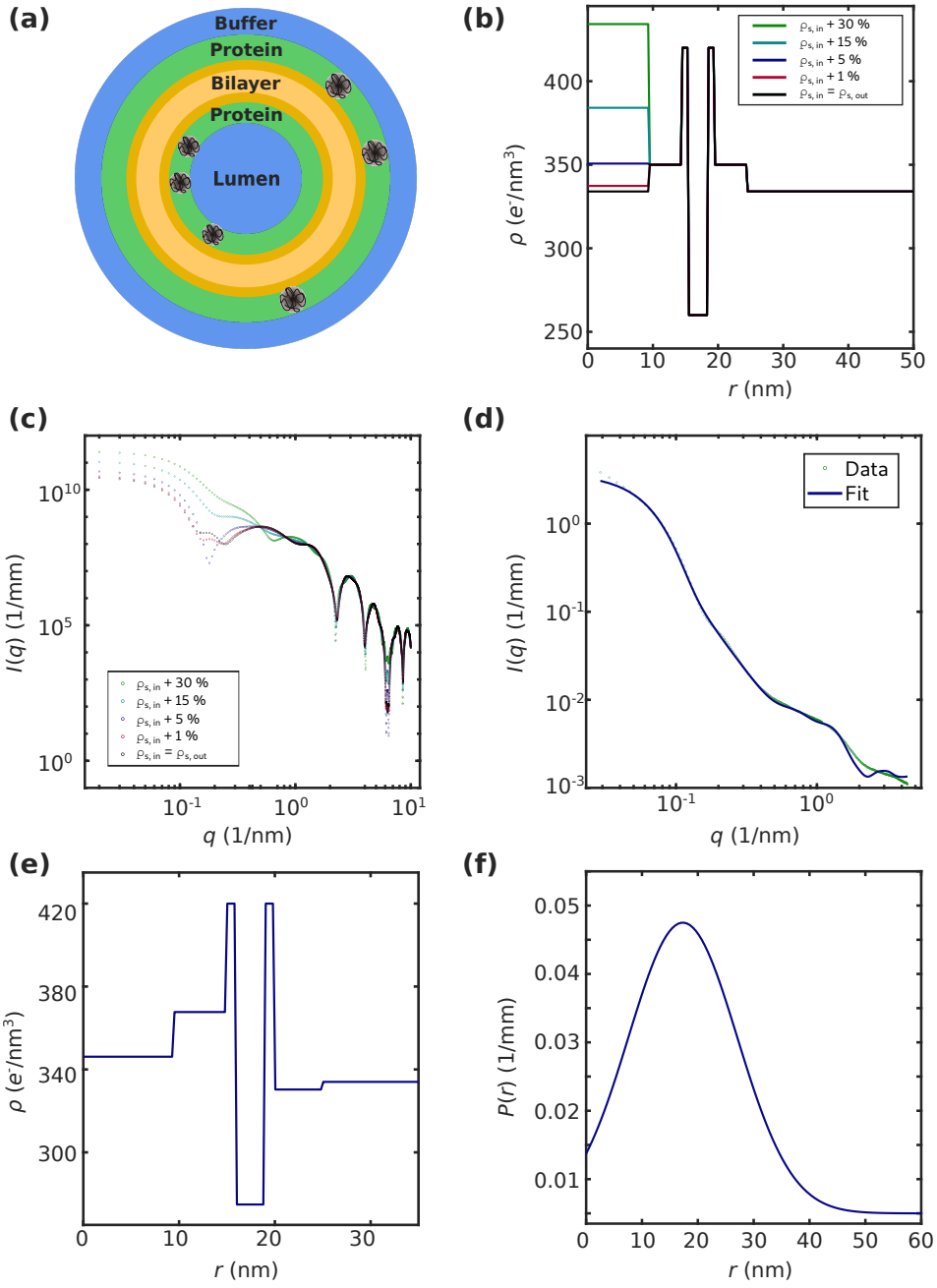

Fig. A.14: Isotropic SAXS model. (a) Sketch of the isotropic SAXS model. (b) EDPs used for the scattering simulations. (c) Simulated SAXS curves using the isotropic SAXS model. (d) Least-squares fit to SV SAXS data using the isotropic SAXS model. (e,f) EDP and size distribution obtained from least-squares fit shown in (d).

A.3.4 Supplementary data: SVs in different buffer

Fig. A.15 presents an additional set of SAXS data obtained from SVs with the uptake and the corresponding control experiments. In contrast to the SV SAXS data presented in the main article, here a different buffer with 300 mM glycine, 5 mM HEPES, 2 mM $MgS0_4 \times 7H_2O$ (pH 7.3) was used, without KCl. The difference in the buffer resulted in noticeable differences in the SAXS lineshapes (compared to Fig. 4.3 in the main article), in particular in the intermediate q-range (between 0.1 and 0.4 nm^{-1}).

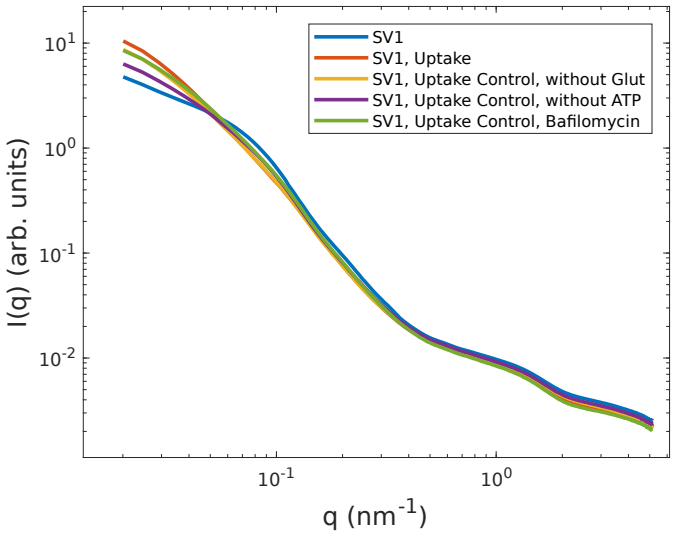

Fig. A.15: Comparison of SAXS data $I(q)$ vs. q obtained from (blue) inactive SVs and (red) active SVs upon the addition of 4 mM ATP, 10 mM k-glutamate, and 4 mM KCl. For the control experiments, (yellow) 4 mM ATP without K-glutamate, (purple) 10 mM K-glutamate without ATP, and (green) 1 mM ATP, 10 mM k-glutamate, and 4 mM KCl together with bafilomycin was added to the SV suspension. Compared to the SAXS data discussed in the main text (Fig.3), here a different buffer was used, 300 mM glycine, 5 mM HEPES, 2 mM $MgS0_4 \times 7H_2O$ (pH 7.3), where KCl was only added for the uptake and the uptake control experiments.

Bibliography

[1] T. C. Südhof. “The Synaptic Vesicle Cycle”. In: *Annual Review of Neuroscience* 27.1 (2004). PMID: 15217342, 509–547.

[2] T. C. Südhof and J. Rizo. “Synaptic vesicle exocytosis”. In: *Cold Spring Harbor perspectives in biology* 3.12 (2011), a005637.

[3] R. Jahn and D. Fasshauer. “Molecular machines governing exocytosis of synaptic vesicles”. In: *Nature* 490.7419 (2012), 201–207.

[4] S. Takamori et al. “Molecular Anatomy of a Trafficking Organelle”. In: *Cell* 127.4 (2006), 831–846.

[5] E. E. Bellocchio et al. “Uptake of Glutamate into Synaptic Vesicles by an Inorganic Phosphate Transporter”. In: *Science* 289.5481 (2000), pp. 957–960.

[6] S. Takamori. “Presynaptic Molecular Determinants of Quantal Size”. In: *Frontiers in synaptic neuroscience* 8 (2016), 2–2.

[7] M. Martineau et al. “VGLUT1 functions as a glutamate/proton exchanger with chloride channel activity in hippocampal glutamatergic synapses”. In: *Nature Communications* 8.1 (2017), p. 2279.

[8] V. Rangaraju, N. Calloway, and T. A. Ryan. “Activity-Driven Local ATP Synthesis Is Required for Synaptic Function”. In: *Cell* 156.4 (2014), 825–835.

[9] S. Takamori et al. “Identification of a vesicular glutamate transporter that defines a glutamatergic phenotype in neurons”. In: *Nature* 407.6801 (2000), 189–194.

[10] S. Takamori et al. “Identification of Differentiation-Associated Brain-Specific Phosphate Transporter as a Second Vesicular Glutamate Transporter (VGLUT2)”. In: *Journal of Neuroscience* 21.22 (2001), RC182–RC182.

[11] C. Gras et al. “A Third Vesicular Glutamate Transporter Expressed by Cholinergic and Serotoninergic Neurons”. In: *Journal of Neuroscience* 22.13 (2002), pp. 5442–5451.

[12] J. Preobraschenski et al. “Vesicular Glutamate Transporters Use Flexible Anion and Cation Binding Sites for Efficient Accumulation of Neurotransmitter”. In: *Neuron* 84.6 (2014), 1287–1301.

[13] Y. Wang et al. “Counting the Number of Glutamate Molecules in Single Synaptic Vesicles”. In: *Journal of the American Chemical Society* 141.44 (2019). doi: 10.1021/jacs.9b09414, 17507–17511.

[14] K. L. Budzinski et al. “Large Structural Change in Isolated Synaptic Vesicles upon Loading with Neurotransmitter”. In: *Biophysical Journal* 97.9 (2009), 2577–2584.

[15] T.-T. Kliesch et al. “Membrane tension increases fusion efficiency of model membranes in the presence of SNAREs”. In: *Scientific Reports* 7.1 (2017), 12070–.

[16] C. Rosenmund and C. F. Stevens. “Definition of the Readily Releasable Pool of Vesicles at Hippocampal Synapses”. In: *Neuron* 16.6 (1996), pp. 1197 –1207.

[17] R. Jahn and R. H. Scheller. “SNAREs: engines for membrane fusion”. In: *Nat. Rev. Mol. Cell Biol.* 7.9 (2006), 631–643.

[18] D Fasshauer et al. “Conserved structural features of the synaptic fusion complex: SNARE proteins reclassified as Q- and R-SNAREs”. In: *Proceedings of the National Academy of Sciences of the United States of America* 95.26 (1998), 15781–15786.

[19] W. S. Trimble, D. M. Cowan, and R. H. Scheller. “VAMP-1: a synaptic vesicle-associated integral membrane protein”. In: *Proceedings of the National Academy of Sciences* 85.12 (1988), pp. 4538–4542.

[20] M. Baumert et al. “Synaptobrevin: an integral membrane protein of 18,000 daltons present in small synaptic vesicles of rat brain.” In: *The EMBO Journal* 8.2 (1989), pp. 379–384.

[21] R. B. Sutton et al. “Crystal structure of a SNARE complex involved in synaptic exocytosis at 2.4 resolution”. In: *Nature* 395.6700 (1998), pp. 347–353.

[22] A. Stein et al. “Helical extension of the neuronal SNARE complex into the membrane”. In: *Nature* 460.7254 (2009), pp. 525–528.

[23] J. M. Hernandez et al. “Membrane Fusion Intermediates via Directional and Full Assembly of the SNARE Complex”. In: *Science* 336.6088 (2012), 1581–1584.

[24] D. Fasshauer et al. “Structural Changes are Associated with Soluble N-Ethylmaleimide-sensitive Fusion Protein Attachment Protein Receptor Complex Formation”. In: *Journal of Biological Chemistry* 272.44 (1997), pp. 28036–28041.

[25] T. Weber et al. “SNAREpins: Minimal Machinery for Membrane Fusion”. In: *Cell* 92.6 (1998), 759–772.

[26] C. G. Schuette et al. “Determinants of liposome fusion mediated by synaptic SNARE proteins”. In: *Proceedings of the National Academy of Sciences* 101.9 (2004), pp. 2858–2863.

[27] G. van Meer, D. R. Voelker, and G. W. Feigenson. “Membrane lipids: where they are and how they behave”. In: *Nature Reviews Molecular Cell Biology* 9.2 (2008), 112–124.

[28] M. R. Wenk. “Lipidomics: New Tools and Applications”. In: *Cell* 143.6 (2010), pp. 888 –895.

[29] T. Harayama and H. Riezman. “Understanding the diversity of membrane lipid composition”. In: *Nature Reviews Molecular Cell Biology* 19.5 (2018), 281–296.

[30] K. T. Lewis et al. “Unique Lipid Chemistry of Synaptic Vesicle and Synaptosome Membrane Revealed Using Mass Spectrometry”. In: *ACS Chemical Neuroscience* 8.6 (2017). PMID: 28244738, pp. 1163–1169.

[31] J. Israelachvili. *Intermolecular and Surface Forces: With Applications to Colloidal and Biological Systems*. Academic Press, 1992.

[32] E. Sackmann. *Handbook of Biological Physics, Volume 1*. Elsevier Science B.V., 1995.

[33] Y. Kozlovsky and M. M. Kozlov. “Stalk Model of Membrane Fusion: Solution of Energy Crisis”. In: *Biophysical Journal* 82.2 (2002), pp. 882 –895.

[34] S. Aeffner et al. “Energetics of stalk intermediates in membrane fusion are controlled by lipid composition”. In: *Proceedings of the National Academy of Sciences* 109.25 (2012), E1609–E1618.

[35] L. V. Chernomordik and M. M. Kozlov. “Mechanics of membrane fusion”. In: *Nature structural & molecular biology* 15.7 (2008), 675–683.

[36] S. J. Marrink, A. H. de Vries, and D. P. Tieleman. “Lipids on the move: Simulations of membrane pores, domains, stalks and curves”. In: *Biochimica et Biophysica Acta (BBA) - Biomembranes* 1788.1 (2009), pp. 149–168.

[37] H. J. Risselada and H. Grubmüler. “How SNARE molecules mediate membrane fusion: recent insights from molecular simulations”. In: *Curr. Opin. Struct. Biol.* 22.2 (2012), 187–196.

[38] M. Müller, K. Katsov, and M. Schick. “A New Mechanism of Model Membrane Fusion Determined from Monte Carlo Simulation”. In: *Biophysical Journal* 85.3 (2003), pp. 1611–1623.

[39] M. Schick. “Membrane Fusion: the Emergence of a New Paradigm”. In: *Journal of Statistical Physics* 142.6 (2011), pp. 1317–1323.

[40] M. Oelkers et al. “SNARE-mediated membrane fusion trajectories derived from force-clamp experiments”. In: *Proceedings of the National Academy of Sciences* 113.46 (2016), pp. 13051–13056.

[41] A. Witkowska and R. Jahn. “Rapid SNARE-Mediated Fusion of Liposomes and Chromaffin Granules with Giant Unilamellar Vesicles”. In: *Biophysical Journal* 113.6 (2017), pp. 1251 –1259.

[42] M. D’Agostino et al. “A tethering complex drives the terminal stage of SNARE-dependent membrane fusion”. In: *Nature* 551.7682 (2017), 634–638.

[43] Y. G. Smirnova, H. J. Risselada, and M. Müller. “Thermodynamically reversible paths of the first fusion intermediate reveal an important role for membrane anchors of fusion proteins”. In: *Proceedings of the National Academy of Sciences* 116.7 (2019), pp. 2571–2576.

[44] F. Manca et al. “SNARE machinery is optimized for ultrafast fusion”. In: *Proceedings of the National Academy of Sciences* 116.7 (2019), pp. 2435–2442.

[45] X. Li et al. “Symmetrical organization of proteins under docked synaptic vesicles”. In: *FEBS letters* 593.2 (2019), 144–153.

[46] R. Hubrich et al. “SNARE-Mediated Fusion of Single Chromaffin Granules with Pore-Spanning Membranes”. In: *Biophysical Journal* 116.2 (2019), pp. 308 –318.

[47] P. Mühlenbrock et al. “Fusion Pore Formation Observed during SNARE-Mediated Vesicle Fusion with Pore-Spanning Membranes”. In: *Biophysical Journal* 119.1 (2020), pp. 151 –161.

[48] R. Lipowsky. “The conformation of membranes”. In: *Nature* 349.6309 (1991), 475–481.

[49] R. Lipowsky and U. Seifert. “Adhesion of Vesicles and Membranes”. In: *Molecular Crystals and Liquid Crystals* 202.1 (1991), pp. 17–25.

[50] A. Ramachandran et al. “Adhesive interactions between vesicles in the strong adhesion limit”. In: *Langmuir : the ACS journal of surfaces and colloids* 27.1 (2010), pp. 59–73.

[51] G. Volpe Bossa, T. P. d. Souza, and S. May. “Adhesion of like-charged lipid vesicles induced by rod-like counterions”. In: *Soft Matter* 14 (19 2018), pp. 3935–3944.

[52] J. Israelachvili. *Intermolecular and Surface Forces: With Applications to Colloidal and Biological Systems*. Academic Press, 1992.

[53] W. Rawicz et al. “Effect of Chain Length and Unsaturation on Elasticity of Lipid Bilayers”. In: *Biophysical Journal* 79.1 (2000), pp. 328 –339.

[54] L. Ma et al. “Munc18-1-regulated stage-wise SNARE assembly underlying synaptic exocytosis”. In: *eLife* 4 (2015). Ed. by S. C. Harrison, e09580.

[55] Y. Zhang. “Energetics, kinetics, and pathway of SNARE folding and assembly revealed by optical tweezers”. In: *Protein Science* 26.7 (2017), pp. 1252–1265.

[56] U. Mennicke, D. Constantin, and T. Salditt. “Structure and interaction potentials in solid-supported lipid membranes studied by X-ray reflectivity at varied osmotic pressure”. In: *The European Physical Journal E* 20.2 (2006), 221–230.

[57] V. A. Parsegian and B. W. Ninham. “Application of the Lifshitz Theory to the Calculation of Van der Waals Forces across Thin Lipid Films”. In: *Nature* 224.5225 (1969), pp. 1197–1198.

[58] V. A. Parsegian. *Van der Waals Forces: A Handbook for Biologists, Chemists, Engineers, and Physicists*. Cambridge: Cambridge University Press, 2005, pp. –.

[59] W. Fenzl. “Van der Waals interaction of membranes”. In: 97.2 (1995), pp. 333–336–.

[60] R. Rand and V. Parsegian. “Hydration forces between phospholipid bilayers”. In: *Biochimica et Biophysica Acta (BBA) - Reviews on Biomembranes* 988.3 (1989), pp. 351 –376.

[61] J. N. Israelachvili and H. Wennerstroem. “Entropic forces between amphiphilic surfaces in liquids”. In: *J. Phys. Chem.* 96.2 (1992), pp. 520–531.

[62] E. Schneck, F. Sedlmeier, and R. R. Netz. “Hydration repulsion between biomembranes results from an interplay of dehydration and depolarization”. In: *Proceedings of the National Academy of Sciences* 109.36 (2012), pp. 14405–14409.

[63] H. Boroudjerdi et al. “Statics and dynamics of strongly charged soft matter”. In: *Physics Reports* 416.3 (2005), pp. 129 –199.

[64] G. C. Wong and L. Pollack. “Electrostatics of Strongly Charged Biological Polymers: Ion-Mediated Interactions and Self-Organization in Nucleic Acids and Proteins”. In: *Annual Review of Physical Chemistry* 61.1 (2010). PMID: 20055668, pp. 171–189.

[65] P. Carrivain et al. “Electrostatics of DNA compaction in viruses, bacteria and eukaryotes: functional insights and evolutionary perspective”. In: *Soft Matter* 8 (36 2012), pp. 9285–9301.

[66] J. E. Sader and D. Y. C. Chan. “Long-Range Electrostatic Attractions between Identically Charged Particles in Confined Geometries and the PoissonBoltzmann Theory”. In: *Langmuir* 16.2 (2000), 324–331.

[67] R. Jellander, S. Marčelja, and J. Quirk. “Attractive double-layer interactions between calcium clay particles”. In: *Journal of Colloid and Interface Science* 126.1 (1988), pp. 194 –211.

[68] H. Wennerstrom, A. Khan, and B. Lindman. “Ionic surfactants with divalent counterions”. In: *Advances in Colloid and Interface Science* 34 (1991), pp. 433 –449.

[69] P. Kékicheff et al. “Charge reversal seen in electrical double layer interaction of surfaces immersed in 2:1 calcium electrolyte”. In: *The Journal of Chemical Physics* 99.8 (1993), pp. 6098–6113.

[70] A. E. Larsen and D. G. Grier. “Like-charge attractions in metastable colloidal crystallites”. In: *Nature* 385.6613 (1997), 230–233.

[71] R. Netz. “Electrostatistics of counter-ions at and between planar charged walls: From Poisson-Boltzmann to the strong-coupling theory”. In: *The European Physical Journal E* 5.1 (2001), pp. 557–574.

[72] A. Naji et al. “Electrostatic interactions in strongly coupled soft matter”. In: *Physica A: Statistical Mechanics and its Applications* 352.1 (2005), pp. 131–170.

[73] A. Naji et al. “Perspective: Coulomb fluids—Weak coupling, strong coupling, in between and beyond”. In: *The Journal of Chemical Physics* 139.15 (2013), p. 150901.

[74] A. G. Moreira and R. R. Netz. “Binding of Similarly Charged Plates with Counterions Only”. In: *Phys. Rev. Lett.* 87 (7 2001), p. 078301.

[75] D. Andelman. “Electrostatic properties of membranes: the Poisson-Boltzmann theory”. In: *Handbook of biological physics* 1 (1995), pp. 603–642.

[76] T. Markovich, D. Andelman, and R. Podgornik. “Charged Membranes: Poisson-Boltzmann theory, DLVO paradigm and beyond”. In: *ArXiv e-prints* (2016).

[77] E. Trizac and L. Samaj. *Like-charge colloidal attraction: a simple argument*. 2012.

[78] W. C. Röntgen. “Über eine neue Art von Strahlen.” In: *Sonderabbdruck aus den Sitzungsberichten der Würzburger Physik.-medic. Gesellschaft* (1895), 137–147.

[79] G. Boehm. “Das Röntgendiagramm der Nerven”. In: *Kolloid-Zeitschrift* 62.1 (1933), 22–26.

[80] F. O. Schmitt, G. L. Clark, and J. N. Mrgudich. “X-ray diffraction studies on nerve”. In: *Science* 80.2085 (1934), pp. 567–568.

[81] F. O. Schmitt, R. S. Bear, and K. J. Palmer. “X-ray diffraction studies on the structure of the nerve myelin sheath”. In: *Journal of Cellular and Comparative Physiology* 18.1 (1941), pp. 31–42.

[82] R. S. Bear, K. J. Palmer, and F. O. Schmitt. “X-ray diffraction studies of nerve lipides”. In: *Journal of Cellular and Comparative Physiology* 17.3 (1941), pp. 355–367.

[83] E Gorter and F Grendel. “On Bimolecular Layers of Lipoids on the Chromocytes of the Blood”. In: *The Journal of experimental medicine* 41.4 (1925), 439–443.

[84] T. Salditt and S. Aeffner. “X-ray structural investigations of fusion intermediates: Lipid model systems and beyond”. In: *Seminars in Cell & Developmental Biology* 60 (2016). The Rhomboid Superfamily in Development and Disease Membrane fusion, pp. 65 –77.

[85] F. A. Heberle and G. Pabst. “Complex biomembrane mimetics on the sub-nanometer scale”. In: *Biophysical Reviews* 9.4 (2017), 353–373.

[86] T. Salditt, K. Komorowski, and K. Frank. “2. X-ray structure analysis of lipid membrane systems: solid-supported bilayers, bilayer stacks, and vesicles”. In: Berlin, Boston: De Gruyter, 2019, 43–86.

[87] E. F. Semeraro et al. “Increasing complexity in small-angle X-ray and neutron scattering experiments: from biological membrane mimics to live cells”. In: *Soft Matter* (2020), pp. –.

[88] L. Yang and H. W. Huang. “Observation of a Membrane Fusion Intermediate Structure”. In: *Science* 297.5588 (2002), pp. 1877–1879.

[89] Z. Khattari et al. “Stalk formation as a function of lipid composition studied by X-ray reflectivity”. In: *Biochimica et Biophysica Acta (BBA) - Biomembranes* 1848.1, Part A (2015), pp. 41 –50.

[90] Y. Xu et al. “Reconstitution of SNARE proteins into solid-supported lipid bilayer stacks and X-ray structure analysis”. In: *Biochimica et Biophysica Acta (BBA) - Biomembranes* 1860.2 (2018), pp. 566 –578.

[91] A. Cypionka et al. “Discrimination between docking and fusion of liposomes reconstituted with neuronal SNARE-proteins using FCS”. In: *Proc. Natl. Acad. Sci. U.S.A.* 106.44 (2009), pp. 18575–18580.

[92] C.-C. Lin, H.-F. Hsu, and P. J. Walla. “A One Donor-Two Acceptor Lipid Bilayer FRET Assay Based on Asymmetrically Labeled Liposomes”. In: *J. Phys. Chem. B* 120 (43) (2016), pp. 11085–11092.

[93] Y. Yang et al. “Dynamic light scattering analysis of SNARE-driven membrane fusion and the effects of SNARE-binding flavonoids”. In: *Biochemical and Biophysical Research Communications* 465.4 (2015), pp. 864–870.

[94] J. Diao et al. “Synaptic proteins promote calcium-triggered fast transition from point contact to full fusion”. In: *eLife* 1 (2012). Ed. by R. Aldrich, e00109–.

[95] T. A. M. Bharat et al. “SNARE and regulatory proteins induce local membrane protrusions to prime docked vesicles for fast calcium-triggered fusion”. In: *EMBO Rep.* 15.3 (2013), pp. 308–314.

[96] H. Yavuz et al. “Arrest of trans-SNARE zippering uncovers loosely and tightly docked intermediates in membrane fusion”. In: *The Journal of biological chemistry* 293.22 (2018), 8645–8655.

[97] L. Gui et al. “Visualization and sequencing of membrane remodeling leading to influenza virus fusion”. In: *Journal of Virology* (2016).

[98] G. Pabst et al. “Structural information from multilamellar liposomes at full hydration: Full q-range fitting with high quality x-ray data”. In: *Phys. Rev. E* 62.3 (2000), pp. 4000–4009.

[99] M. R. Brzustowicz and A. T. Brunger. “X-ray scattering from unilamellar lipid vesicles”. In: *J. Appl. Crystallogr.* 38.1 (2005), pp. 126–131.

[100] F. A. Heberle et al. “Model-based approaches for the determination of lipid bilayer structure from small-angle neutron and X-ray scattering data”. In: *Eur. Biophys. J.* 41.10 (2012), 875–890.

[101] P. Székely et al. “Solution X-ray Scattering Form Factors of Supramolecular Self-Assembled Structures”. In: *Langmuir* 26.16 (2010), 13110–13129.

[102] N. Kucerka et al. “Lipid bilayer structure determined by the simultaneous analysis of neutron and X-ray scattering data”. In: *Biophysical journal* 95.5 (2008), 2356–2367.

[103] M. Doktorova et al. “Molecular Structure of Sphingomyelin in Fluid Phase Bilayers Determined by the Joint Analysis of Small-Angle Neutron and X-ray Scattering Data”. In: *The Journal of Physical Chemistry B* 124.25 (2020), 5186–5200.

[104] S. Castorph et al. “Structure Parameters of Synaptic Vesicles Quantified by Small-Angle X-Ray Scattering”. In: *Biophys. J.* 98.7 (2010), 1200–1208.

[105] Z. Varga et al. “Towards traceable size determination of extracellular vesicles”. In: *Journal of extracellular vesicles* 3 (2014).

[106] E. F. Semeraro et al. “In vivo analysis of the Escherichia coli ultrastructure by small-angle scattering”. In: *IUCrJ* 4.Pt 6 (2017), 751–757.

[107] S Castorph et al. “Synaptic Vesicles Studied by SAXS: Derivation and Validation of a Model Form Factor”. In: *J. Phys: Conf. Ser.* 247.1 (2010), p. 012015.

[108] O. P. B. Wiklander et al. “Advances in therapeutic applications of extracellular vesicles”. In: *Science translational medicine* 11.492 (2019), eaav8521.

[109] P. Panine et al. “Probing fast kinetics in complex fluids by combined rapid mixing and small-angle X-ray scattering”. In: *Advances in Colloid and Interface Science* 127.1 (2006), pp. 9 –18.

[110] L. K. Bruetzel et al. “Time-Resolved Small-Angle X-ray Scattering Reveals Millisecond Transitions of a DNA Origami Switch”. In: *Nano Letters* 18.4 (2018), 2672–2676.

[111] S. Köster and T. Pfohl. “X-ray studies of biological matter in microfluidic environments”. In: *Mod. Phys. Lett. B* 26.26 (2012), pp. 1230018–.

[112] B. F. B. Silva. “SAXS on a chip: from dynamics of phase transitions to alignment phenomena at interfaces studied with microfluidic devices”. In: *Phys. Chem. Chem. Phys.* 19 (35 2017), pp. 23690–23703.

[113] S. A. Watkin et al. “Microfluidics for Small-Angle X-ray Scattering”. In: *X-ray Scattering*. Ed. by A. E. Ares. Rijeka: IntechOpen, 2017. Chap. 4.

[114] T. M. Squires and S. R. Quake. “Microfluidics: Fluid physics at the nanoliter scale”. In: *Rev. Mod. Phys.* 77 (3 2005), pp. 977–1026.

[115] E. M. Purcell. “Life at low Reynolds number”. In: *American Journal of Physics* 45.1 (1977), pp. 3–11.

[116] L. Pollack et al. “Time Resolved Collapse of a Folding Protein Observed with Small Angle X-Ray Scattering”. In: *Phys. Rev. Lett.* 86 (21 2001), pp. 4962–4965.

[117] M. Buscema et al. “Spatially resolved small-angle X-ray scattering for characterizing mechanoresponsive liposomes using microfluidics”. In: *Materials Today Bio* 1 (2019), p. 100003.

[118] T. Salditt and M. Osterhoff. “X-ray Focusing and Optics”. In: *Nanoscale Photonic Imaging*. Ed. by T. Salditt, A. Egner, and D. R. Luke. Cham: Springer International Publishing, 2020, pp. 71–124.

[119] A. Grafmüller, J. Shillcock, and R. Lipowsky. “The Fusion of Membranes and Vesicles: Pathway and Energy Barriers from Dissipative Particle Dynamics”. In: *Biophysical Journal* 96.7 (2008), 2658–2675.

[120] B. Weinhausen et al. “Acyl-Chain Correlation in Membrane Fusion Intermediates: X-Ray Diffraction from the Rhombohedral Lipid Phase”. In: *Biophysical Journal* 102.9 (2012), 2121–2129.

[121] F. A. Heberle et al. “Model-based approaches for the determination of lipid bilayer structure from small-angle neutron and X-ray scattering data”. In: *Eur. Biophys. J.* 41.10 (2012), pp. 875–890.

[122] Z. K. Issa et al. “Ca2+ Bridging of Apposed Phospholipid Bilayers”. In: *J. Phys. Chem. B* 114.41 (2010), pp. 13249–13254.

[123] H.-H. G. Tsai et al. “Molecular dynamics simulation of cation-phospholipid clustering in phospholipid bilayers: Possible role in stalk formation during membrane fusion”. In: *Biochimica et Biophysica Acta (BBA) - Biomembranes* 1818.11 (2012), pp. 2742–2755.

[124] M. Pannuzzo et al. “Simulation of polyethylene glycol and calcium-mediated membrane fusion”. In: *J. Chem. Phys.* 140.12 (2014), pp. 124905–.

[125] S. Castorph et al. “Synaptic vesicles studied by dynamic light scattering”. In: *The European Physical Journal E* 34.6 (2011), p. 63.

[126] A. V. Pobbati, A. Stein, and D. Fasshauer. “N- to C-Terminal SNARE Complex Assembly Promotes Rapid Membrane Fusion”. In: *Science* 313.5787 (2006), pp. 673–676.

[127] D. Fasshauer et al. “Mixed and Non-cognate SNARE Complexes: Characterization of Assembly and Biophysical Properties”. In: *Journal of Biological Chemistry* 274.22 (1999), pp. 15440–15446.

[128] P. Pernot et al. “Upgraded ESRF BM29 beamline for SAXS on macromolecules in solution”. In: *Journal of Synchrotron Radiation* 20.4 (2013), pp. 660–664.

[129] M. E. Brennich et al. “Online data analysis at the ESRF bioSAXS beamline, BM29”. In: *Journal of Applied Crystallography* 49.1 (2016), pp. 203–212.

[130] P. Heftberger et al. “Global small-angle X-ray scattering data analysis for multilamellar vesicles: the evolution of the scattering density profile model”. English. In: *Journal of applied crystallography* 47.1 (2014), pp. 173–178.

[131] H. I. Petrache et al. “Interbilayer interactions from high-resolution x-ray scattering”. In: *Phys. Rev. E* 57 (6 1998), pp. 7014–7024.

[132] S Tristram-Nagle, H. I. Petrache, and J. F. Nagle. “Structure and interactions of fully hydrated dioleoylphosphatidylcholine bilayers”. In: *Biophysical journal* 75.2 (1998), 917–925.

[133] B. Demé et al. “Giant Collective Fluctuations of Charged Membranes at the Lamellar-to-Vesicle Unbinding Transition. 1. Characterization of a New Lipid Morphology by SANS, SAXS, and Electron Microscopy”. In: *Langmuir* 18.4 (2002), 997–1004.

[134] M. Hishida et al. “Electrostatic double-layer interaction between stacked charged bilayers”. In: *Phys. Rev. E* 96 (4 2017), p. 040601.

[135] A. Moreira and R. Netz. “Simulations of counterions at charged plates”. In: *The European Physical Journal E* 8.1 (2002), pp. 33–58.

[136] N. Kucerka et al. “Influence of cholesterol on the bilayer properties of monounsaturated phosphatidylcholine unilamellar vesicles”. In: *The European Physical Journal E* 23.3 (2007), pp. 247–254.

[137] B. Angelov, M. Ollivon, and A. Angelova. “X-ray Diffraction Study of the Effect of the Detergent Octyl Glucoside on the Structure of Lamellar and Nonlamellar Lipid/Water Phases of Use for Membrane Protein Reconstitution”. In: *Langmuir* 15.23 (1999), pp. 8225–8234.

[138] N. Kucerka et al. “Curvature Effect on the Structure of Phospholipid Bilayers”. In: *Langmuir* 23.3 (2007), pp. 1292–1299.

[139] N. Kucerka, M.-P. Nieh, and J. Katsaras. “Asymmetric Distribution of Cholesterol in Unilamellar Vesicles of Monounsaturated Phospholipids”. In: *Langmuir* 25.23 (2009), pp. 13522–13527.

[140] O. Szekely et al. “The Structure of Ions and Zwitterionic Lipids Regulates the Charge of Dipolar Membranes”. In: *Langmuir* 27.12 (2011), pp. 7419–7438.

[141] R. J. Alsop, R. Maria Schober, and M. C. Rheinstadter. “Swelling of phospholipid membranes by divalent metal ions depends on the location of the ions in the bilayers”. In: *Soft Matter* 12.32 (2016), pp. 6737–6748.

[142] O. Lotan et al. “Critical Conditions for Adsorption of Calcium Ions onto Dipolar Lipid Membranes”. In: *J. Phys. Chem. A* 120.19 (2016), pp. 3390–3396.

[143] U. Seifert, K. Berndl, and R. Lipowsky. “Shape transformations of vesicles: Phase diagram for spontaneous- curvature and bilayer-coupling models”. In: *Phys. Rev. A* 44 (2 1991), pp. 1182–1202.

[144] R. R. Netz and R. Lipowsky. “Unbinding of symmetric and asymmetric stacks of membranes”. In: *Phys. Rev. Lett.* 71 (21 1993), pp. 3596–3599.

[145] K. Komorowski et al. “Vesicle Adhesion and Fusion Studied by Small-Angle X-Ray Scattering”. In: *Biophysical Journal* 114.8 (2018), 1908–1920.

[146] L. Fink et al. “Structure and Interactions between Charged Lipid Membranes in the Presence of Multivalent Ions”. In: *Langmuir* 35.30 (2019), pp. 9694–9703.

[147] T. Mukhina et al. “Attractive Interaction between Fully Charged Lipid Bilayers in a Strongly Confined Geometry”. In: *J. Phys. Chem. Lett.* 10.22 (2019), pp. 7195–7199.

[148] G. Pabst et al. “X-ray Kinematography of Temperature-Jump Relaxation Probes the Elastic Properties of Fluid Bilayers”. In: *Langmuir* 16.23 (2000), pp. 8994–9001.

[149] Z. Varga, A. Wacha, and A. Bóta. "Osmotic shrinkage of sterically stabilized liposomes as revealed by time-resolved small-angle X-ray scattering". In: *Journal of Applied Crystallography* 47.1 (2014), pp. 35–40.

[150] A. Yaghmur, B. Sartori, and M. Rappolt. "The role of calcium in membrane condensation and spontaneous curvature variations in model lipidic systems". In: *Phys. Chem. Chem. Phys.* 13.8 (2011), pp. 3115–3125.

[151] A. Yaghmur et al. "Calcium triggered L alpha-H2 phase transition monitored by combined rapid mixing and time-resolved synchrotron SAXS". In: *PloS one* 3.4 (2008), e2072–e2072.

[152] A. Ghazal et al. "Direct monitoring of calcium-triggered phase transitions in cubosomes using small-angle X-ray scattering combined with microfluidics". In: *Journal of Applied Crystallography* 49.6 (2016), pp. 2005–2014.

[153] A. Ghazal et al. "Microfluidic Platform for the Continuous Production and Characterization of Multilamellar Vesicles: A Synchrotron Small-Angle X-ray Scattering (SAXS) Study". In: *The Journal of Physical Chemistry Letters* 8.1 (2017). PMID: 27936765, pp. 73–79.

[154] A. S. Poulos et al. "Microfluidic SAXS Study of Lamellar and Multilamellar Vesicle Phases of Linear Sodium Alkylbenzenesulfonate Surfactant with Intrinsic Isomeric Distribution". In: *Langmuir* 32.23 (2016), pp. 5852–5861.

[155] M. Denz et al. "Cyclic olefin copolymer as an X-ray compatible material for microfluidic devices". In: *Lab Chip* 18.1 (2018), pp. 171–178.

[156] E. Samson, J. Marchand, and K. A. Snyder. "Calculation of Ionic Diffusion Coefficients on the Basis of Migration Test Results". en. In: *Materials and Structures* 36.3 (2003), pp. 156–165.

[157] T. Narayanan et al. "A multipurpose instrument for time-resolved ultra-small-angle and coherent X-ray scattering". In: *Journal of Applied Crystallography* 51.6 (2018), 1511–1524.

[158] T. Salditt et al. "Compound focusing mirror and X-ray waveguide optics for coherent imaging and nano-diffraction". In: *Journal of Synchrotron Radiation* 22.4 (2015), pp. 867–878.

[159] T. Narayanan, J. Gummel, and M. Gradzielski. "Chapter Seven - Probing the Self-Assembly of Unilamellar Vesicles Using Time-Resolved SAXS". In: *Advances in Planar Lipid Bilayers and Liposomes*. Ed. by A. Iglič and C. V. Kulkarni. Vol. 20. Academic Press, 2014, 171–196.

[160] B. Angelov et al. “Rapid mixing stopped-flow small-angle X-ray scattering study of lipoplex formation at beamline ID02@ESRF”. In: *Journal of Surface Investigation. X-ray, Synchrotron and Neutron Techniques* 9.1 (2015), pp. 105–110.

[161] A. Schlaich, A. P. dos Santos, and R. R. Netz. “Simulations of Nanoseparated Charged Surfaces Reveal Charge-Induced Water Reorientation and Nonadditivity of Hydration and Mean-Field Electrostatic Repulsion”. In: *Langmuir* 35.2 (2019), pp. 551–560.

[162] R. B. Sutton et al. “Crystal structure of a SNARE complex involved in synaptic exocytosis at 2.4 rA resolution”. In: *Nature* 395.6700 (1998), 347–353.

[163] K. I. Willig et al. “STED microscopy reveals that synaptotagmin remains clustered after synaptic vesicle exocytosis”. In: *Nature* 440.7086 (2006), 935–939.

[164] D. L. Rupert et al. “Methods for the physical characterization and quantification of extracellular vesicles in biological samples”. In: *Biochimica et Biophysica Acta (BBA) - General Subjects* 1861.1, Part A (2017), pp. 3164–3179.

[165] Z. Varga et al. “Size Measurement of Extracellular Vesicles and Synthetic Liposomes: The Impact of the Hydration Shell and the Protein Corona”. In: *Colloids and Surfaces B: Biointerfaces* 192 (2020), p. 111053.

[166] F. Perissinotto et al. “Chapter Six - Multi-technique analysis of extracellular vesicles: not only size matters”. In: *Advances in Biomembranes and Lipid Self-Assembly*. Ed. by A. Bongiovanni et al. Vol. 32. Advances in Biomembranes and Lipid Self-Assembly. Academic Press, 2020, pp. 157–177.

[167] G. Ahnert-Hilger et al. “Regulation of vesicular neurotreansmitter transporters”. In: *Reviews of Physiology, Biochemistry and Pharmacology*. Berlin, Heidelberg: Springer Berlin Heidelberg, 2004, 140–160.

[168] R. H. Edwards. “The Neurotransmitter Cycle and Quantal Size”. In: *Neuron* 55.6 (2007), 835–858.

[169] J. Preobraschenski et al. “Dual and Direction-Selective Mechanisms of Phosphate Transport by the Vesicular Glutamate Transporter”. In: *Cell Reports* 23.2 (2018), 535–545.

[170] P. Székely et al. “Solution X-ray scattering form factors of supramolecular self-assembled structures”. In: *Langmuir* 26.16 (2010), pp. 13110–13129.

[171] A. J. B. Kreutzberger et al. “In vitro fusion of single synaptic and dense core vesicles reproduces key physiological properties”. In: *Nature Communications* 10.1 (2019), 3904–.

[172] Y. Sembira-Nahum, A. Apelblat, and E. Manzurola. “Volumetric Properties of Aqueous Solutions of L-Glutamic Acid and Magnesium-L-Glutamate”. In: *Journal of Solution Chemistry* 37.3 (2008), pp. 391–401.

[173] M. M. Seibert et al. “Single mimivirus particles intercepted and imaged with an X-ray laser”. In: *Nature* 470.7332 (2011), 78–81.

[174] E. Sobolev et al. “Megahertz single-particle imaging at the European XFEL”. In: *Communications Physics* 3.1 (2020), p. 97.

[175] H. N. Chapman. “X-Ray Free-Electron Lasers for the Structure and Dynamics of Macromolecules”. In: *Annual Review of Biochemistry* 88.1 (2019). PMID: 30601681, pp. 35–58.

[176] G. Brändén et al. “Coherent diffractive imaging of microtubules using an X-ray laser”. In: *Nature Communications* 10.1 (2019), p. 2589.

[177] D. Oberthür. “Biological single-particle imaging using XFELs - towards the next resolution revolution”. eng. In: *IUCrJ* 5.Pt 6 (2018). 30443350[pmid], pp. 663–666.

[178] J. Bielecki et al. “Electrospray sample injection for single-particle imaging with x-ray lasers”. In: *Science Advances* 5.5 (2019), eaav8801.

[179] M. F. Hantke, T. Ekeberg, and F. R. Maia. “Condor: a simulation tool for flash X-ray imaging”. In: *Journal of applied crystallography* 49.4 (2016), 1356–1362.

[180] F. R. N. C. Maia et al. “*Hawk*: the image reconstruction package for coherent X-ray diffractive imaging”. In: *Journal of Applied Crystallography* 43.6 (2010), 1535–1539.

[181] M. Maidorn et al. “Nanobodies reveal an extra-synaptic population of SNAP-25 and Syntaxin 1A in hippocampal neurons”. In: *mAbs* 11.2 (2019), 305–321.

[182] S. Schenck et al. “Generation and Characterization of Anti-VGLUT Nanobodies Acting as Inhibitors of Transport”. In: *Biochemistry* 56.30 (2017), 3962–3971.

[183] J. Bielecki et al. “Electrospray sample injection for single-particle imaging with x-ray lasers”. In: *Science Advances* 5.5 (2019).

[184] M. F. Hantke et al. “Rayleigh-scattering microscopy for tracking and sizing nanoparticles in focused aerosol beams”. In: *IUCrJ* 5.6 (2018), pp. 673–680.

[185] M. F. Hantke et al. “High-throughput imaging of heterogeneous cell organelles with an X-ray laser”. In: *Nature Photonics* 8.12 (2014), 943–949.

[186] T. Ekeberg et al. “Three-Dimensional Reconstruction of the Giant Mimivirus Particle with an X-Ray Free-Electron Laser”. In: *Phys. Rev. Lett.* 114 (9 2015), p. 098102.

[187] B. J. Daurer et al. “Experimental strategies for imaging bioparticles with femtosecond hard X-ray pulses. Corrigendum”. In: *IUCrJ* 6.3 (2019), p. 500.

[188] J. Als-Nielsen. *Elements of Modern X-Ray Physics*. Wiley, 2001.

[189] S. W. Provencher and P. Štêpánek. “Global Analysis of Dynamic Light Scattering Autocorrelation Functions”. In: *Particle & Particle Systems Characterization* 13.5 (1996), pp. 291–294.

Authors Contribution

In the following detailed information about the particular contributions of the author in the publications is given. Two peer-reviewed articles and one unpublished manuscript are considered for this cumulative thesis to fulfill the rules and regulations of the PhD program Göttingen Graduate Center for Neurosciences (GGNB) that is part of the Georg-August-University School of Science (GAUSS):

(1) K. Komorowski, A. Salditt, Y. Xu, H. Yavuz, M. Brennich, R. Jahn, and T. Salditt. Vesicle adhesion and fusion studied by small-angle X-ray scattering. *Biophysical Journal,* 114(8), 1908 – 1920 (2018).

(2) K. Komorowski, J. Schaeper, M. Sztucki, L. Sharpnack, G. Brehm, S. Köster, and T. Salditt. Vesicle adhesion in the electrostatic strong-coupling regime studied by time-resolved small-angle X-ray scattering. *Soft Matter,* 16, 4142 – 4154 (2020).

(3) K. Komorowski, J. Preobraschenski, M. Ganzella, J. Alfken, C. Neuhaus, R. Jahn, and T. Salditt. Neurotransmitter uptake by synaptic vesicles studied by X-ray diffraction. *Unpublished,* (2020).

In (1) vesicle adhesion and fusion were studied by SAXS and predictions of interaction potential models were evaluated and compared to experimental results. KK, RJ and TS designed research. KK, AS, and HY prepared samples. KK, AS, YX, and TS carried out synchrotron experiments with support and advice from MB. KK analyzed data with support from AS and YX and advice from TS. KK and AS carried out dynamic light scattering experiments. KK and TS wrote the manuscript, with comments and critical reading from all authors.

In (2) time-resolved SAXS was used to study structural dynamics of vesicle adhesion and fusion with a main focus on strong-coupling like-charge attraction. KK and TS designed research. KK, JS, and GB fabricated the microfluidics devices with advice from SK. KK and JS prepared samples. KK, JS, and TS carried out synchrotron experiments with support and advice from MS and LS. KK analyzed data with advice from TS. KK and TS wrote the manuscript, with comments and critical reading from all authors.

Neurotransmitter uptake and fusion of SVs were studied by SAXS and single-SV CDI simulations were performed in (3). KK, JP, RJ and TS designed research. MG performed

SV purification. KK prepared samples with advice from JP and MG. KK and TS carried out synchrotron experiments. KK analyzed data with support from JA and advice from TS. CN and JA carried out dynamic light scattering experiments with advice from KK and TS. KK performed coherent diffractive imaging simulations of SVs with advice from TS. KK and TS wrote the manuscript.

Publications

(1) K. Komorowski, A. Salditt, Y. Xu, H. Yavuz, M. Brennich, R. Jahn, and T. Salditt. Vesicle adhesion and fusion studied by small-angle X-ray scattering. *Biophysical Journal,* 114(8), 1908 – 1920 (2018).

(2) K. Komorowski, J. Schaeper, M. Sztucki, L. Sharpnack, G. Brehm, S. Köster, and T. Salditt. Vesicle adhesion in the electrostatic strong-coupling regime studied by time-resolved small-angle X-ray scattering. *Soft Matter,* 16, 4142 – 4154 (2020).

(3) Y. Xu, J. Kuhlmann, M. Brennich, K. Komorowski, R. Jahn, C. Steinem, and T. Salditt. Reconstitution of SNARE proteins into solid-supported lipid bilayer stacks and X-ray structure analysis. *Biochimica et Biophysica Acta (BBA) - Biomembranes,* 1860(2), 566 – 578 (2018).

(4) M. Scheu, K. Komorowski, C. Shen, and T. Salditt. A stalk fluid forming above the transition from the lamellar to the rhombohedral phase of lipid membranes. *Submitted,* (2020).

(5) T. Salditt, K. Komorowski, K. Frank. 2. X-ray structure analysis of lipid membrane systems: solid-supported bilayers, bilayer stacks, and vesicles. Berlin, Boston: De Gruyter, (2019).

Acknowledgements

This work would not have been possible without the great support and input of many colleagues and collaborators.

First of all, I thank Prof. Dr. Tim Salditt for his enthusiasm for this topic and his inspiring support given to me during the time of my thesis. I am grateful for the many opportunities given to me such as participating at conferences or at exciting synchrotron experiments. For sure, I have learned a lot from you, also beyond scientific matters.

I also thank Prof. Dr. Claudia Steinem and Prof. Dr. Silvio Rizzoli for co-supervising my thesis, and for fruitful discussions on several occasions.

I thank Dr. Theyencheri Narayanan, Dr. Michael Sztucki, Dr. Lewis Sharpnack (beamline ID02), and Dr. Martha Brennich (beamline BM29) for great support during the synchrotron experiments, as well as for excellent working conditions at the European Synchrotron Radiation Facility in Grenoble. I also thank Dr. Diego Pontoni, and Pierre Lloria for sharing their resources at the Partnership for Soft Condensed Matter during our beamtimes at the ESRF.

I thank Dr. Michael Sprung for great support during the synchrotron experiments, as well as for excellent working conditions at the P10 beamline at Deutsches Elektronen-Synchrotron in Hamburg.

Further, the synchrotron experiments were only possible due to a great team effort. My special thanks go to Susanne Hengst who dedicated a lot of her time for the support in sample preparation, in particular before synchrotron experiments. I thank Annalena Salditt for excellent support during the synchrotron experiment at beamline BM29, as well as for her support in data analysis. I also thank Max Scheu for excellent support in sample preparation and data acquisition during the synchrotron experiment at the beamline ID02. I thank Jannis Schaeper for excellent support during the microfluidics SAXS experiments at beamline ID02 and P10.

I thank Prof. Dr. Reinhard Jahn for constant collaboration throughout the years, already during the time of my master thesis and continuing for this work. As part of

this collaboration, I also thank Dr. Julia Preobraschenski and Dr. Marcelo Ganzella for SV purification and fruitful discussions regarding biological matters. This work has benefited a lot of such an interdisciplinary environment.

I thank the entire group of the IRP! Within the institute, I thank in particular Kilian Frank for great scientific exchange on an everyday basis, who further dedicated a lot of his time for the support in synchrotron experiments and data analysis. I'll also keep our bouldering sessions and our trip to Fontainebleau in good memory! I also thank Malte Vaßholz for being a great office mate and for his occasional support in computational matters. Further I thank Jette Alfken for her support in the SV project, it was a pleasure to work with her.

I also thank Gerrit Brehm and Prof. Dr. Sarah Köster for close collaboration in the microfluidics project, in particular for the support in the fabrication of microfluidics devices.

I thank the Sonderforschungsbereich 803 *Funktionalität kontrolliert durch Organisation in und zwischen Membranen* and the Sonderforschungsbereich 1286 *Quantitative Synaptologie* for financial support, funded by Deutsche Forschungsgesellschaft (DFG).

Finally, my warm thanks go to my family, and in particular to Valentina Marie Skeries for her unprecedented support.